One dimensional photonic crystal for label-free and fluorescence sensing application

Original
One dimensional photonic crystal for label-free and fluorescence sensing application / Rizzo, Riccardo. - (2017).

Availability:
This version is available at: 11583/2672761 since: 2017-05-25T14:01:08Z

Publisher:
Politecnico di Torino

Published
DOI:10.6092/polito/porto/2672761

ScuDo
Scuola di Dottorato - Doctoral School
WHAT YOU ARE, TAKES YOU FAR

Doctoral Dissertation
Doctoral Program in Physics (29^{th}cycle)

One dimensional photonic crystal for label-free and fluorescence sensing application

By

Riccardo Rizzo

******

Supervisor(s):
Prof. Emiliano Descrovi, Supervisor
Prof. Fabrizio Giorgis, Co-Supervisor

Doctoral Examination Committee:
Prof. Giancarlo Cicero, Politecnico di Torino
Prof. Hans P. Herzig, EPFL Neuchatel
Prof. Rita C. Iotti, Politecnico di Torino
Prof. Giovanni Mattei, Università di Padova
Dr. Matthieu Roussey, University of Eastern Finland

Politecnico di Torino
2017

El que baila camina sobre el agua dentro de una llama
G. L.

Acknowledgements

Firstly, I would like to express my sincere gratitude to my supervisor Prof. Emiliano Descrovi for the continuous support of my Ph.D study and related research, for his motivation and the knowledge he shared with me. His guidance helped me in all the time of research.
Besides my supervisor, I would like to thank my co-supervisor Prof. Fabrizio Giorgis for his precious comments and suggestions. He was always there for every need.

I thank my fellow teammates, Dr. Angelo Angelini, Dr. Francesca Frascella, Dr. Serena Ricciardi, Susanna Licheri, Federica Pirani, Chiara Summa for the stimulating discussions, for the coffee-breaks and for all the fun we have had in the last years. It was a pleasure to work with you.

I would like to express my thanks to all the Biloba project team, especially to Dr. Maria Alvaro, Dr. Norbert Danz and Dr. Paola Rivolo, it is an honor for me to present here the results I obtained in the framework of this project.
My gratitude goes also to Dr. Luca Boarino who gave access to the INRIM nanofacilities.

Last but not the least, I would like to thank my family: my parents, Ester and Giuseppe, and my sister, Giò, for always supporting me regardless of the distance that separates us.

Abstract

The development of more sensitive and more reliable sensors aids medical applications in many fields as diseases detection or therapy progress. This thesis threats the development of an optical biosensor based on electromagnetic modes propagating at the interface between a finite one-dimensional photonic crystal (1DPC) and a homogeneous external medium, also named Bloch Surface Waves (BSW). BSW have emerged as an attractive approach for label-free sensing in plasmon-like sensor configurations. Besides label-free operation, the large field enhancement and the absence of quenching allow the use of BSW to excite fluorescent labels that are in proximity of the 1DPC surface. This approach was adapted to the case of angularly resolved resonance detection, thus giving rise to a combined label-free/labelled biosensor platform. BSW present many degrees of design freedom that enable tuning of resonance properties. In order to obtain a figure of merit for an optimization, I investigated the measurement uncertainty depending on resonance width and depth with different numerical models. This has led to a limit of detection that can assist the choice of the best design to use. Two tumor biomarkers, such as vascular endothelial growth factor (VEGF) and Angiopoietin-2 (Ang2), have been considered to be detected with the BSW biosensing platform. For this purpose the specific antibodies for the two tumor biomarkers were immobilized on the 1DPC biochip surface. The conclusive experiments reported in this work demonstrated the successful detection of the VEGF biomarker in complex matrices, such as cell culture supernatants and human plasma samples. Moreover, the platform was used to determinate Ang2 concentration in untreated human plasma samples using low volumes, 300 µL, and with short turnaround times, 30 minutes. This is the first BSW based biosensor assay for the determination of tumor biomarker in human plasma samples at clinically relevant concentrations.

Abstract

Lo sviluppo di sensori sempre più affidabili e sensibili può favorire la ricerca medica in campi come la diagnosi di malattie o il monitoraggio dell'efficacia delle terapie. Questa tesi riporta lo sviluppo di un biosensore ottico basato su modi elettromagnetici di superficie che si propagano all'interfaccia tra un cristallo fotonico unidimensionale (1DPC) ed un mezzo esterno omogeneo, conosciuti con il nome di onde di superficie di Bloch (BSW). Molta attenzione è stata data alle BSW da quando sono state utilizzate per il rilevamento diretto (label-free) di biomolecole con configurazioni simili a quelle dei sensori plasmonici. Oltre alle configurazioni label-free, la grande amplificazione del campo elettrico sulla superficie del 1DPC e l'assenza di quenching permettono di usare le BSW per eccitare molecole fluorescenti che si trovino in prossimità dell'interfaccia. In questo lavoro i due approcci, label-free e fluorescente, sono stati combinati su un'unica piattaforma che permette il rilevamento con entrambi i modi di detection. Il design di un biosensore basato su BSW presenta molti gradi di libertà. Al fine di ottenere una figura di merito per un'ottimizzazione, ho indagato alcuni parametri chiave delle BSW con diversi modelli numerici. Questo ha portato alla definizione di un limite di rilevamento teorico (LoD) che ha determinato la scelta del miglior design da utilizzare. Due biomarcatori tumorali quali il fattore di crescita vascolare endoteliale (VEGF) e l'Angiopoietina-2 (Ang2) sono stati scelti per essere rilevati con la piattaforma. A questo scopo gli anticorpi specifici per i due marcatori tumorali sono stati immobilizzati sulla superficie del 1DPC. Gli esperimenti conclusivi riportati in questo lavoro hanno dimostrato con successo la rilevazione del biomarker VEGF in matrici complesse. Inoltre, la piattaforma è stata impiegata per rilevare concentrazioni di Ang2 in plasma umano usando volumi ridotti, 300 µL, e con tempi di risposta brevi, 30 minuti. Quello riportato è il primo saggio per la quantificazione di concentrazioni clinicamente rilevanti di biomarker tumorali in plasma umano che utilizzi un biosensore basato su BSW.

Table of contents

List of figures

List of tables

Introduction

In the short stories *Storie Naturali*, Primo Levi tells of one of the many technological wonders put on the market by a mysterious American company: *il Mimete*, The Mimer, this is the name of the machine that duplicates documents, but not as a common copier. It does its job recreating on another paper the characters and symbols printed on the first: the Mimer recreates in all respects the document, the fibers and the imperfections of the paper, the lacerations, the "spots in a duplication process in which in the exact position of each atom of the model is fixed a similar atom extracted from its ink: carbon where it was carbon, nitrogen where it was nitrogen, and so on...It was really a revolutionary technique: organic synthesis at low temperature, the order from disorder, quickly and cheaply: the dream of four generations of chemists" [Levi (1987)]. The operation of the Mimer closely resembles the dream of the first supporters of nanotechnology: the chance to grow in a controlled manner and with great efficiency nanoscale structures and machines, assembling atom by atom molecular sized objects with well-defined functions.

In the same year in which the Levi's novels were sold in bookshops, the mouvie *Fatastic Voyage* made its appearance in the cinemas. The movie proposed to the audience a bold vision of nanotechnology applied to medicine: a team of doctors were miniaturized in order to remove from the inside a dangerous blood clot in the brain of a patient.

Probably, the situations described above belongs only to the realm of science fiction. Still, nanotechnology is enhancing biomedical research tools, for example, by providing new kinds of labels for experiments done to discover drugs or to reveal which sets of genes are active in cells under various conditions. Researchers are also exploiting nanoparticles as improved contrast agents for noninvasive imaging and as drug-delivery vehicles. Nanotechnology devices, moreover, can play an important part in diagnostic screens in order to detect in a fast and reliable way if any disease or cancer is developing in the patient.

This is precisely the *leitmotiv* of my doctoral thesis, contribute to the realization of a new biosensor that uses what nanotechnology has to offer for cancer prevention. The World Health Organization states that the number of new cases of cancer is expected to rise from 14 million in 2012 to 22 within the next 2 decades [Stewart and Wild (2014)]. Cancer is among the leading causes of morbidity and mortality worldwide, with approximately 8.2 million cancer related deaths in 2012 [Ferlay et al. (2015)]. Metastases are the major cause of death from cancer [Mehlen and Puisieux (2006)]. For many types of cancer, early and accurate detection allows treatment before the metastatic process begins. Therefore, early diagnosis plays a vital role for a successful therapy of the disease. Quantitative detection of cancer biomarkers is a powerful tool to diagnose cancers in early stages [Pepe et al. (2001)]. Furthermore, cancer biomarkers are used as noninvasive tool to monitor the response to the treatment. Although enzyme-linked immunosorbent assay (ELISA) is considered the preferred technique for measuring biomarkers' concentration in plasma, conventional ELISA tests are time-consuming, require highly specialized staff and specific laboratory equipment [Tighe et al. (2015)]. The development of a sensitive, compact and easy to use platform for real-time detection of cancer biomarkers would represent a major breakthrough in both clinical and research field.

Optical biosensors provide a valid alternative to ELISA for the detection of many kinds of biomolecules including tumor biomarkers [Tan et al. (2008),Ulber et al. (2003)]. Optical biosensing is based on two detection approaches, one making use of fluorescent labels and the other label-free [**?**]. Both methods have their advantages and drawbacks. Label-free techniques, like Surface Plasmon Resonance (SPR), are generally used to investigate in real-time the kinetics of surface-binding events. These provide quantitative information on both the specific recognition of a biomolecule and knowledge about the binding constants, such as the affinity [Dey et al. (2012),Guo (2012),Karlsson et al. (1991),Liu et al. (2008),Piliarik et al. (2007),Sikarwar et al. (2017),Ulber et al. (2003)]. While the latter is a unique and valuable feature of the label-free detection method, sensitivities are usually lower compared to the fluorescent counterpart [Huber et al. (1992),Mathias et al. (2007)]. For this reason, optical schemes exploiting evanescent waves, which feature strong field localization and intensity enhancement at the surface of interest, have been put forth [Anopchenko et al. (2016),Cooper (2002),Descrovi et al.

(2013),Fan et al. (2008),Fort and Grésillon (2008),Ligler and Taitt (2008),Pokhriyal et al. (2010),Zhao et al. (2010)]. Among evanescent wave sensors those based on Bloch surface waves (BSW) sustained by dielectric one dimensional photonic crystals (1DPC) was proposed and demonstrated as valid alternative to SPR for label-free optical biosensing [Konopsky et al. (2013),Paeder et al. (2011),Rivolo et al. (2012),Rizzo et al. (2014a),Shinn and Robertson (2005),Sinibaldi et al. (2015)]. The direct comparison of the performance of BSW and SPR biosensors showed that evanescent waves on all-dielectric structures can outperform their metallic counterpart [Sinibaldi et al. (2012)]. Furthermore, BSW were used to enhance the fluorescence emission from fluorescent molecules near 1DPC surfaces [Angelini et al. (2014a),Angelini et al. (2013),Badugu et al. (2013),Descrovi et al. (2010),Ray et al. (2015),Ricciardi et al. (2015)]. Although encouraging, all these experiments were conducted with biomarkers spiked in simple matrices such as phosphate buffered saline (PBS). In order to obtain clinically relevant results it is essential to perform the biomarker detection in more complex matrices such as blood plasma or other biological fluids.

In this thesis it is presented the detection of biomarkers in biological fluids by means of a compact and multifunctional point-of-care platform. The biosensing platform exploits BSW on disposable and low cost 1DPC biochips, whose unique design allows both label-free and fluorescence detection. The first chapter deals with a brief description of photonic crystals and BSW. It also illustrates the design and optimization of 1DPC for biosensing experiments. The second chapter focuses on the 1DPC production and the optical setup used. Chapter three describes the surface functionalization protocols adopted to make the 1DPC surface bio-compatible prior the bioassays. Chapter four will report on the biosensing experiments detecting angiogenic biomarkers in real world complex matrices like cell culture supernatant and human plasma samples.

Chapter 1

One dimensional photonic crystals and Bloch surface wave

In the last 20 years the development of new optical technologies has accelerated significantly. These technologies generally aim at the development of low cost optical systems designed for specific applications that have to be compact and robust. The goal is to control the optical properties of materials that in turn will control light. Fundamental components of these new optical systems are the class of materials known as *photonic crystals* (PC). A PC is a material in which an appropriate periodic refractive index variation is defined in one, two or three dimensions in space (Fig. 1.1).

Fig. 1.1 Simple examples of one, two, and three dimensional photonic crystals. The different colors represent materials with different dielectric constants. The defining feature of a photonic crystal is the periodicity of dielectric material along one or more axes.

A crystal is a periodic arrangement of atoms or molecules. The pattern with which the atoms or molecules are repeated in space is the crystal lattice. The crystal presents a periodic potential to an electron propagating through it, and both the constituents of the crystal and the geometry of the lattice dictate the conduction properties of the crystal. Importantly, however, the lattice can also prohibit the propagation of certain waves. There may be gaps in the energy band structure of the crystal, meaning that electrons are forbidden to propagate with certain energies in certain directions. The optical analogue is the photonic crystal, in which the atoms or molecules are replaced by macroscopic media with differing dielectric constants, and the periodic potential is replaced by a periodic dielectric function (or, equivalently, a periodic index of refraction). However, PC are not a new idea; in nature many biological systems exploit a sub-micrometric periodic structure of dielectric materials and Lord Rayleigh published one of the first analyses of the optical properties of multilayer films in 1887 [Rayleigh (1888)]. But it is only in the 80' that the PC concept was introduced together with that of photonic bandgap structure (PGB) [Yablonovitch (1987)].

Many of the most remarkable effects in these structures are related with the formation of forbidden gaps within the band structure. Indeed, if the dielectric constants of the materials in the crystal are sufficiently different, and if the absorption of light by the materials is minimal, which is true for dielectric materials, then the refractions and reflections of light from all of the various interfaces can produce many of the same phenomena for photons (light modes) that the atomic potential produces for electrons. The simplest possible photonic crystal, shown in Fig. 1.1 on the left, consists of alternating layers of material with different dielectric constants: a one dimensional photonic crystal (1DPC), practically a multilayer.
A multilayer made of an infinite number of planar layers of thickness d oriented perpendicular to the direction z is considered (Fig. 1.2) [Novotny and Hecht (2012)]. The dielectric constant of the layers is assumed to alternate between the values ε_1 and ε_2. The optical mode propagating inside the material is characterized by the wavevector **k**=(k$_x$, k$_y$, k$_z$). It is further assumed that both materials are non-magnetic, i.e. $\mu_1 = \mu_2 = 1$, and lossless. Two kinds of modes can be distinguished, TE modes, for which the electric field vector is always parallel to the boundaries between adjacent layers, and TM modes, for which the magnetic field vector is always parallel to the boundaries. Separation of variables leads to the following equations for the complex field amplitudes:

$$TE : \mathbf{E(r)} = E(z) e^{i(k_x x + k_y y))\mathbf{n}_x}, \tag{1.1}$$

$$TM : \mathbf{H(r)} = H(z) e^{i(k_x x + k_y y))\mathbf{n}_x}. \tag{1.2}$$

In each layer n, the solution for E(z) and H(z) is a superposition of a forward and a backward propagating wave, i.e.

$$TE: E_{n,j}(z) = a_{n,j} e^{ik_{z_j}(z-nd)} + b_{n,j} e^{-ik_{z_j}(z-nd)}, \tag{1.3}$$

$$TM: H_{n,j}(z) = a_{n,j} e^{ik_{z_j}(z-nd)} + b_{n,j} e^{-ik_{z_j}(z-nd)}. \tag{1.4}$$

where $a_{n,j}$ and $b_{n,j}$, are constants that depend on the layer number n and the medium ε_j. The longitudinal wavenumber k_{z_j} is defined as

$$k_{z_j} = \sqrt{\frac{\omega^2}{c^2}\varepsilon_j - k_\parallel^2}, \; k_\parallel = \sqrt{k_x^2 + k_y^2}, \tag{1.5}$$

with $k_\parallel$ being the parallel wavenumber. To find the constants $a_{n,j}$ and $b_{n,j}$ the boundary conditions at the interface are supplied $z = z_n = nd$ between the nth and the (n + 1)th layer:

$$E_{n,1}(z_n) = E_{n+1,2}(z_n), \tag{1.6}$$

$$\frac{d}{dz}E_{n,1}(z_n) = \frac{d}{dz}E_{n+1,2}(z_n), \tag{1.7}$$

$$H_{n,1}(z_n) = H_{n+1,2}(z_n), \tag{1.8}$$

$$\frac{1}{\varepsilon_1}\frac{d}{dz}H_{n,1}(z_n) = \frac{1}{\varepsilon_2}\frac{d}{dz}H_{n+1,2}(z_n). \tag{1.9}$$

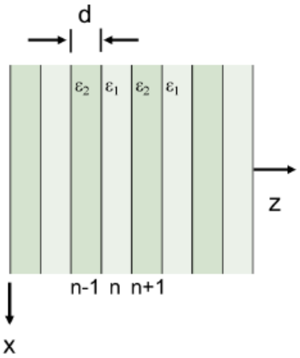

Fig. 1.2 A one-dimensional photonic crystal made of an infinite number of planar layers of thickness d.

Equation 1.7 is derived by expressing the transverse component of the magnetic field in terms of the electric field by using ∇× **E** = i $\omega\mu_0$ **H**. Similarly, Equation 1.9 follows from ∇× **H** = -i $\omega\varepsilon_0\varepsilon$ **E**. Inserting Equations 1.3 and 1.4 leads to

$$a_{n,1} + b_{n,1} = a_{n+1,2}e^{-ik_{z_2}d} + b_{n+1,2}e^{ik_{z_2}d}, \tag{1.10}$$

$$a_{n,1} - b_{n,1} = p_m\left(a_{n+1,2}e^{-ik_{z_2}d} - b_{n+1,2}e^{ik_{z_2}d}\right), \tag{1.11}$$

where $p_m \in (p_{TE}, p_{TM})$ is a factor that depend on the polarization as

$$p_{TE} = \frac{k_{z_2}}{k_{z_1}}\,(TE\,modes)\,,\; p_{TM} = \frac{k_{z_2}}{k_{z_1}}\frac{\varepsilon_1}{\varepsilon_2}\,(TM\,modes). \tag{1.12}$$

For a given mode type there are two equations but four unknowns, i.e. $a_{n,1}$, $b_{n,1}$, $a_{n+1,2}$, and $a_{n+1,2}$. Thus, more equations are needed. Evaluating the boundary conditions at the interface $z = z_{n-1} = (n-1)d$ between the (n-1)th and nth layers leads to

$$a_{n-1,2} + b_{n-1,2} = a_{n,1}e^{-ik_{z_1}d} + b_{n,1}e^{ik_{z_1}d}, \tag{1.13}$$

$$a_{n-1,2} - b_{n-1,2} = \frac{1}{p_m}\left(a_{n,1}e^{-ik_{z_1}d} - b_{n,1}e^{ik_{z_1}d}\right), \tag{1.14}$$

Although four equations for each mode type were derived, the number of unknowns were increased by two, i.e. by including $a_{n-1,2}$ and $b_{n-1,2}$. However, these two can be expressed in terms of $a_{n+1,2}$ and $b_{n+1,2}$ with the help of the Floquet–Bloch theorem. This theorem states that if E is a field in a periodic medium with periodicity 2d then it has to satisfy

$$E(z+2d) = e^{ik_{Bl}2d}E(z), \tag{1.15}$$

where k_{Bl} is a wavevector, called the Bloch wavevector. A similar equation holds for the magnetic field H(z). Application of the Floquet–Bloch theorem leads to

$$a_{n+1,2} + b_{n+1,2}e^{-2ik_{z_2}[z-(n-1)d]} = e^{ik_{Bl}2d}\left(a_{n-1,2} + b_{n-1,2}e^{-2ik_{z_2}[z-(n-1)d]}\right). \tag{1.16}$$

Since this equation has to hold for any position z, it needs to be required that

$$a_{n+1,2} = a_{n-1,2}e^{ik_{Bl}2d}, \tag{1.17}$$

$$b_{n+1,2} = b_{n-1,2}e^{ik_{Bl}2d}, \tag{1.18}$$

which reduces the number of unknowns from six to four and allows to solve the homogeneous system of equations defined by Equations 1.10- 1.14. The system of equations can be written in matrix form and the determinant must be zero in order to guarantee a solution. The resulting characteristic equation turns out to be

$$cos(2k_{Bl}d) = cos(k_{z_1}d)cos(k_{z_2}d) - \frac{1}{2}\left(p_m + \frac{1}{p_m}\right)sin(k_{z_1}d)sin(k_{z_2}d). \tag{1.19}$$

Since $\cos(2k_{Bl}d)$ is always in the range [-1...1], solutions cannot exist when the absolute value of the right-hand side is larger than unity. This absence of solutions gives rise to the formation of bandgaps. For each Bloch wavevector k_{Bl} one finds a dispersion relation $\omega(k \parallel)$. If all possible dispersion relations are plotted on the same graph one obtains a so called band diagram. An example is shown in Fig. 1.3, where the shaded areas correspond to allowed bands for which propagation through the crystal is possible. Notice that propagating modes exist even if one of the longitudinal wavenumbers (k_{z_j}) is imaginary. The Bloch wavevector at the band edges is determined by $k_{Bl}d = n\pi/2$. For a given direction of propagation characterized by $k_\parallel$ one finds frequency regions for which propagation through the crystal is possible and frequency regions for which propagation is inhibited. However, for a 1DPC there is no complete bandgap, i.e. there are no frequencies for which propagation is inhibited in all directions. If a wave propagating in vacuum is directed onto the photonic crystal, then only modes with $k_\parallel$ smaller than $k = \omega/c$ can be excited. The vacuum light-lines are indicated in Fig. 1.3 and one can find complete frequency bandgaps inside the region $k_\parallel < k$.

The band gap in a dielectric truncated 1DPC can be exploited to obtain guiding of a surface mode, thus giving rise to surface sensitive evanescent field sensors [Konopsky et al. (2013)]. These surface modes are called Bloch Surface Waves (BSW) and can be excited by prism coupling in the well known Kretschmann–Raether configuration. The following paragraphs address the optimization of a BSW optical sensor based on a periodic 1DPC.

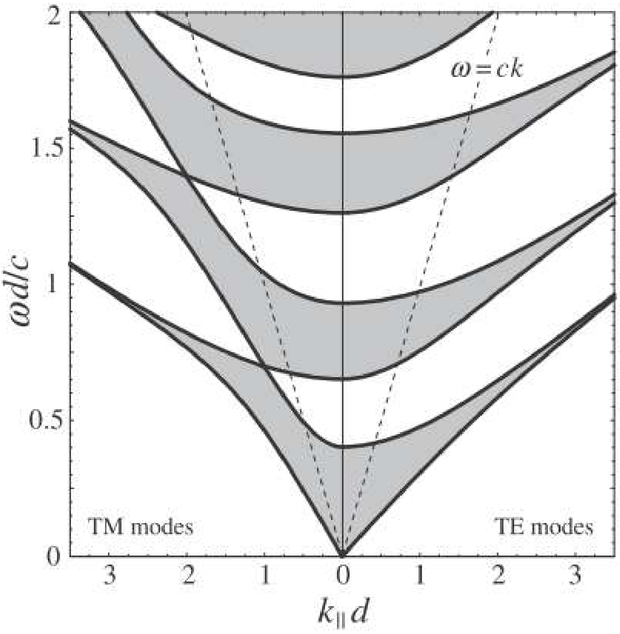

Fig. 1.3 The band diagram for a 1DPC photonic crystal. The shaded areas are the allowed bands. The diagram represents both TE and TM modes.

1.1 Optimization and design

Under total internal reflection (TIR) conditions, BSW may be revealed by a very narrow dip in the angular reflectance spectrum, whose angular position depends on surface perturbations and is used, for example, as a probe of molecular binding events at the 1DPC surface. Here, a semi-analytical resonance model is applied to discuss the effect of the detection noise on the resonance shift determination for angularly resolved reflection analysis. Combining the results with the values obtained for a *figure of merit* (FoM) of such sensors yields the *limit of detection* (LoD), which is governed by the resonance properties as well as by its sampling. Besides the choice of the detector, such sampling depends also on the (angular) range to be detected. Moreover, both quantities, LoD and FoM, are simulated for SPR and are used for a sample optimization of a low loss dielectric thin film stack sustaining BSW.

Part of this section have been published in Rizzo et al. (2014a), all the calculations reported were carried out by means of self-written software that is based upon a transfer matrix formalism (TMM). Using this tool the angularly resolved, monochromatic reflectivity of the thin film system is simulated in the plane wave approximation when the sensor stack is illuminated from the (glass) substrate. The interface between substrate back side and air is neglected. The numerical procedure is readily illustrated in the inset of Fig. 1.4. First, the angularly resolved reflectivity is calculated for the stack covered with water like medium of n_A = 1.33 refractive index (curve 1 in Fig. 1.4(A)). From this curve the depth D and the full with at half depth W are determined. Second, a 10 nm thick organic layer (refractive index n_{org} = 1.45) is added to calculate curve 2 in Fig. 1.4(A). The sensitivity S [deg/nm] is derived from the minima positions of curves 1 & 2. Third, the maximum signal is assumed to be detected with 10 nm thick organic layer and an increased solution refractive index n_A = 1.36 thus yielding resonance 3 as shown in Fig. 1.4(A). The angular range included between the upper limit of the half depth of curve 3 and the lower limit of the half depth of curve 1 is used as an estimation of the angular range A to be detected. These assumptions consider the standard label-free operation range only.

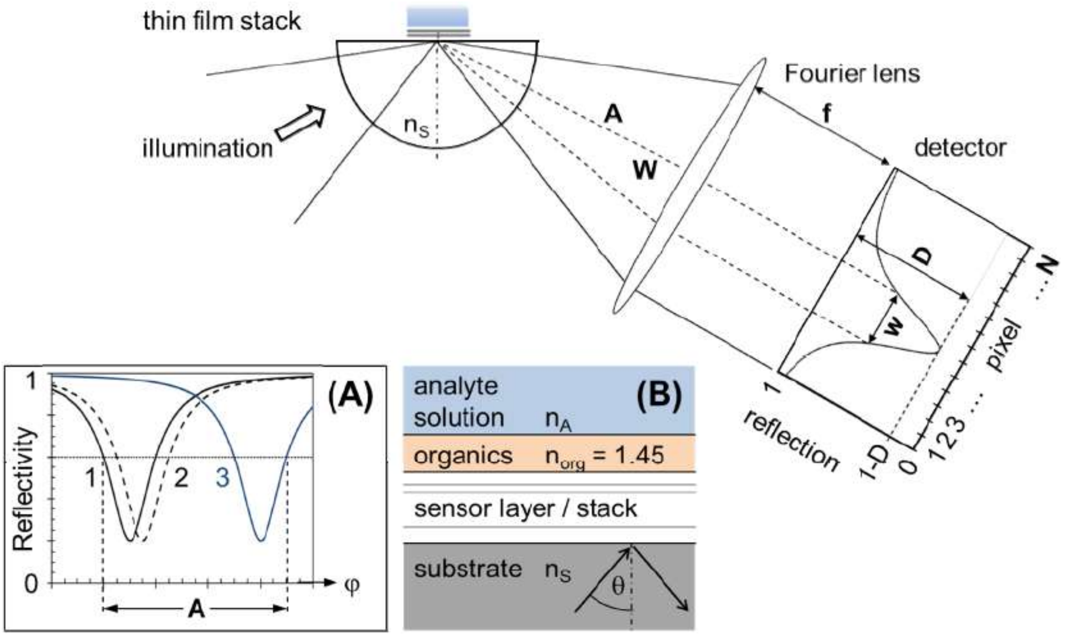

Fig. 1.4 Scheme of angular resonance detection by means of a Fourier imaging approach utilizing a lens with focal length f. The angular range A is discretized with N detector pixels that transform the angular width W of the resonance into a width w in terms of detector pixels. Inset A illustrates that discretization needs to resolve small signal shifts (curves 1 and 2) but is practically limited by the free measurement range (curve 3). Inset B illustrates the general stack that yields signal shifts due to organic layer adsorption as well as changes of analyte refractive index n_A.

1.2 Basic experimental scheme and noise estimation

A sketch of the experimental scheme used to measure angularly resolved reflectivity is shown in Fig. 1.4. The optical functions of half ball and Fourier lenses will be combined within the chip substrate to create small systems with disposable chips that will be shown later. A monochromatic analysis is considered here in order to leave material dispersion effects out of the discussion. Then the angular spectrum of reflected light intensity is detected by means of an array detector with N pixels. The surface mode resonance observed in the reflected angular spectrum is characterized by a depth D and an angular width W (capital letter W) given in degrees. Sampling by the detector with limited dynamic range yields a discretized curve exhibiting a width w (lower case letter 'w') measured in detector pixels. The latter width is assigned the unit *pix* to distinguish w and W.

The sensitivity S_{bulk} is usually defined as the shift of the resonance position (degrees) due to bulk refractive index changes (RIU). Such value can be easily determined experimentally when using liquids with different refractive indices. In the current frame this definition is misleading. Dielectric systems allow for positioning the resonance at any (angular) position. As will be exemplified later, the sensitivity also depends on the resonance position which governs the penetration depth of the evanescent field into the (aqueous) analyte solution. Defining the sensitivity over the bulk refractive index of this analyte solution will yield maximum sensitivity at the angle of total internal reflection because then the evanescent field is infinitely extended into this medium. Therefore, sensitivity S_{layer} is defined as the signal given in degrees relative to an organic layer thickness change given in nanometer, while assuming a refractive index of $n_{org} = 1.45$ for such layer. In order to evaluate the sensor performance the effect of the resonance width and depth on the noise of the sensor output (resonance shift) needs be quantified. A simplified square polynomial model that mimics fitting the resonance in the region of minimum reflectivity is assumed for this analysis and sketched in Fig. 1.5(A). It could directly represent an experiment that saturates the detector outside the angular range around minimum reflectivity. The approach

$$y(x) = a_2 \cdot x^2 + a_1 \cdot x + a_0 \Rightarrow x_{min} = -\frac{a_1}{2 \cdot a_2} \Rightarrow \Delta x_{min} = \left|\frac{\Delta a_1}{2 \cdot a_2}\right| + \left|\frac{\Delta a_2}{a_2} \cdot x_{min}\right|. \quad (1.20)$$

is used to derive x_{min} because of its linearity with respect to all fit parameters. The error for the minimum position determination depends on x_{min} itself because the uncertainty on the two parameters a_1 and a_2 is correlated and not independent. However, Eq. 1.20 can be applied in the case $x_{min} \sim 0$ in order to estimate the noise effect. According to the illustration in Fig. 1.5(A) the depth D and width w of the resonance completely define a quadratic polynomial for a given dynamic range of the detector. So the parameters a_i and thus x_{min} are known exactly, and the parameter errors Δa_i are determined numerically from the diagonal elements of the covariance matrix C according to $\sigma^2(a_i) = C_{ii}$ [Ziegel et al. (1987)]. This allows one to model the measurement noise by assuming an intensity uncertainty σ_i associated to each pixel's intensity value y_i. The detection shot noise $\sigma^2 \sim y_i$ is considered, assuming it to be 0.6% of light intensity as previously suggested [Piliarik and Homola (2009)], and the digitization error, assuming one count of the analog-to-digital converter.

In the case of extremely narrow resonances one has also to consider effects due to limited sampling (discretization). This is illustrated in Fig. 1.5(B) for an arbitrary continuous function f(x). The intensity detected by each pixel corresponds to a spatial integration and results in the error

$$y_i = \frac{1}{\Delta x} \cdot \int_{x_i - \Delta x/2}^{x_i + \Delta x/2} f(x) \cdot x \rightarrow \Delta y_i = y_i - f(x_i) = -\frac{(\Delta x)^2}{24} f''(x_i) - O\left(f^{(4)}; (\Delta x)^4\right). \tag{1.21}$$

This discretization error is proportional to the second derivative of the function under consideration. It is worth to point out explicitly that in the square polynomial approximation a constant intensity offset ($\sim a_2$) is added to the data. So it cannot be considered noise and might be dropped for the present analysis. But, similar effects are introduced by mechanical vibrations of the setup that will yield higher order errors when fitting real data. Therefore the simulation results will be shown with and without inclusion of the discretization noise effect. The total contribution of shot noise, digitization error and discretization error are then given by the lowest order of approximation from Eq. 1.21 and yield a total intensity uncertainty in each pixel

$$\sigma_i^2 = 1 + \frac{6}{1000} \cdot y_i + \left(\frac{a_2}{12}\right)^2. \tag{1.22}$$

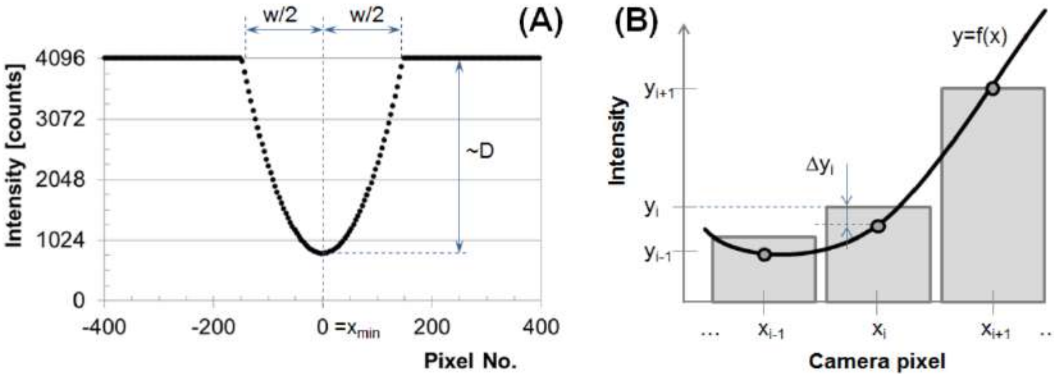

Fig. 1.5 (A) Simplified model of resonance analysis using a quadratic polynomial to mimic the resonance sampled by a 12 bit dynamic range detector. (B) Discretizing a function by spatially extended pixels corresponds to a spatial integration of the distribution and yields discretized intensity values $y_i(x_i)$ that differ from the ideal distribution $f(x_i)$ by an amount y_i.

Calculating the result of Eq. 1.20 when assuming the noise according to Eq. 1.22 yields the results shown in Fig. 1.6 In order to cross check such error estimation an additional numerical experiment has been performed by adding numerical noise to a Lorentzian function of width w and depth D = 0.7. The standard deviation of the minimum position is deduced from fitting 1'000 different noise representations. The points shown in Fig. 1.6(B) almost perfectly match the results of the square polynomial model for sufficient resonance widths.

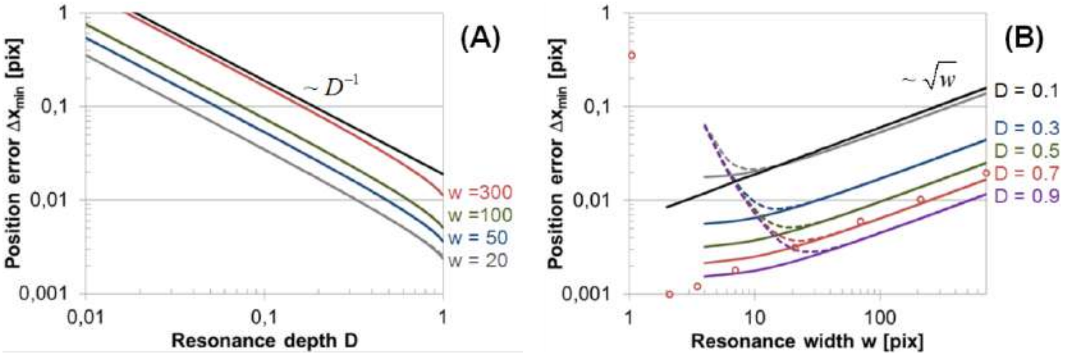

Fig. 1.6 (A) Error of minimum position determination with respect to resonance depth for different widths of the resonance; the black line illustrates a 1/D behavior. (B) Minimum position error vs. resonance width for different depths of the resonance; the black line depicts the asymptotic behavior. The dots illustrate uncertainties obtained from fitting Lorentzian curves of width w with added numerical noise. All simulations assume a detector with 12 bit dynamic range; the solid and the dashed curves give the error without or with inclusion of the discretization error, respectively.

The results obtained by such numerical calculations can be summarized by the following three major points:

1. According to Fig. 1.6(A) the accuracy of minimum determination is well proportional to the inverse depth (~1/D) of the resonance. Deviations occur for very deep resonances (D>0.7) due to the fact that low intensities near the minimum suffer from shot noise less. This law corresponds well to previous findings [Piliarik and Homola (2009)].

2. The effect of the width onto the noise is well approximated by a $x^{1/2}$ law in the asymptotic case of large resonance widths. Such result confirms the previous findings [**?**,Rizzo et al. (2014b)]. Enormous deviations appear for bad sampling in the w<30 pix range when assuming the discretization error to be noise. As its contribution is deterministic according to Eq. 1.6 this assumption is debatable, and both models yield different suggestions for optimum resonance width. But it reflects the fact that fitting the intensity distribution of very narrow resonances might not be the method of choice anymore, and resonance width shall be ensured to exceed a value around 10 *pix*. This result underlines that strongly decreasing resonance width requires special attention in order to maintain proper sampling of the distribution.

3. Aside from such very narrow resonances the diagrams in Fig. 1.11 enable one to extract an upper limit for the uncertainty of minimum determination according to

   $$\Delta x_{min} \leq \alpha \sqrt{w}/D. \tag{1.23}$$

   The noise decreases when increasing the dynamic range of the detector (data not shown). As an example, with the assumptions outlined above and the unit *pix* for the number of detector pixels, $\alpha_{12bit} = 6 \cdot 10^{-4}\sqrt{pix}$ and $\alpha_{8bit} = 2.8 \cdot 10^{-3}\sqrt{pix}$ were obtained as factor of proportionality in Eq. 1.23 when considering the noise levels obtained for 12 and 8 bit dynamic range detection, respectively. This can be compared to previously reported experimental data [Rizzo et al. (2014b)],where for a resonance with D = 0.15 and w = 32.4 pix experimentally was obtained $\Delta x_{exp} = 0.12$ pix for a 8 bit detection. This is almost exactly the prediction $\Delta x_{exp} = 0.11$ pix of the above model. Therefore Eq. 1.23 can be applied to the biosensors performance estimation carried out below.

4. The diagram in Fig. 1.6(B) reveals a lower limit that depends on the detector dynamic range and the discretization noise only. For the case of 12 bit dynamic range detection the accuracy limit is in the $10^{-3} \div 10^{-2}$ pix range, depending on the magnitude of the discretization noise.

1.3 Figure of merit and limit of detection

A FoM has been defined elsewhere [Sinibaldi et al. (2012)] in order to compare the performance of different sensor approaches. It relates the depth D and width W of the resonance to the sensitivity S according to

$$FoM = D \cdot \frac{S}{W}. \tag{1.24}$$

Such FoM has been shown analytically to be maximized for intensity measuring systems without spectral or angular resolution [Sinibaldi et al. (2013)]. Using the sensitivity S and the sensor output noise σ_S suggests using another assessment criterion referred to the LoD [Piliarik and Homola (2009)] according to$LoD = \sigma_S / S$. Note, that the choice of $S = S_{bulk}$ or $S = S_{layer}$ determines the unit of the LoD, so it applies to both kinds of sensitivities. With the results of the previous section it can be obtained

$$LoD \leq \alpha \cdot \frac{\sqrt{w}}{D \cdot S}. \tag{1.25}$$

According to Fig. 1.4, where the angular range A is sampled by N pix, the detector's pixel and angular scales are connected by $\sigma_{[\mathrm{deg}]} = \sigma_{[pix]} \cdot A/N$ and $w = W \cdot N/A$ accordingly. Applying both conversions and combining them with Eq. 1.25 yields

$$LoD \leq \alpha \cdot \frac{\sqrt{W}}{D \cdot S} \cdot \sqrt{\frac{A}{N}} = \alpha \cdot \frac{1}{FoM \cdot \sqrt{w}}. \tag{1.26}$$

that needs to be minimized for sensor optimization. Due to the fact that the angular sampling is determined by the angular range analyzed by the detector, the LoD in Eq. 1.26 also contains he angular range A of observation, which needs to consider the free measurement range as well as practical tolerances of the system.

In the limiting case, when the detection system samples exactly the resonance width, one obtains the minimum $LoD|_{A=W} \sim \alpha \; / \; \left(FoM \cdot \sqrt{N}\right)$. Combining it with the fact that FoM has been shown to apply to intensity only experiments strictly [Sinibaldi et al. (2013)], the sensor performance measured by the FoM shall be used in the case of a small angular detection range $A \sim W$. Whenever a larger range needs to be detected, e.g. in case of parallel angularly resolved measurement [Danz et al. (2011),Chinowsky et al. (2007),Naimushin et al. (2002)], if the free measurement range including tolerances needs to be considered, or if fluorescence collection is desired as well [Sinibaldi et al. (2014)], the optimization should minimize the LoD that also considers the resonance sampling. Thus, optimum sensor performance can only be achieved with good FoM in combination with a sufficient sampling of the resonance. In the following section the different meanings of the LoD and FoM as performance measures will be illustrated by discussing different types of plasmon like sensors.

1.4 Numerical evaluation

1.4.1 Surface plasmon resonance

First, surface plasmon sensing will be discussed as a reference. The thickness of the metal layer is the only free parameter in the 'stack design' once the metal has been chosen. So different gold layer thicknesses on a glass substrate made of nBK7 are assumed to be used for sensing. The optical constants of gold are taken from [Palik (1998)]. Calculation results are summarized in Fig. 1.7 for convenience. Both, the FoM obtained according to Eq. (5) and the LoD according to Eq. 1.26 exhibit local optima in the 800..850 nm spectral range when utilizing 45..55 nm gold layer thicknesses. This implies to preferably use this wavelength range for sensing issues as being done currently [Danz et al. (2011),Remy-Martin et al. (2012)]. With the assumptions used here the LoD of such sensors should reach the picometer range. This result needs to be cross checked with previous findings. The present calculation yields a surface sensitivity of $S \sim 0.05\,\mathrm{deg}\,/\,nm$ that corresponds to a bulk refractive index sensitivity of$S \sim 100\,\mathrm{deg}\,/\,RIU$. These data enable to convert $\Delta d_{min} \sim 0.8$pm into $\Delta n_{min} \sim 3 \cdot 10^{-7}$RIU, which agrees very well with previous experimental findings [**?**,Piliarik et al. (2009)]. So the noise levels applied to the LoD simulation yield a valid order of magnitude approximation.

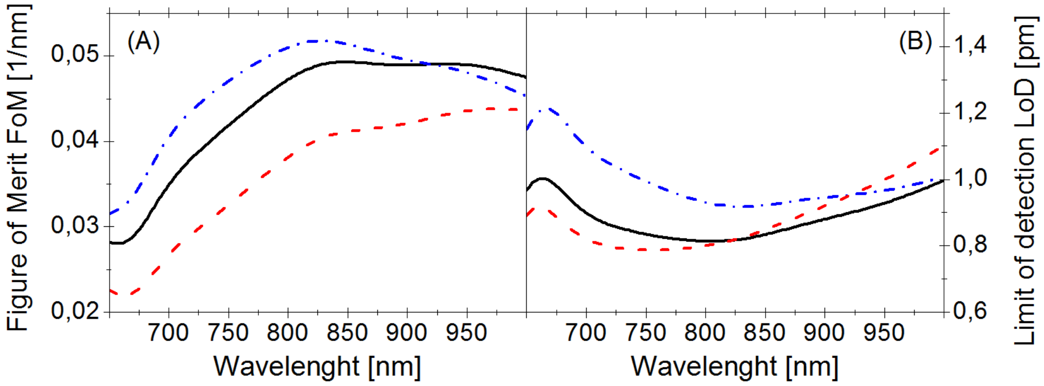

Fig. 1.7 Calculation results obtained for sensitivity figure of merit FoM (A) as well as limit of detection LoD (B) vs. wavelength (650 nm $<\lambda<$ 1'000 nm) for the case of 45 nm (dashed red), 50 nm (solid black) and 55 nm (dashdot blue) thick gold layers. LoD has been calculated assuming the value N = 1'000 pix.

1.4.2 Bloch surface waves

As pointed out in the introduction the resonance width can be dramatically decreased when working with low loss dielectric stacks supporting Bloch surface waves. Now more parameters can be accessed to tailor the sensor's performance and their range of variation explored. Besides the wavelength of operation the choice of two materials, their thicknesses, and the number of periods need to be considered. In order not make confusion with a too general and possibly heavy description, it is sufficient to focus the attention on an exemplary case to put into evidence the potential of BSW for sensing applications and develop a strategy to design an optimized 1DPC.

As case of study the following structure is discusses at the wavelength λ = 670 nm: substrate $|L|(HL)^{N_p}$ | water, where N_p is the number of the periods that will vary between 4 and 6. The materials Ta$_2$O$_5$ ($n_H = 2.106 + 3.5 \cdot 10^{-5} i$) and SiO$_2$ ($n_L = 1.474 + 6 \cdot 10^{-6} i$) are being used as high (H) and low (L) refractive index layers, respectively. Comparable stacks [Munzert et al. (2003)] have been recently applied for other BSW sensors [Sinibaldi et al. (2013),Sinibaldi et al. (2012),Sinibaldi et al. (2014)]. The substrate index n_S = 1.514 is chosen similar to the SPR case at the corresponding wavelength. Fixing these prerequisites leaves the number of periods N_p and the two thicknesses of the high (d_H) and the low (d_L) refractive layers open for optimization. The optimization procedure developed for the present case can be extended to stacks based on different materials, different spectral ranges and also to aperiodic stacks.

At first the optimization will focus on maximum sensitivity because this value determines the resonance shift that can be observed. The maps of the calculated layer (S_{layer}) and bulk (S_{bulk}) sensitivities, obtained by scanning d_L and d_H with a 10 nm and 5 nm step size, respectively, are shown in Fig. 1.8 for three different values of N_p. Regions without resonance appear for very thin stacks, i.e., in the lower left corner of the diagrams in Fig. 1.8 (shown in black). This is caused by the fact that the BSW at the given λ is below its cut-off. Two interesting results can be derived from this analysis. First, the influence of the number of periods N_p on the BSW sensitivity is negligible, that is to say, the sensitivity variation with the number of periods is below 1.5% only for all points in the graph. Second, optima of S_{layer} appear in a narrow, nearly line shaped region near the BSW cut-off. In such region, the optimum thicknesses of high and low index materials are surprisingly correlated by the linear law d_L = - d_H + C, with C = 452.5 nm for the stack design considered here and operating at the given λ, as shown in Fig. 1.9(A). Fig. 1.9(B) illustrates the sensitivity along such a line: the mean value is 0.02 °/nm and the extrema differ by 0.6% only, thus proving that along such a line a similar maximum can be found for all values of N_p. In contrast, the bulk index sensitivity S_{bulk} is maximized at the TIR edge, where the evanescent fields exhibit maximum penetration into the aqueous analyte medium. Fig. 1.8 illustrates that bulk sensitivity is no proper target for BSW biosensor optimization.

The resonance position and the angular range according to Fig. 1.4(A) are shown in Fig. 1.10 for N_p = 5 only. Other N_p values yield similar maps with a change of 0.01% for the resonance angle (θ_{BSW}) and 2% for the angular range (A) only. A monotonic behavior is observed when increasing the layers' thickness; the resonance position shifts towards larger angles and the angular range towards smaller values. Interestingly, the S_{layer} optimized stacks exhibit almost the same resonance angular position, i.e., maximum S_{layer} is achieved at a fixed propagation constant of the surface wave (dashed line in Fig. 1.10(A)). The angular range has been determined for a 10 nm organic layer thickness increase only, therefore it is governed by bulk index effects, as confirmed by Fig. 1.10(B) that qualitatively resembles the S_{bulk} map shown in Fig. 1.8.

Once discussed the sensitivity, the dependency of the remaining parameters contributing to the LoD, as defined by the Eq. 1.26, on the layers thickness needs

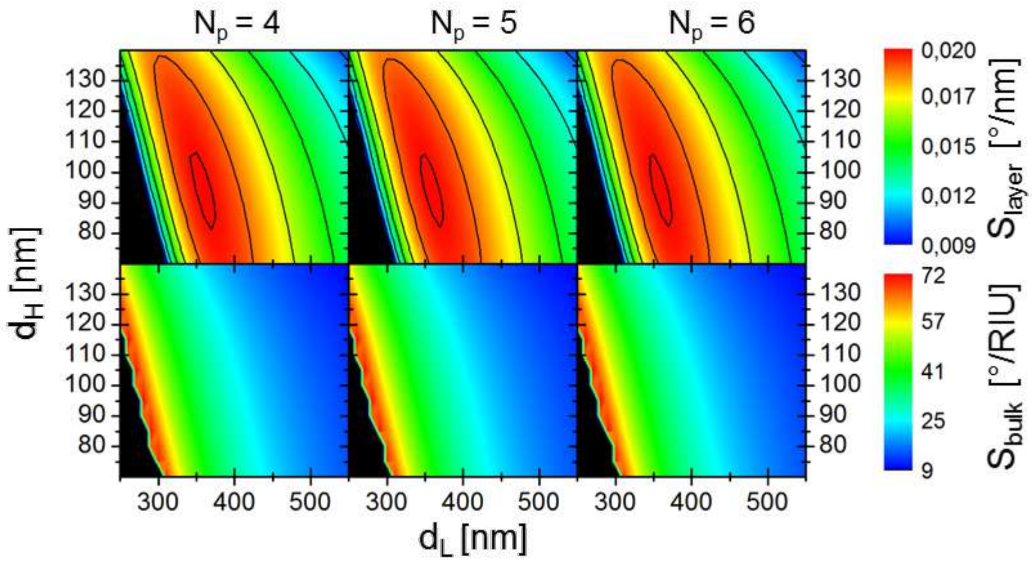

Fig. 1.8 Sensitivity with regard to thin film binding S_{layer} (top row) and with regard to bulk index changes S_{bulk}(bottom row) for the dielectric BSW systems subs $|L|(HL)^{N_p}|$water with different number of periods. S_{bulk} is based on an external refractive index change of 0.01 starting from n_A = 1.33.

to be analyzed in order to optimize the performance of the BSW sensor. Especially the resonance depth D and width W are highly influenced by the number of periods, because this modulates the radiative losses into the substrate [Sinibaldi et al. (2013)]. This is confirmed by the results shown in Fig. 1.11. For large N_p = 5,6 the smallest W is obtained close to the TIR edge (boundary of the dark region), whereas for N_p = 4 the resonance width seems to suggest an optimum high index layer thickness in the range d_H = 90..100 nm. Generally, the W values span over two orders of magnitude for the simulated structures and decrease when increasing N_p. The region where the maximum D is obtained shifts towards smaller thicknesses of the low index layer as the number of periods increases, following a sort of parabolic shape with the high refractive index layer thickness.

In general, the number of periods should be utilized to adapt the system onto changes of the material losses. Increasing such material losses requires decreasing the number of periods, because this increases radiation losses. Such case might be desired in order to simplify the stack or to increase resonance width and is similar to the plasmon case [Professor Dr. Heinz Raether (1988)].

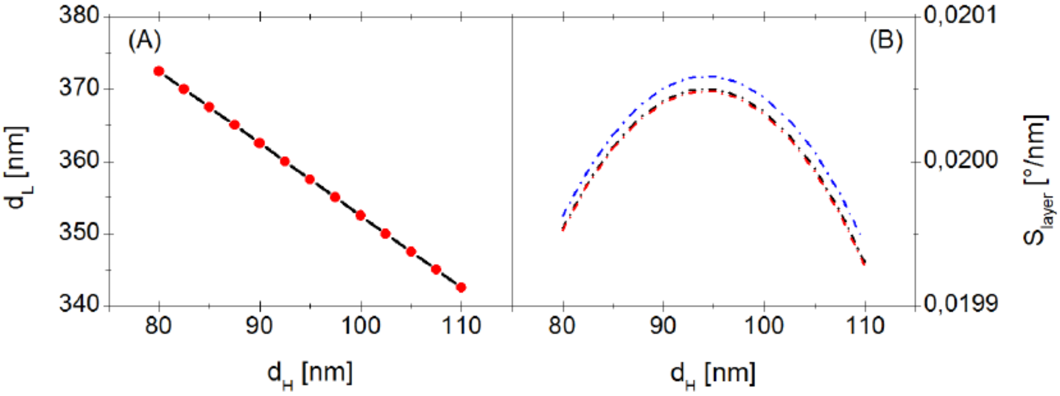

Fig. 1.9 (A) Extrapolated pairs $d_L = f(d_H)$ from Fig. 1.8 with optimum sensitivity S_{layer}. The linear law $d_L = -d_H + 452.5$ nm that correlates the two thicknesses is unequivocally. Along this line the sensitivity (B) varies by 0.6% only and has a mean value of 0.020 °/nm.

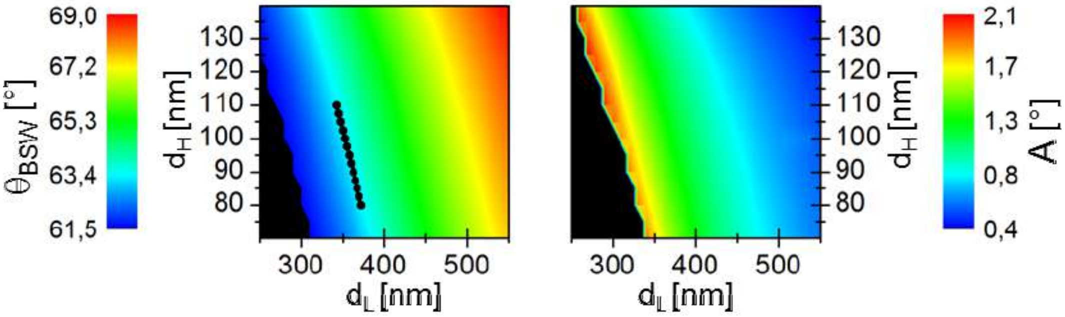

Fig. 1.10 Resonance position (A) and angular range (B) for the BSW stack subs $|L|(HL)^5|$ water determined according to Fig. 1.4(A). The white dashed line indicates S_{layer} optimized stacks according to Fig. 1.9(A).

Combining all resonance features enables one to compile FoM and LoD maps as shown in Fig. 1.12. Tuning the number of periods in the stack allows one to generate a large region (N_p =5) with minimum LoD values in the range LoD_{min}>0.04 pm. For the case $N_p = 6$ small regions with comparable low values are found. The most important contribution to the formation of such extended range of well suited stacks with $N_p = 5$ is the fact that sensitivity S and resonance depth D are maximized in the same region of the map. Alternatively, this effect could be achieved by adjusting the absorption losses of the stack materials. But this will increase the resonance width, which in turn results in an increased LoD.

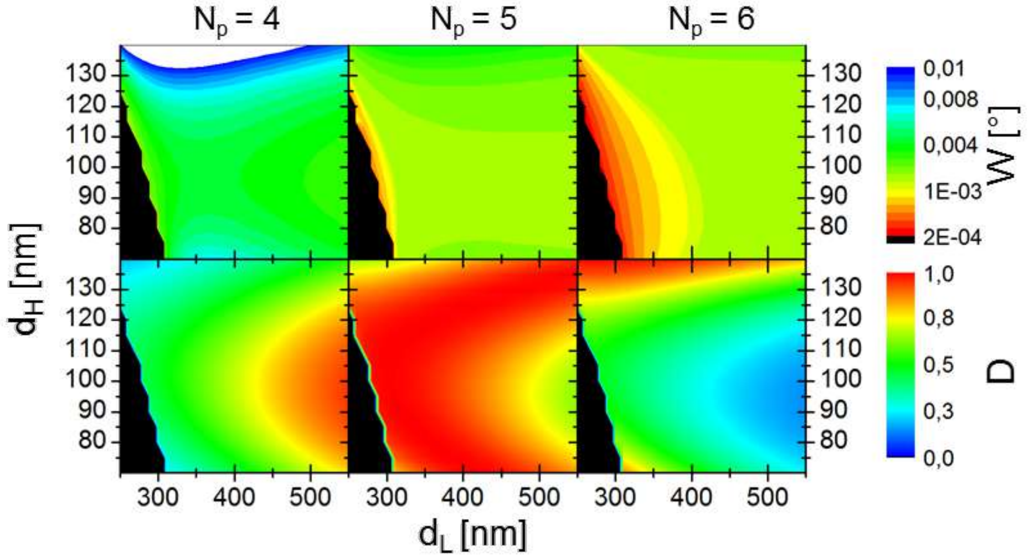

Fig. 1.11 Resonance full width half maximum W (first row) and depth D (second row) for the BSW stacks subs $|L|(HL)^{N_p}$ | water with N_p = 4,5,6 (columns).

1.5 Considerations about the sensitivity

The interesting resonance properties obtained for the exemplary stack discussed here require some further discussion. First, the sensitivity has been found to be independent of the number of periods. This can be explained by the reflection of the surface wave at the substrate side dielectric stack: for the angles under consideration, the phase of such reflection is almost independent of the number of periods. Because of the large index difference of n_L and n_H, deviations occur for lesser numbers of periods only. Second, the surface sensitivity S$_{Layer}$ exhibits a clear optimum near the TIR edge with the optimum angle being well separated from this edge. Such effect is associated with the TIR at the interface to the analyte medium and will be discussed in detail elsewhere. The optimum performance for the exemplary BSW sensor achieved here reaches FoM_{max} ~24 nm^{-1} that is more than two orders of magnitude above that of SPR. But, minimum LoD_{min} ~0.04 pm is 'only' a factor 20 below that of SPR. This illustrates that the superior finesse of BSW sensors, that could be associated with the ratio S/W, can be partially translated into LoD reduction only. As the sensitivity governs the angular range to be detected, it simultaneously limits the sampling of the angular distribution and increases the noise of resonance position determination. In our calculations a N

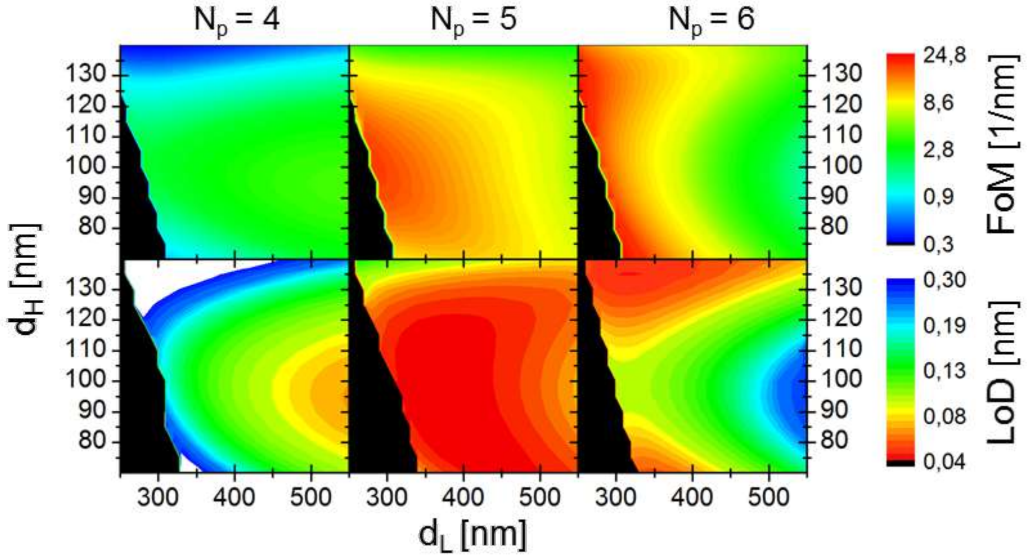

Fig. 1.12 Simulated FoM (top row) and LoD (bottom row) assuming 1'000 pix detector for different number of periods (columns).

= 1'000 pix detector has been assumed, while W~0.001° and A~1° for optimized stacks has been obtained. This illustrates that sampling will tremendously affect reflection intensity based resonance analysis. With regard to Fig. 1.6(B) such superior performance requires one to improve the detector sampling along with the mechanical stability of set-up. Note, that even varying the number of periods in an optimized stack (d_L ~360 nm, d_H ~95 nm) from N_p = 5 to N_p = 4 or 6 will reduce the LoD and FoM but still yield a performance improvement when comparing to SPR. Furthermore, the large region of layer thicknesses for optimized stacks in the N_p = 5 indicate that limited fabrication accuracy will not constrain the sensor performance.

1.6 Coupled fluorescence

It is well known that the fluorescence generated by an emitter can be strongly modified by the photonic environment. In analogy with the density of electronic states (DOS), the Local Density of electromagnetic States (LDOS) stands for the available electromagnetic modes in which photons can be radiated from a specific location. The emission from a dipole-like source in free-space results in a spherical isotropic radiation pattern because of the infinite eingemodes of the vacuum.

However, when the emitter is in close proximity to a 1DPC, in which the dielectric constant varies spatially on the length scale of the same order of the emitted wavelength, the decay properties of the emitter are modified according to the photonic band structure and so is the radiation pattern. This effect will be used to provide a tandem detection mode, i.e. label-free/fluroescence, for a BSW biosensing platform. Moreover, The emitter can be excited by a BSW on the interface between a truncated 1DPC and an external medium. Due to the fact that BSW works in TIR conditions, only molecules near the surface (within the exponentially decreasing intensity distribution of the evanescent field in the external medium) will be excited (Fig. 1.13).

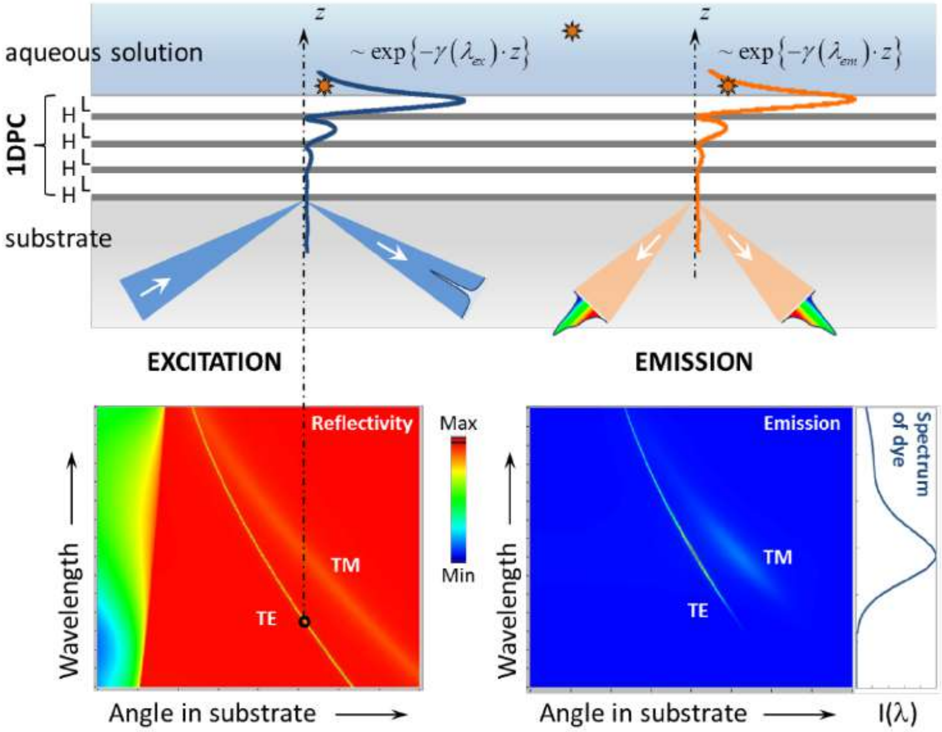

Fig. 1.13 Illustration of the basic effects arising when exciting and observing fluorescence on top of a BSW supporting thin film stack. Excitation is shown on the left and emission on the right side.

Fluorescence excitation exploits the same effect of field enhancement that is utilized for label-free sensing. Then, maximum interaction of the emitter on the surface with the light wave impinging from the substrate is reached. Once excited, the molecules emit the energy into all electromagnetic modes of the system. In this process, modes with increased energy density at the emitter position are preferably excited. In result, the field enhancement of the BSW excitation forces

the energy to be emitted into the dispersion of the BSW stack (Fig. 1.13).
BSW coupled emission has been studied using the tool *Radiating Slabs* (Fraunhofer IOF) and that has been applied successfully in a quantitative manner to emission problems in stratified media previously. Parameters like number of layers and resonance angles have been varied to optimize the fluorescence detection. In result, a few summaries and/or conclusions can be drawn from these optimizations: increasing the number of layers (periods) in a BSW stack does not improve fluorescence detection efficiency. But it decreases the emission resonance width. The reason for such results seems be twofold: first, extinction in the layers causes elevated losses when increasing the total thickness. Second, increasing the stack thickness introduces (more) guided modes that can drain the energy of the excited emitting molecules. Optimizing algorithm tries to achieve TE and TM resonant emission at similar angles close to the TIR edge, because the sum of both polarizations has been set as figure of merit. All of the results are local (numerical) optima. There is no proof that such results are global optima. Therefore, any later label-free based stack analysis will have to explicitly review the effect of the stack onto the fluorescence.

Chapter 2

Production of 1DPC and optical setup

The thin film stack has to fulfill several tasks in order to achieve appropriate operations of the sensor system: it needs to exhibit correct resonance properties (according to the design) as well as to provide convenient surface properties for later biochemical functionalization and immobilization. Moreover, the fabrication method has to be reliable in terms of a subsequent series production with very low tolerances and with a high number of substrates that can be coated in a single deposition run. For this reason although two deposition techniques were, i.e. plasma enhanced chemical vapor deposition (PECVD) and plasma-ion assisted vacuum evaporation (PIAD), only the 1DPC coated with the latter method were used for the biosensing experiments. Furthermore, PIAD has the possibility to deposit coatings with an adjustable densification and stoichiometry at low substrate temperature which make the technique suitable for the deposition of the 1DPC on polymeric substrates.

2.1 Plasma Enhanced Chemical Vapor Deposition

Silicon-based alloys have been studied in order to check the feasibility of their use in the fabrication of 1DPC sustaining BSW. Silicon-based amorphous thin-film alloys are materials of considerable interest and have been studied extensively by the scientific community for a wide range of applications, including microelectronics [Wu et al. (2014),Pomorski et al. (2014),Kim et al. (2003)], photovoltaics [Shi et al. (2013),Wan et al. (2013)], tribology [Jiang et al. (2014)], biomedicine

[Mandracci et al. (2008)] and photonics [Luo et al. (2013),Lin et al. (2015)]. An important characteristic of these materials, which is related to their amorphous structure, is the possibility of finely adjusting the relative amount of the elements that compose the alloys, thus allowing their physical and chemical properties to be tuned. These features can be exploited when these materials are grown by means of plasma enhanced chemical vapor deposition (PECVD), since this technique allows the element incorporation to be controlled by changing the percentage of the feedstock gases in the reactor [Mandracci and Ricciardi (2007)] with a thickness control at the nanometric scale [Giorgis et al. (1999)]. The PECVD is a modification of the CVD process, in which a plasma is used as a source of energy in order to obtain the dissociation of the reactive gases at temperatures at which they would not dissociate thermally. A plasma can be described as a gas in which a part of the atoms (or molecules) have been ionized. There are three constituents: neutral atoms or molecules (depending of the type of gas), ions and electrons. The ratio between the number of ionized particles and the neutral ones is called degree of ionization. The degree of ionization of the plasmas used for PECVD can vary in the range $10^{-6} \div 10^{-4}$.
The apparatus used is located in a professional clean room ,class 1000 and in Fig. 2.1 a scheme of the whole system is shown. It consists of two deposition chambers: the first used for Electron-Cyclotron-PECVD processing and the second for the RF-PECVD processing. The last is used for the deposition of thin films and multilayers. Each one of the two deposition chambers is separated from the load-lock chamber by a gate valve. The two chambers are always kept under vacuum pumping condition; the introduction of the substrates is achieved through the load-lock chamber with the following scheme:

1. the substrate is introduced in the load-lock chamber;
2. the load-lock chamber is pumped down to a pressure lower then 10^{-4}Torr;
3. the gate valve between the load-lock and the deposition chamber is opened;
4. the substrate is moved from the load-lock chamber to the deposition chamber by a vacuum tight transfer system;
5. the gate valve is closed.

This procedure allows to avoid the contact of the deposition chamber with the open air, reducing the risk of contamination of the grown film. The reverse procedure is used for the extraction of the grown films from the deposition chamber. The use of the load-lock system allows also the transfer of a sample from one chamber to the other without exposing the film surface to air.

The RF-PECVD reactor is a stainless steel cylinder with a diameter of 250 mm and a height of 285 mm. The chamber is provided with:

- an ionization gauge for themeasurement of the ultimate pressure before processing (which is usually in the range $10^{-8} \div 10^{-7}$Torr);
- a capacitance manometer gauge head, a throttle valve and relative automatic pressure controller for the regulation and measurement of the gas pressure during the deposition process;
- a gas manifold with mass flow controllers and associated control units, for the control of the flow of the reactive gases: SiH_4, CH_4, NH_3, CO_2 and H_2.

The substrate is introduced in the chamber by means of two stainless steel rails and is faced downwards to avoid accumulation of dust particles on the surface. The process gases are introduced by a gas diffusion ring and are evacuated by the pumping system. The pumping system consists of a turbomolecular pump and a mechanical pump in sequence. The mechanical pump has a pumping speed of 25 m^3/h and allows a minimum pressure of about 10^{-4}Torr; the turbomolecular pump has a pumping speed of 300 l/s and allows a minimum pressure of about 10^{-9}Torr. All pumps are purged by nitrogen to protect some of their most sensitive parts and to avoid possible accumulation of toxic or explosive components when reactive gases are used. The heating is performed by irradiation from a resistor located at the top part of the deposition chamber, at a distance of 20 mm from the substrate. The control of the temperature is performed by a temperature controller , which is connected to a type K thermocouple, the point of which is located in a hole in the center of the heater. The maximum temperature that can be achieved is 500°C.

2.2 Growth of amorphous silicon-based thin films

The silicon nitrides and the silicon oxycarbides were grown by means of the PECVD apparatus described before at a temperature of 493 K, using a fixed total mass flow rate of $7.4\cdot 10^{-5}$mol s^{-1}(100 sccm). The other deposition parameters:

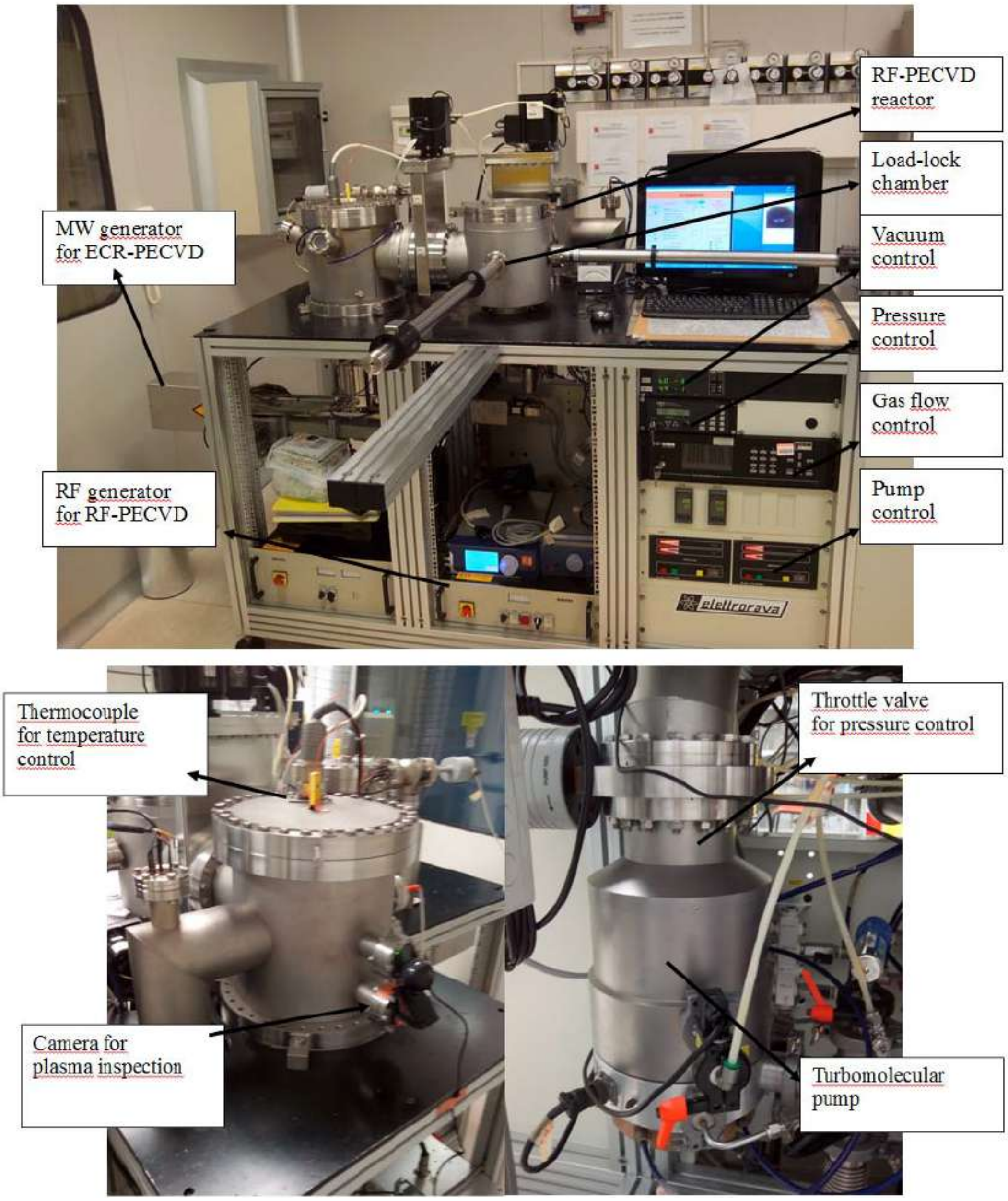

Fig. 2.1 Double-chamber growth apparatus with details concerning with the PECVD reactor.

radio frequency power density, total pressure and relative fractions of the reactive gases are reported in Table 2.1. Single layers were grown on 4 inches silicon wafers to allow optical characterization by means of UV–vis spectroscopy in reflective mode. A small area in the center of each wafer was masked to leave an uncoated region, in order to allow thickness measurements to be made. These results have been published in Mandracci et al. (2016).

VIS-NIR reflectance spectra were obtained using an Agilent Cary 5000 (Agilent California, USA) UV–visible–NIR spectrophotometer equipped with a 12.5° reflectance unit, in the 400–1000 nm range. The film thickness was estimated by means of a mechanical profilometer (Tencor P10-A) by measuring the height of the step between the uncoated region and film surface. The deposition rate of each material was then calculated, as the ratio between film thickness and deposition time, as reported in Table 2.1. The dispersion of the refractive indexes was obtained from the interferometric pattern of the reflectance spectra and the measured thickness of the amorphous silicon based thin film.

Table 2.1 Growth parameters applied for the synthesis of the a-SiN_x:H and a-SiO_xC_y:H thin-films. Uncertainties were estimated from the instrumental uncertainties given by the equipment producers.

	a-SiN_x:H (high n)	**a-SiN_x:H (low n)**	**a-SiO_xC_y:H**
Power density [mW cm^{-2}]	40±1	40±1	60±1
Total pressure [Pa]	80±1	80±1	73±1
[SiO_4]%	20±0.2	4±0.04	1±0.01
[NH_3]%	80±0.8	96±1	0
[CH_4]%	0	0	29±0.3
[CO_2]%	0	0	70±0.7
Growth rate[nm min^{-1}]	19±1	18±1	5.2±0.1

Fig. 2.2 shows that the refractive index of a-SiN_x:H grown with 96% of NH_3 in the SiH_4+NH_3 gas mixture is markedly lower than in the silicon-nitride layer grown with 80% of NH_3 (n=1.77 vs. n=2.04 at 1000 nm). This is in agreement with several other experimental findings [Giorgis et al. (1997)] and can be justified considering the higher N incorporation in the amorphous network caused by the by increase of the nitrogen precursor flux in the reactor chamber. The decrease in the refractive index for the samples obtained by increasing the ammonia fraction in the growth reactor can, in fact, be ascribed to the replacement of Si-Si bonds (in Si-rich alloys) with strong Si-N and/or Si-H bonds in the amorphous silicon

network [Robertson (1991)]. In addition, the refractive index obtained with 96% of NH_3 in the gas feedstock is typical of anamorphous silicon nitride thin film that approaches the stoichiometry (i.e. a-$SiN_{1.33}$:H). It is lower than the typical value found for stoichiometric silicon-nitride grown by means of thermal Low Pressure CVD (n~2 in the low absorption energy range), because of the hydrogenation of the PECVD alloys.

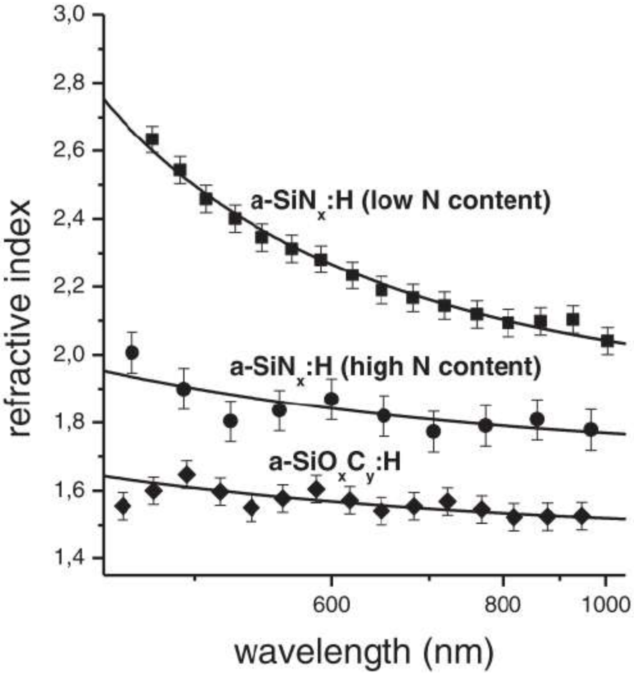

Fig. 2.2 Refractive index dispersion of a-SiN_x:H and a-SiO_xC_y:H thin films.

The refractive index is further reduced for the silicon-oxycarbide thin film, where n=1.52 at 1000 nm is measured. Such a low value is due to the excess oxygen incorporated in the SiC matrix [Miyazaki (2008)], which increases the degree of freedom for the design of dielectric multilayers with high optical contrast.

2.3 Mulitalyers based on amorphous silicon alloys

1DPC based on binary and ternary silicon-based alloys were fabricated and characterized at Politecnico di Torino. The optical features of the planar dielectric multilayers based on the discussed amorphous silicon-based alloys are presented hereafter. a-SiN_x:H and a-SiO_xC_y:H multilayers were grown on thin glass wafers of 150 μm thickness. The RF discharge was interrupted for 10 s and the deposition chamber evacuated at each hetero-interface of the stratified structures. The thickness of each layer within the stratified structures was imposed in order to take into account the deposition rate for a certain elemental composition.

A 1DPC made of all-silicon nitride alloys has been designed in order to have TE-polarized BSW sustained in the 530–650 nm wavelength region, taking into account the refractive indices measured in the homogeneous thin films. The structure consists of a 7-period stack of high (H) and low (L) refractive index silicon-nitride layers with thicknesses d_H=d_L=90 nm, terminated by a high refractive index layer with d_H=20 nm. The design has been optimized considering water as the external medium exposed to the free surface of the 1DPC. The multilayer has been deposited on a thin glass wafer and characterized by angle-resolved spectral reflectivity in the Kretschmann–Raether spectroscopic configuration. A collimated and TE-polarized white light has been used to illuminate the 1DPC through the input facet of a glass coupling prism. Reflectance maps R(θ,λ) have been obtained by means of a detection scheme in which the sample is rotated with respect to the incident beam, where θ is the angle between the normal to the 1DPC layers and the direction of the incident beam at the prism/multilayer interface. The reflected light has been detected by means of a fibered spectrometer. In order to make BSW appear, an external water medium must be in contact with the free surface of the multilayer. To this end, an appropriate fluidic cell has been employed.

The calculated TE-polarized reflectivity map R(θ,λ) is shown in Fig. 2.3 over a 560 to 650 nm spectral range. Incidence angles beyond the critical angle were considered in order to operate in Total Internal Reflection mode. A dip appears in the reflected light for specific pairs (θ,λ) ,which shows that a BSW coupling condition is reached. The reflectivity dip is dispersed in the (θ,λ) plane according to the BSW dispersion diagram [Liscidini and Sipe (2009),**?**]. An angularly-resolved spectral reflectivity map has been experimentally collected, as illustrated in the inset of Fig. 2.3(b), that shows that the BSW dispersion is in good agreement with the calculated results. The dip observed at specific angles (see, for example Fig. 2.3(c)) is related to the BSW coupling and is only observed when TE-polarized illumination is adopted.

Another 1DPC has been designed considering the high refractive index a-SiN_x:H and a-SiO_xC_y:H as building blocks. In this case, the structure consists of a 5-period stack of high-n a-SiN_x:H (H) and a-SiO_xC_y:H (L) with thicknesses of d_H=115 nm and d_L=155 nm, respectively. A lower period of the dielectric stack has

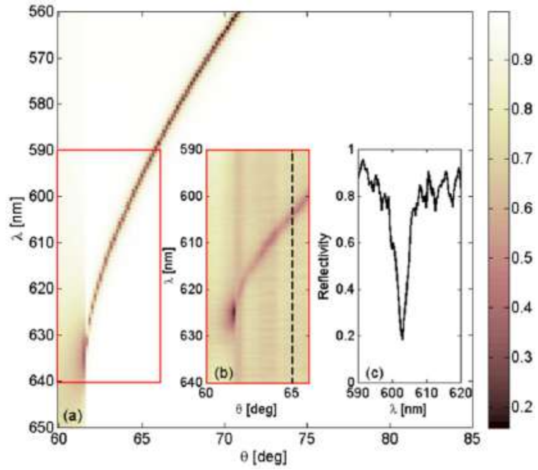

Fig. 2.3 (a) Calculated TE-polarized angularly-resolved spectral reflectivity for the all-silicon nitride 1DPC described in the text; (b) R(θ, λ) experimental reflectivity map collected in a prism-coupling configuration. The critical angle for a water/glass interface is visible at 62.5°; (c) cross-sectional spectral reflectivity profile collected at 65° (in a total internal reflection condition).

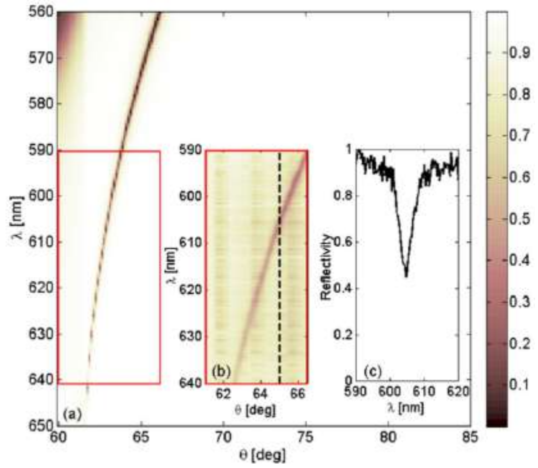

Fig. 2.4 (a) Calculated TE-polarized angularly-resolved spectral reflectivity for the silicon nitride–silicon oxycarbide 1DPC described in the text; (b) R(θ, λ) experimental reflectivity map collected in a prism-coupling configuration; (c) cross-sectional spectral reflectivity profile collected at 65° (in a total internal reflection condition).

been imposed in such a layout, taking advantage of the high optical contrast in the a-SiN$_x$:H/a-SiO$_x$C$_y$:H sequence. A clear BSW dispersion has also been pointed out in the reflectivity maps for this 1DPC, as shown in Fig. 2.4.

These results, concerning spectrally/angularly resolved reflectivity measurements, demonstrate the potentiality of amorphous silicon technology based on PECVD for refractive index tuning of high optical quality layers consisting of binary and ternary alloys (a-SiN_x:H and a-SiO_xC_y:H) to be used in 1DPC sustaining BSWs.

2.4 Plasma-Ion Assisted Vacuum Evaporation

This technique belongs to the Physical Vapour Deposition (PVD) methods that are conducted in high vacuum conditions. In Fig. 2.5, a schematic drawing of the PIAD principle is shown. Material from a thermal vaporization source reaches the substrate with title or no collision with gas molecules in the space between the source and substrate. The trajectory of the vaporized material is *line-of-sight*. The vacuum environment also provides the ability to reduce gaseous contamination in the deposition system to a low level. Typically, vacuum deposition takes place in the gas pressure range of 10^{-9} to 10^{-5}mbar depending on the level of gaseous contamination that can be tolerated in the deposition system. The thermal vaporization rate can be very high compared to other vaporization methods. The material vaporized from the source has a composition which is in proportion to the relative vapor pressure of the material in the molten source material. Thermal evaporation is generally done using thermally heated sources such as tungsten wire coils or by high energy electron beam heating of the source material itself. Generally the substrates are mounted at an appreciable distance away from the vaporization source to reduce radiant heating of the substrate by the vaporization source. For the PIAD technology (as shown in the schematic drawing in Fig. 2.5), a plasma ion source is installed in the center of the chamber. The high energetic ions that are emitted from the source and that are accelerated towards the substrate holder allow to densify the growing layer very effectively without heating of the substrates.

The plasma ion source which represents the core element of a PIAD plant is based on a LaB_6 cathode, a cylindrical anode tube and a solenoid magnet as can be seen in Fig. 2.6. The cylindrical LaB_6 cathode is indirectly heated by a graphite filament heater. A dc voltage between anode and cathode creates a glow discharge plasma with a hot electron emitter, supplied with a noble gas such as argon. Due to the magnetic field of the solenoid magnet, which surrounds the anode tube, the plasma is extracted towards the direction of the substrate holder. The reactive gases are introduced through a ring shower located on top of the anode tube. Because of the high plasma density, the reactive gases get activated

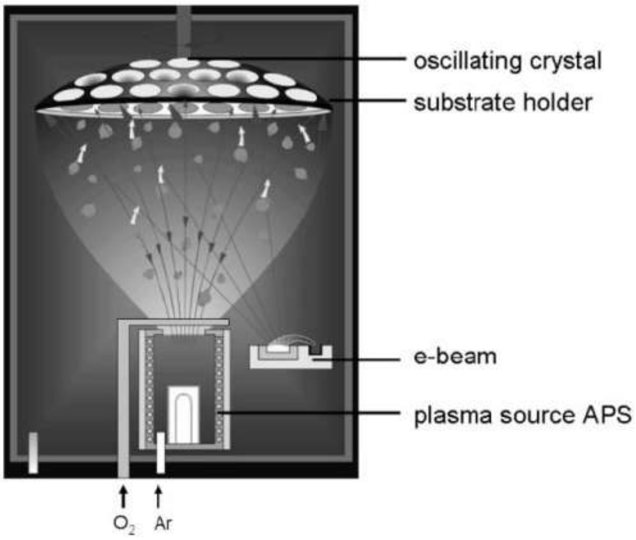

Fig. 2.5 Schematic drawing of PIAD deposition technique.

and partly ionized. Ionization of the reactive gas lowers the required reactive gas pressure, to grow stoichiometric films. The plasma source is electrically insulated with respect to the chamber ground. Therefore the plasma gets a positive self bias voltage relative to the chamber walls and to the substrate holder. The ion energy is mainly determined by the self bias voltage between anode and chamber ground. The magnitude of the bias voltage, which is controlled during the evaporation process, depends on the applied discharge voltage, the magnetic field strength, the gas flows and the chamber pressure. Due to momentum transfer of the accelerated plasma ions onto the condensing film molecules, the surface mobility and therefore the packing density of the growing film is increased. Since the plasma spreads in the total volume between the plasma source and the substrate holder, the evaporant also becomes partly ionized.

All the photonic crystals used in this work have been produced at the Fraunhofer Institute Jena (IOF) by means of an APS 904 PIAD system (Leybold Optics GmbH). Fig. 2.7 shows the inside of the APS 904 if the chamber door is open. On the top the rotatable substrate holder is mounted. The substrate rotation is necessary to provide good thickness homogeneity in circumferential direction. The homogeneity in radial direction is given by an adapted shadow mask. Two 270 ° electron beam gun evaporators are installed where it is possible to evaporate almost every material with a high deposition rate. Nowadays these evaporators are standard equipment for this kind of coating plants and are usually applied

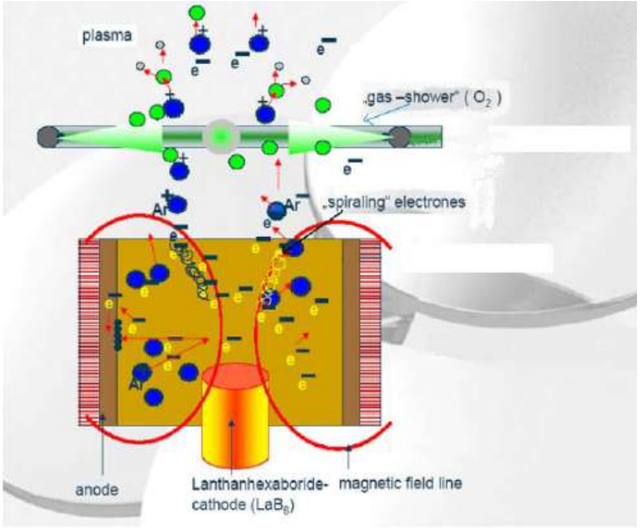

Fig. 2.6 Schematic drawing of the plasma ion source.

for the evaporation of metal oxide materials. In the center of the chamber the Advanced Plasma Source (APS) is situated.

2.5 Re-engineering of thin film optical properties by means of BSW

The fabrication of suitable 1DPC showing proper BSW dispersion and field enhancement is a critical requirement for highly sensitive biosensing. An intimate knowledge of the optical constants of the deposited materials is essential for thin film staks and high quality optical coatings. Relevant quantities are the absolute value and the reproducibility of the refractive index n, the loss coefficient k and layers' thicknesses of the 1DPC. The excitation of leaky modes, like BSW, using Kretschmann-Raether attenuated total reflection (ATR) configuration can be be used for the determination of thin film parameters. The goniometer set-up for the measurement of the angularly resolved reflectance comprising a fused silica half-ball lens which allows large observation angles is shown in Fig. 2.8. The device under test consist of 1 mm thick SiO_2 substrate with a respective BSW stack. This substrate is attached to the half ball lens (which is in fact slightly modified i.e. reduced in thickness by the thickness of the substrate) by means of an appropriate index matching liquid.

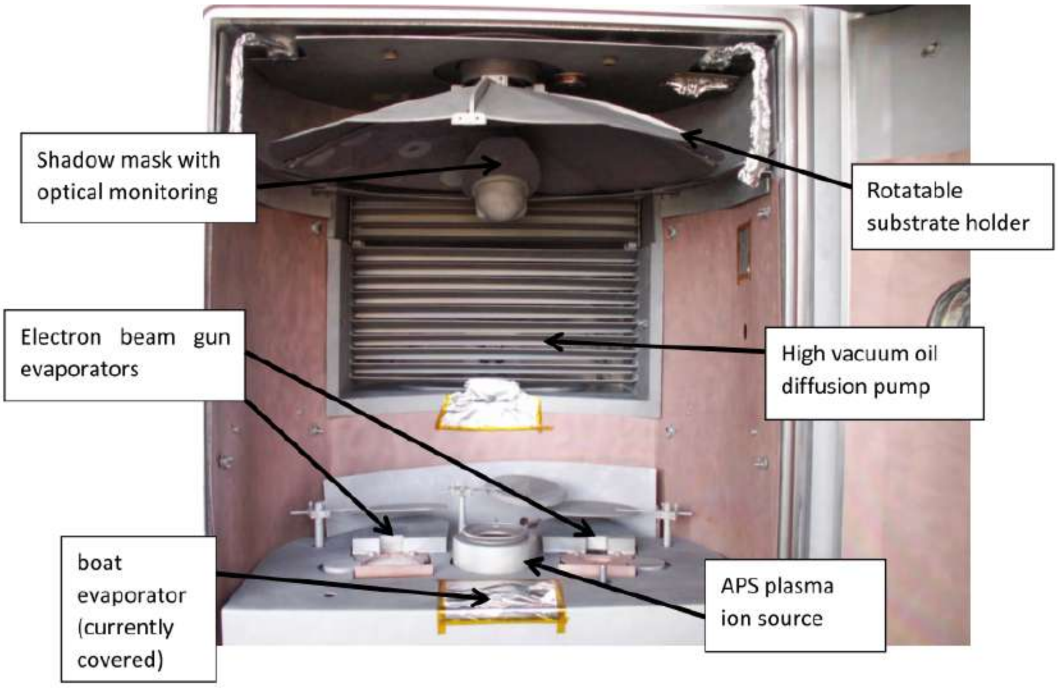

Fig. 2.7 View inside the open APS 904 deposition chamber.

The angularly resolved signal which is recorded in TE as well as TM polarization is detected by an integrating sphere and both a reference and the reflectance signals are processed with a lock-in-technique, which greatly reduces any external signal noise. Due to the structural dimensions of the components the angular span ranges from 10° to 80° in the employed two-θ measurement setup. The results presented here have been published in Wächter et al. (2016).

Having in mind radiation losses of some 10^{-6} for SiO_2 and $10^{-4} \div 10^{-5}$ for H-layers of TiO_2 and Ta_2O_5, respectively, a BSW stack for an operating wavelength of λ=660 nm have been designed. The corresponding stacks are fabricated onto 1 mm thick substrates of fused silica by means of PIAD technology. Special care has to be taken in the reflectance measurement to record data with an appropriate angular resolution. Whereas for the angle scan well below TIR a step width of $\Delta\theta$=0.1° is sufficient, the resonance dip requires a much finer resolution of 0.01° or even below. Furthermore, narrow features of the measured reflectance curve are prone to be affected by a finite angular bandwidth of the beam. Thus, this angular bandwidth is determined separately by a reflectance measurement around the TIR-edge at a bare substrate, Fig. 2.9.

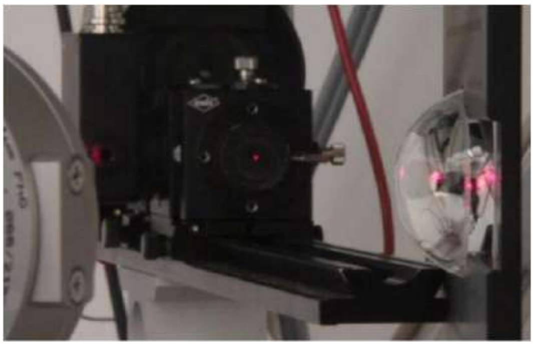

Fig. 2.8 Goniometer set-up comprising half ball lens coupling for large observation angles.

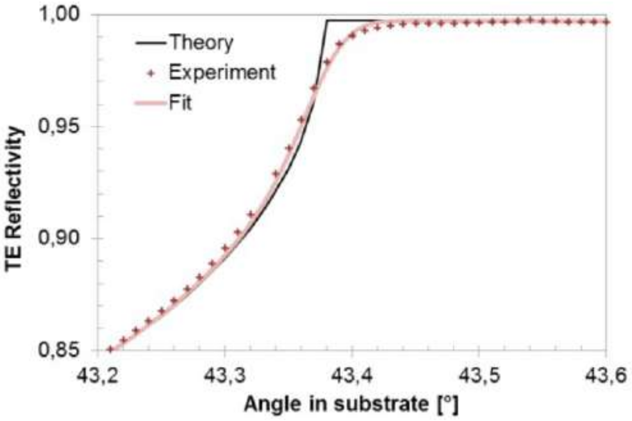

Fig. 2.9 TE-reflectivity of bare SiO_2 substrate close to the TIR-angle, measurement (dots), simulated values (black), fitted values with Gaussian angular beam width included in simulation (red).

Assuming a Gaussian shape of the angular spectrum the corresponding angular beam-width $\Delta\theta_{beam}$ results in a corresponding distribution of plane wave components. If the fit of measured reflectance data and those modeled by TMM comprises a corresponding convolution $\Delta\theta_{beam}$ is a parameter which can be readily determined. For the underlying setup a typical value of $\Delta\theta_{beam}$=0.035° or 0.6 mrad can be derived from the data shown in Fig. 2.9 which is taken into account within the fits to determine the parameter of the layer stacks, subsequently.

Two HL-stacks sub$|(LH)^4|$ L of TiO_2 and SiO_2 with nominal values of d_L=220nm and two different values of d_H, i.e. 115nm and 275nm, respectively, are examined. Intentionally, the particular angular resonance positions are similar, but the power-fraction in the H and L-layers differs. Thus, even with a single dip in both reflectance curves a determination of both k_L and k_H is possible. Since neither designated optical constants nor film thicknesses are perfectly met in a deposition the fit of the reflectance data must provide the complete layer data vector LDV, whose components in Matlab notation reads as LDV(i,1:3) = [n_i, k_i, d_i] for any of the individual layers. Thus, with a layer number of N_l the total numbers of unknowns to be determined in a fit would be 3 $N_l + 2$ if angular beam width and n_{sub} would be cross-checked, too. With some reasonable assumptions the number of unknowns can be reduced, i.e. assuming identical n and k for the respective layer-types, and omitting a cross-check of $\Delta\theta_{beam}$ then 9 thickness-values, three refractive indices and two k values need to be fixed in this specific configuration. The numerical fit problem can be tackled by any optimization code, ranging from downhill-simplex to Levenberg-Marquardt for nonlinear least squares, at least in principle. For any fit a reasonable guess for the start LDV has to be provided, self-evidently, where at least for the fit up to the TIR-edge the design LDV might work. A direct fit of the complete reflectance measurement in just one attempt turns out to be all but impossible. Generally, for any practical fit including the resonance dip reasonable strict parameter constraints are needed in order to prevent the optimization algorithm from digressive runaway of some of the stack-parameter values.

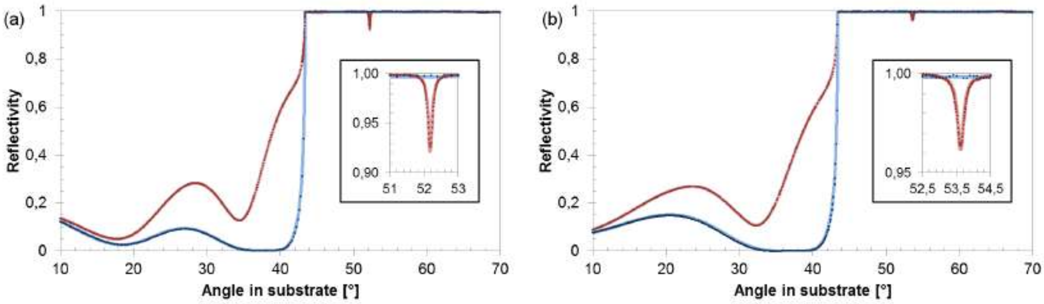

Fig. 2.10 Fitted TE (red) and TM (blue) reflectivity curves for BSW-stack with d_H ~275nm (a) and 115 nm (b). Measured values are indicated by dots, fits are plotted as lines.

The resulting fit for the TiO$_2$-based BSW with the thick H-layers is shown in Fig. 2.10. The LDVs for both H-thicknesses are given in Table 2.2. The differentiation of the L and H losses relies on a combined analysis of both samples.

The validity of the calculated refractive indices n and layer thicknesses has been confirmed by variable angle spectroscopic ellipsometer measurements. The losses measured for the BSW-stacks are seemingly reliable, at least concerning the order of magnitude. However, measurements of similar layers by e.g. laser calorimetry show perceptibly lower losses as those estimated by the evaluation

Table 2.2 Fitted LDVs of both TiO_2-BSW-stacks.

	Stack with thick H-layer **Thickness nm**	**Stack with thin H-layer** **Thickness nm**	n	k
L^4	215.1	211.6	1.446	$6{\cdot}10^{-6}$
H^4	274.8	115.8	2.26	$5.5{\cdot}10^{-5}$
L^3	220.1	218.9	1.446	$6{\cdot}10^{-6}$
H^3	276.9	117.9	2.26	$5.5{\cdot}10^{-5}$
L^2	219.6	218.7	1.446	$6{\cdot}10^{-6}$
H^2	274	112.1	2.26	$5.5{\cdot}10^{-5}$
L^1	215.5	214	1.446	$6{\cdot}10^{-6}$
H^1	276.4	115.7	2.26	$5.5{\cdot}10^{-5}$
L^0	215.6	214.3	1.446	$6{\cdot}10^{-6}$
Sub			1.457	

of the leaky wave resonances. This can be attributed to the longer wavelength of λ=1030nm used for laser calorimetry, at least partly. Furthermore, this tendency is comprehensible simply due to the fact that with respect to leaky wave propagation material losses and losses due to surface roughness add up, and, from the point of view of critical coupling requirements act as the counterbalance of the inherent radiation loss of the leaky wave stack. In addition to the stack-air surface internal interfaces contribute as well to the scattering particularly due to local field maxima at L-H interfaces of reflector-layer-pairs. Despite this, the procedure presented is a great help in the determination of the LVD of a thin film stack. This was used to fine tune the PIAD depositions and produce 1DPC showing proper BSW dispersion and field enhancement.

2.6 Selection of the 1DPC

Once the deposited layers were characterized, the optimization procedure illustrated in the previous chapter was used to design the optimized 1DPC used for the experimental section. A new stack was designed that contained TiO_2 as thin, high index layer in order to increase resonance width. In fact, although a decrease of resonance width is required in order to achieve a decreased LoD, imaging such extremely narrow angular resonances increases the demand of resolution for any optical system. Resolution means the capability to obtain an image of this resonance in order to achieve sampling by the pixelated detector. Resolution limits are imposed due to diffraction limits an aberrations by non-ideal optical elements. This design represents a trade off between the the smallest LoD possible and the possibility to correctly image the label-free resonance. Different extinction of TiO_2 can be prepared during deposition thus resulting in:

- *low loss* TiO_2 n$_{(TiO_2)}$ ~2.28+i5.0·10^{-4}
- *high loss* TiO_2 n$_{(TiO_2)}$ ~2.28+i1.8·10^{-3}

Wavelength of calculation is 670 nm and the values n$_{(Ta_2O_5)}$= 2.108+ i 5·10^{-5}; n$_{(SiO_2)}$= 1.474+ i 5·10^{-6}; n$_{(subs)}$=1.5299 have been assumed for simulation.
After preliminary steps the structure subs | SiO_2 | $(Ta_2O_5/SiO_2)^{2or3}$ | TiO_2 | SiO_2 | water has been selected for detailed consideration and optimization as described below. In case of low TiO_2 losses a 3 period stack and in case of high TiO_2 losses a 2 period stack is being used in order to achieve deep resonances. Both top layers have been set to 20 nm thicknesses in order to achieve a proper wave guiding layer. Furthermore, a 20 nm SiO_2 cover layer is introduced to enable for silane based surface chemistry.
It turns out, that both the angular position of the resonance and the sensitivity are not affected by the losses of the TiO_2 layer. This is due to the fact that both quantities depend on the refractive index real part much more that on the losses in such loss range. Contrarily and as has been intended, the resonance width and depth vary when changing the TiO_2 layer losses and adapting the substrate side stack. This is apparent when comparing the right and left columns in Fig. 2.11. From such data the performance measures FoM and LoD have been derived (Fig. 2.12).

In result, using a high loss stack with thin TiO_2 high index layer theoretically enables one to achieve LoD_{min}<10 nm or a FoM_{max} ~0.4 nm^{-1}.

The selected multilayer has a maximum sensitivity and comprises *high loss* TiO_2 top layer and two period stack with 120 nm thick Ta_2O_5 and 275 nm thick SiO_2. The following properties can be derived for the selected stack:

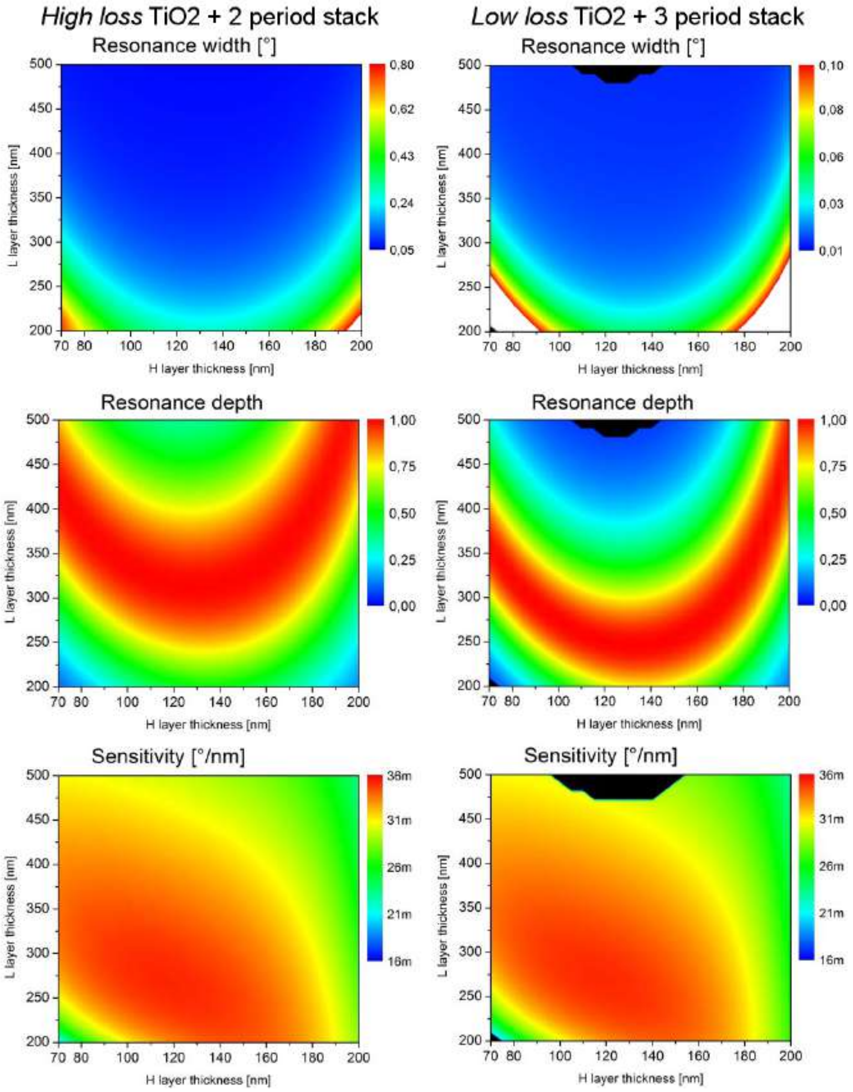

Fig. 2.11 Comparison of resonance widths, depths as well as angular position and sensitivity for the cases of high and low absorbing TiO_2 layer as described in the text. Black color depicts regions with invalid data due to the limited range of angular calculation.

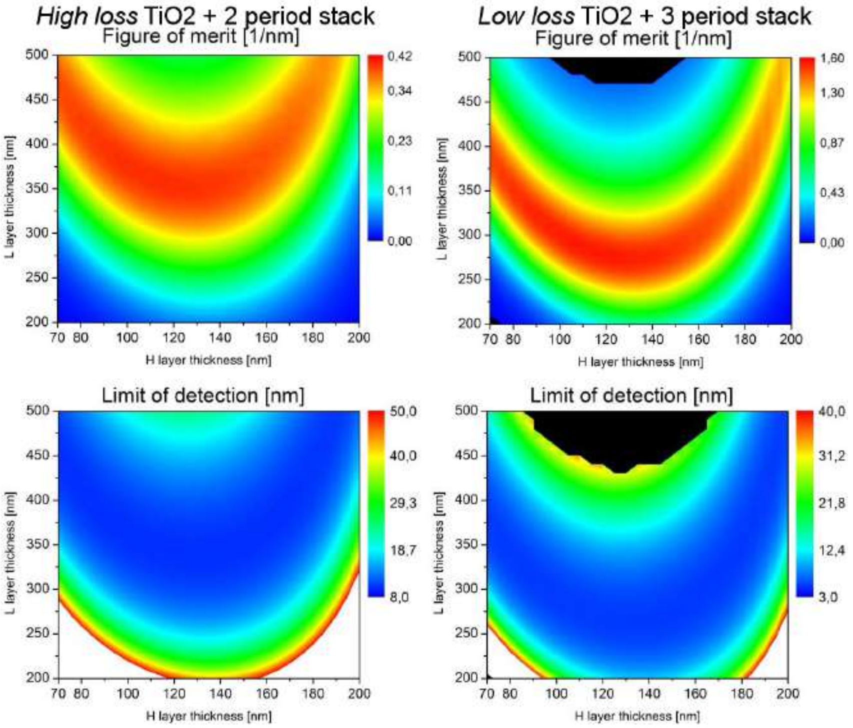

Fig. 2.12 Comparison of resulting LoD and FoM for the cases of high and low absorbing TiO_2 layer as described in the text. Black colour depicts regions with invalid data due to the limited range of angular calculation.

Depth	D = 0.92
Width of Resonance	W = 0.12°
Sensitivity	S = 0.034°/nm
Angular range	A = 1.36° (label-free)
Figure of Merit	FoM = 0.26 nm^{-1}
Limit of detection	LoD = 12.9 nm

Fig. 2.13(a) presents a rendering of a section of the chosen 1DPC stack (not to scale).

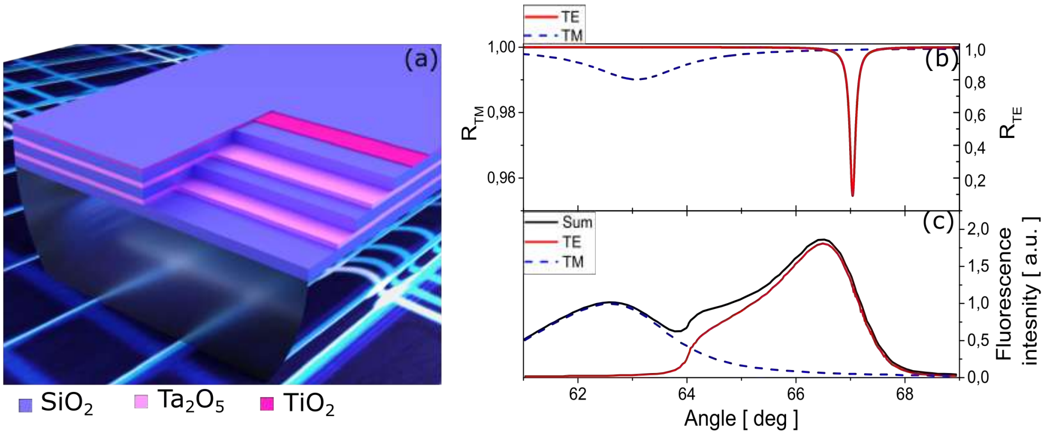

Fig. 2.13 (a) Rendered image of a cross section of the 1DPC on top of the biochip (not to scale). The 1DPC image is sectioned to show the different layers. (b) Calculated angular reflectivity profile for TE and TM polarized light at λ= 670 nm, (c) simulated intensity distribution of the fluorophore DyLight 650 over an 8 ° angular range for TE, TM, and SUM emission polarization.

In Fig. 2.13(b) it is shown the calculated angular reflectance spectrum for TE and TM polarized incident light at λ= 670 nm for the chosen 1DPC. The external medium used in the calculation is water, n$_{H_2O}$= 1.33. BSW is excited trough an electromagnetic wave at λ around 67 ° when considering the TE polarized mode and 63 ° for the TM, the configuration used is Kretschmann-Raether. As already mentioned, the excitation of BSW leads to an enhancement of the electric field at the interface between the 1DPC surface and the external medium. This enhancement is used to excite fluorophores at the stack surface and boost their emission into the direction of the substrate. The resulting fluorescence emission is angularly dispersed due to the dispersion of the BSW thin film stack as shown in Fig. 2.13(c). It presents the simulated intensity distribution of an ensemble of fluorophores with a given spectrum over an 8 ° angular range. Two peaks are clearly visible, they are due to the coupling of the fluorescence emission to the BSW TE mode and to the TM mode present in the 1DPC structure.

2.7 Optical setup for biosensing

The optical system have been developed by the Fraunhofer Institute for Applied Optics and Precision Engineering IOF in Jena and is depicted in Fig. 2.15. The author of this thesis have participated to the development of the system during a period prior to the beginning of the Ph.D.
The biosensing platform is furnished with a disposable and low cost sensor unit: a molded plastic (TOPAS®) substrate with micro-optics (KDS Raderberger Gmb.H, Germany) (Fig. 2.14) represented as a prism in Fig. 2.15. The chip links the optical system with the fluidic (handling) system and is the solid support for the dielectric thin film stacks as transducer.

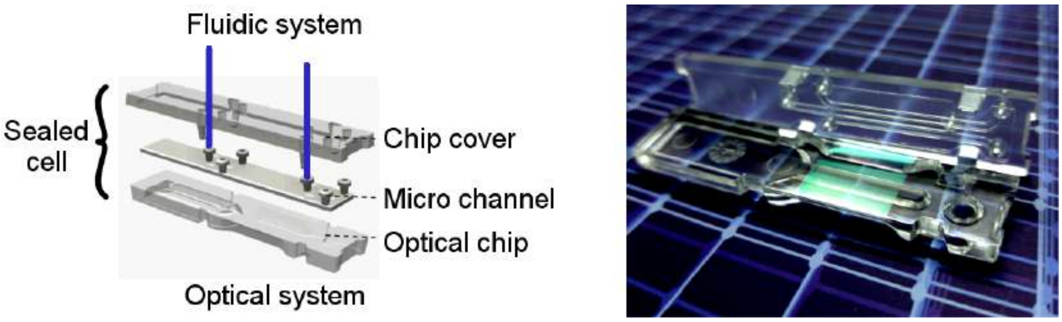

Fig. 2.14 Sketch of the chip functionality (left), photo of the TOPAS® chip with its polymeric microfluidic cover, the greenish part is the 1DPC.

A collimated, TE polarized beam of a 670 nm laser diode is focused by a cylindrical lens (CL1) into the polymer chip, thus illuminating a line at the sensor surface. The reflected light is angularly imaged onto the CCD image sensor (APOGEE Ascent with Sony ICX814) by the cylindrical lens CL2. Therefore, each row of the CCD image can be assigned to one angular component of the reflected light in order to measure the angular reflectivity curve plotted in Fig. 2.13(b). In result, an angular range of 2.9 deg is analyzed along the long dimension of the CCD. For the label-free operation, the angular range was restricted around the resonance to reduce the memory occupation and increase the CCD frame rate.

More than 20 spots can be arranged along the illuminated line at the sensor surface. These are imaged by a cylindrical optical system (CL3 and CL4) onto the

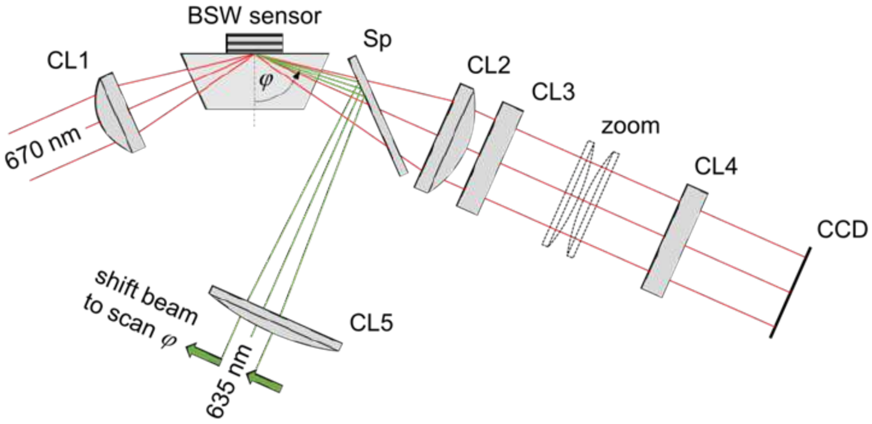

Fig. 2.15 Sketch illustrating the optical system without plotting laser diode collimation systems. Label-free and fluorescence emission is shown in red while fluorescence excitation is illustrated in green. See text for details.

columns of the CCD in order to allow one for analyzing each spot independently. The fluorescence detection is achieved by means of a 635 nm laser diode. The resonance for fluorescence excitation is as narrow as the resonance utilized for label-free sensing. Its angular position will also shift during the experiments when molecules bind onto the sensor surface (the same effect as the one exploited for label-free sensing). That's why the angle of fluorescence excitation needs to be scanned in order to find the correct excitation angle to exploit surface wave enhanced fluorescence excitation. Here, the collimated beam of the 635 nm laser diode is focused by a 100 mm focal length cylindrical lens into the sensor (green rays in Fig. 2.15) thus illuminating the same line as the one illuminated in the label-free mode. The dichroic splitter SP combines the different wavelengths. Laterally shifting the collimated laser beam keeps the illuminated position constant but changes the angle of excitation.

The dichroic splitter SP transmits the emitted fluorescence that is imaged angularly and laterally by the same optical system onto the same detector as in the label-free case. But the angular range of 2.9 deg observed in the label-free case is insufficient to collect all fluorescence energy emitted. Therefore a cylindrical system (*zoom* in Fig. 2.15) can be introduced. This will increase the angular range observed, thus enabling to collect almost all fluorescence, but reduce the angular resolution which is not required in the fluorescence mode.

Chapter 3

Biofunctionalization protocols and materials

Successful detection of target biomolecule upon the 1DPC surface relies on the selective interaction of the biosensor with the target biomolecule. It is therefore essential to immobilize a specific antibody for the target biomarker on the 1DPC biochip surface. A direct assay was chosen (Fig. 3.1) for the biomarkers detection and to assess the performance of the biosensor. A direct assay allows the sensing of the analytes both in the label-free mode as well as fluorescence, as depicted in Fig. 3.1. The assay involves a two-step method for achieving the dual mode of detection. In the label-free mode, the biomarkers are directly immobilized on the antibody-functionalized surface and physical measurements are performed. However, a second specific primary antibody is bound on the biomarker-immobilized surface in the second mode of detection. Using a second primary antibody labelled with fluorophores, the detection can be performed in fluorescence mode.

To achieve such a versatile approach for detection, the surface should be properly functionalized prior to the covalently attach of the primary antibody. The activity of proteins immobilized on a solid surface, is typically weaker than that in the aqueous phase, mainly because the orientation of the protein molecules on a solid substrate is random. The strategy adopted involves conjugating the chemically functionalized surfaces with protein G that should properly orient the probe antibodies to achieve higher sensitivity. This protein is capable of binding the Fc fragment of the antibody, leaving free the Fab fragment where the interaction with the antigen takes place. Next, the protein G modified surfaces

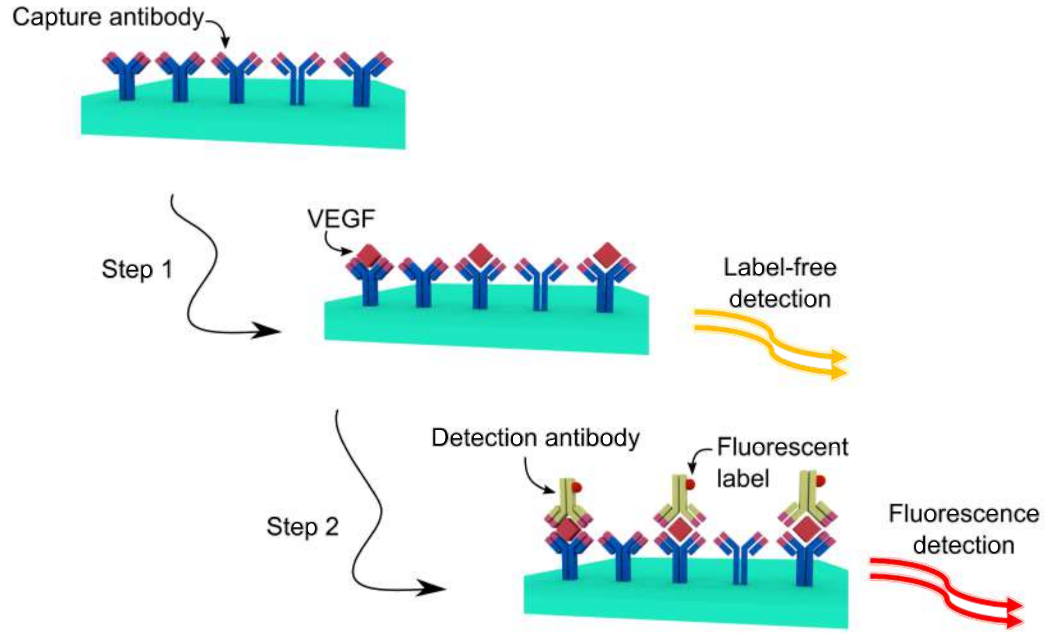

Fig. 3.1 Schematic representation of the direct immunodetection assay. The biochips are first functionalized with protein G, followed by conjugation with primary antibodies (capture antibodies). These antibodies specifically interact and capture the biomarkers, which can be detected using label-free mode (Step 1). Subsequently, second primary antibodies (detection antibodies) tagged with fluorophores are added, which specifically recognize the bound biomarkers and can be detected in the fluorescence mode (Step 2).

will be covered with a densely distributed properly oriented probe antibodies, specific for a given biomarker. Although the use of protein G seemed reasonable in first tests, the measurements carried out on the final platform suffered from non-specific absorption due to non-uniform cover of this molecule. As will be shown later, the use of protein G was discontinued in order to work out the issue of the non-specific absorption.

The surface functionalization protocol was optimized in close collaboration with the group of Prof. Molly Stevens at the Imperial College, London.

3.1 APTES wet functionalization

A protein biosensor on solid surfaces must have an artificial biomolecular monolayer. These thin organic films increase the biocompatibility of the surface and protect the proteins form denaturation and structural modification during surface immobilization. Therefore, it is mandatory to design possible biomolecule adsorption strategies that could be adapted to the studied 1DPC system. The designed 1DPC has a silicon dioxide (SiO_2) active layer for protein immobilization. Among the various surface modification techniques, the deposition of a self-assembled monolayer (SAM) of organosilane on a SiO_2 surface is very versatile, and has many advantages over other approaches. Many organosilanes have been employed to form SAMs on such surfaces [Mittal and International Symposium on Silanes and Other Coupling Agents. (1992)].

(3-aminopropyl)triethoxysilane (APTES) chemistry is particularly appealing for antibody immobilization, due in part to many advances in the understanding of this class of surface modification agents. APTES can readily react with hydroxyl groups and can support the formation of monolayer coverage under carefully controlled conditions [Mittal and International Symposium on Silanes and Other Coupling Agents. (1992)]. Modification of the surfaces through APTES chemistry results in amino functional group that can be readily conjugated to chemical agent that would lead to crosslinking with the protein of interest (Fig. 3.2).

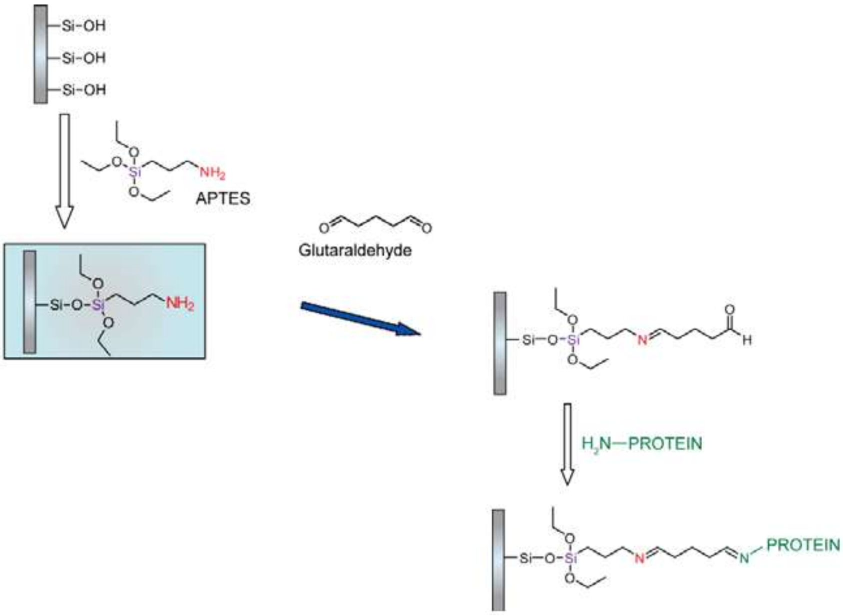

Fig. 3.2 Wet functionalization of test substrates with (3-aminopropyl)triethoxysilane. The amine termination of the functionalized surface enables cross-coupling with protein through glutaraldehyde.

Glutaraldehyde (GAH) is used as a bifunctional agent to couple the APTES-functionalized surface with protein G, where a terminal aldehyde group would be free to react with the antibody (Fig. 3.2). Using glutaraldehyde as a crosslinking agent a dense monolayer of proteins is obtained on the surface irrespective of different reaction mechanisms.

For the silanization, the substrates were cleaned in piranha solution for 10 min at room temperature, thoroughly rinsed with de-ionized water, and then dried under N_2 gas. Initially, the substrates were incubated with 2, 5 and 10% (v/v) APTES solution in 95% ethanol-water mixture for 1 hr at room temperature. Reaction efficiency at different reaction time such as 30 min, 1 hr and 2 hr was also studied. Following the APTES reaction the slides were sonicated for 2 min and rinsed with ethanol and water to remove non-covalently adsorbed silane compounds. After thorough washing the chips were cured at 80 °C for 1 hr on a hotplate to prepare a stable monolayer of APTES ligand. Static contact angle measurements were performed in three replicates using 5 μL of water and using the Laplace-Young fitting method.

As observed from the static water contact angle (WCA), the substrates were very hydrophilic with a measured WCA of ~10 °. The surface hydrophobicity increased significantly for the APTES SAMs with WCA ranging between 51 ° and 58 °. Interestingly, the WCA was higher for the lower amount of APTES, indicating an enhanced surface hydrophobicity for lower amount of APTES. This observation may point at the well-defined SAM formation on the substrates at lower concentration of APTES. However, the reaction with 2% APTES at the chosen time points (30 min, 1 hr, and 2 hr) did not alter the surface hydrophobicity significantly (Fig. 3.3(A, J, K)), suggesting that the surface was covered with the SAM even within a shorter reaction time. The APTES reaction, therefore, presents an efficient strategy for functionalizing the 1DPC surface.

The APTES layer was immobilized with fluorescein isothiocyanate (FITC) to ensure that the APTES treatment of the substrate surface provided sufficient free amino groups that would enable conjugating with a crosslinker in the next step of functionalization. FITC is an aminereactive fluorescent compound that forms a stable covalently attached fluorescent conjugate (FITC-APTES conjugate) after reacting with APTES, containing a primary amine group [Jang and Liu (2009)]. FITC conjugation was performed on the APTES-functionalized surfaces by incubating with 0.1 mg/ml FITC in DMSO for 12 h. Then, the samples were washed

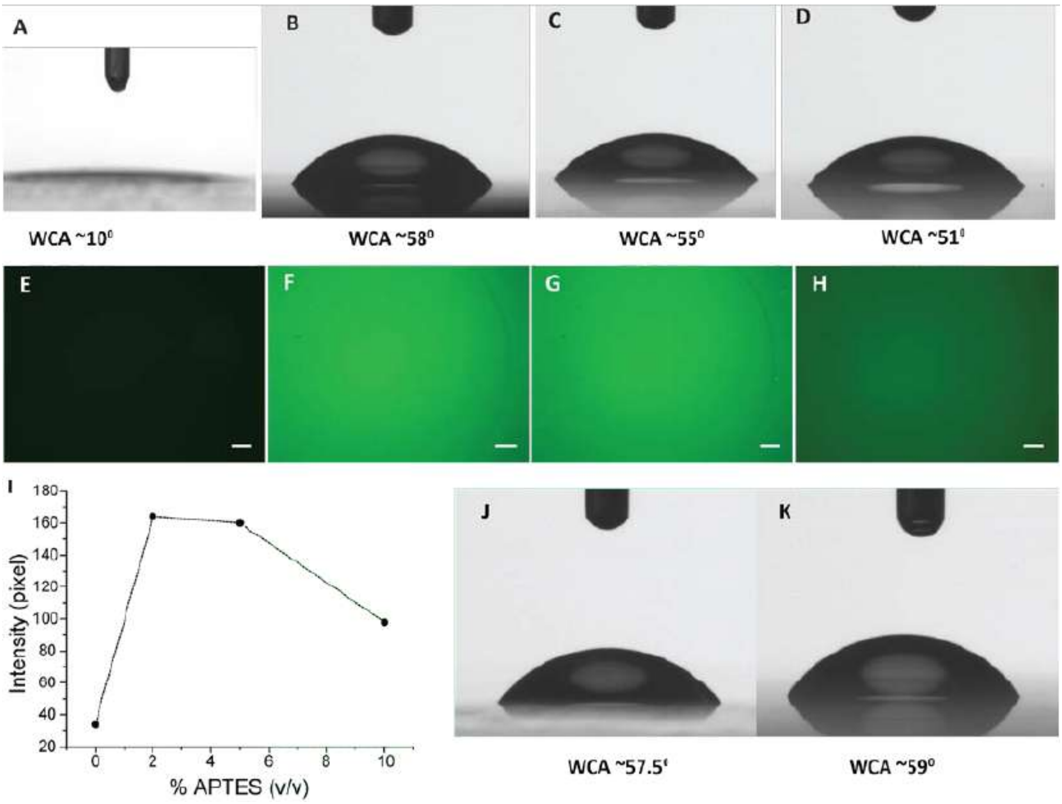

Fig. 3.3 APTES functionalization of test substrate with SiO_2 outermost layer. Static contact angle of water were measured on surfaces functionalized with (A) 0%, (B) 2%, (C) 5%, and (D) 10% APTES (v/v). Fluorescent images of APTES-FITC were captured for slides treated (E) without APTES and with different amount of APTES such as (F) 2%, (G) 5%, and (c) 10% for 1 hr at room temperature. (I) Fluorescence intensities of each of the images were plotted against the amount of APTES reacted. Contact angle was measured for the surfaces treated with 2% APTES for (J) 30 min, and (K) 2 hr at room temperature. Scale bar: 1 μm.

with DMSO and ethanol inan ultrasonic bath and blown dry using nitrogen. Fluorescent images (using a microscope) of the FITC-APTES conjugates presented an interesting trend. While both the 2% and 5% APTES provided highly fluorescent surfaces, the reaction with 10% APTES resulted in a surface with FITC labelling to a lesser extent (Fig. 3.3(E, F, G, H)). The fluorescence intensity of the different functionalized surfaces showed a linear decrease (Fig. 3.3I). Based on these observations, 2% and 5% APTES concentrations were chosen.

3.2 Conjugation with glutaraldehyde

Following the APTES functionalization, the glutaraldehyde (GAH) crosslinking reaction was studied. The optimization was carried out using a 2:1 APTES:GAH ratio on the substrates pre-functionalized with 2% and 5% APTES. Also, the reaction efficiency was assessed in presence and absence of sodium cyanoborohydride ($NaCNBH_3$), a mild reducing agent that reduces the unstable imine bond formed between the primary amino group of APTES and the aldehyde group of glutaraldehyde. The resulting secondary amine compound should provide a stable monolayer of the crosslinker conjugated to the surface. So, the 2% and 5% APTES-functionalized slides were immersed in GAH solution in 100 mM $KHCO_3$ (pH~8.5) in presence or absence of 0.1 mM $NaCNBH_3$ for 1 hr. Then, the slides were sonicated for 2 min to remove non-covalently adsorbed GAH molecules and washed thoroughly with water. It can be observed that $NaCNBH_3$ plays a major role in the conjugation reaction.

It can be seen that while the static WCA slightly increased to ~61 ° indicating enhanced surface hydrophobicity upon GAH conjugation, the WCA values were very similar for both the 2% and 5% APTES-functionalized surfaces in absence of the reducing agent (Fig. 3.4). However, the GAH reaction in presence of $NaCNBH_3$ provided much higher hydrophobicity for both the surfaces (Fig. 3.4E), indicating that the GAH functionalization on APTES-coated surfaces is more effective in presence of the mild reducing agent. The hydrophobicity of the 2% APTES-functionalized surface was very high compared to the 5% APTES-coated slide, suggesting an efficient reaction with the crosslinker on the well-defined APTES layer.

3.3 Final functionalization protocol and definition of spot arrays

Four biochips were functionalized at a time. All the concentrations, volumes and times of the functionalization and immobilization procedure were adjusted to obtain the best sensor performance. 1DPC surface was cleaned with piranha (H_2SO_4:H_2O_2 = 3:1) for 10 minutes, washed thoroughly using de-ionized (DI) water and ethanol and dried with N_2. The cleaned biochips were dipped in a 2% (v/v) solution of APTES in a mixture of ethanol/water (95:5 v/v) for 1 hour.

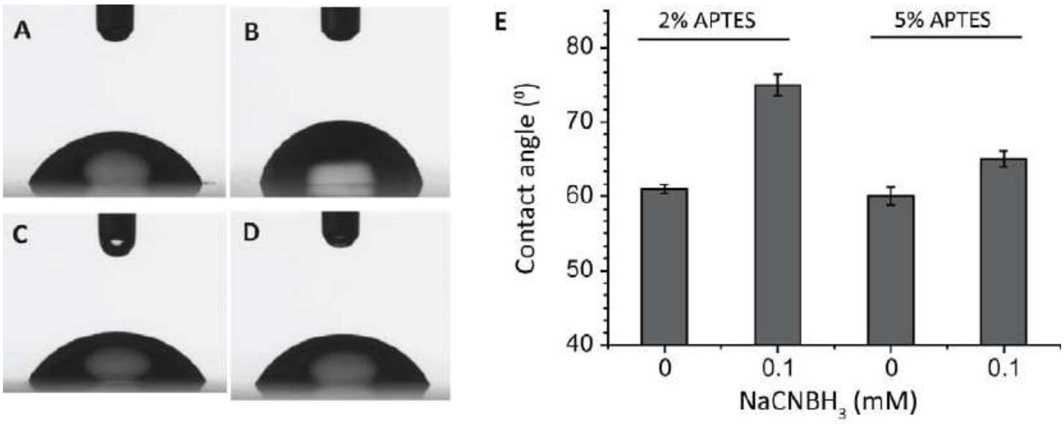

Fig. 3.4 Glutaraldehyde conjugation of APTES-functionalized surfaces. Static contact angle of water were measured on GAH conjugated 2% APTES-functionalized surfaces with (A) 0, (B) 0.1 mM NaCNBH$_3$ and on 5% APTES with (C) 0, (D) 0.1 mM NaCNBH$_3$.

They were then transferred in pure ethanol and sonicated three times. After rinsing with pure ethanol and drying with N_2 the biochips were baked on a hot plate at 80 °C for 1 hour. As already mentioned, glutaraldehyde (GAH) was used as a homobifunctional agent to couple the APTES functionalized surface with the specific antibodies that are intended to be immobilized on the surface. The prepared biochips were dipped in a solution of 1% (v/v) GAH in 100 mM sodium bicarbonate buffer (pH 8.5) in the presence of 0.1 mM NaCNBH$_3$ for 1 hour. A last sonication was performed in DI water followed by a thorough wash with DI water.

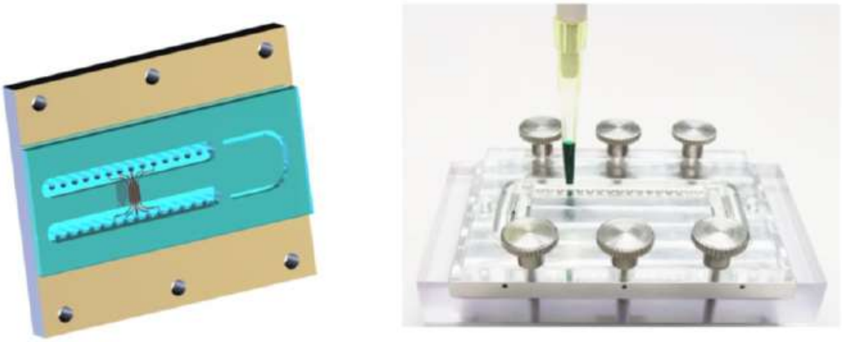

Fig. 3.5 Picture illustrating the five channel functionalization flow cell. The Polydimethylsiloxane (PDMS) flow cell (blue) with the five fluidic channels (red) attached to an aluminum plate (left). Filling of a channel flow cell using a standard microliter pipette (right).

The following step was the protein G immobilization that was carried out after mounting on the functionalized biochip the spotting tool showed in Fig. 3.5. Such a microfluidic tool allowed to prepare five different measurement spots on the sensor surface. The tool is composed of a Polydimethylsiloxane (PDMS) flow cell with five parallel channels (each 200 μm wide and 200 μm high) that is attached to an aluminum backplate. For the immobilization of the biomolecules, the biochip was loaded into a socket plate and topped with the five channel functionalization flow cell, which was then locked using screws. Thus, a closed fluidic system on the chip is obtained which allowed filling the proteins to be immobilized using a standard microliter pipette into the channels (Fig. 3.5, right). The cell was used to immobilize in two regions (channels) of the biochip surface BSA (10 mg/mL) and in three regions protein G (0.5 mg/mL). After 1 hour of incubation the biochip was detached from the tool and rinsed with D-PBS. The biochip was loaded again in the tool and the same three channels used for PtG were then filled with a solution containing the capture antibody, specific for the biomarker to be detected during the successive experiment. After incubating the biomolecules the spotting tool was removed, the biochip was washed in D-PBS and the microfluidic cell was clicked on top before mounting the complete biochip in the analytical instrument.

3.4 Materials

In order to maximize the performance of the sensing measurements and for sake of reproducibility, all the sensing measurements have been always performed the day after the biomolecules immobilization. This is the reason why although the functionalization protocols have been developed mainly by the Imperial College group, all the biochips that were measured have been funtionalized at Politecnico of Torino providing the necessary information for the optimization of the technique.

A detailed list of the chemical and biological materials that have been used in this thesis is briefly presented below.

3.4.1 Chemicals

Sulfuric acid (95-98%), hydrogen peroxide (30% in H_2O), (3-Aminopropyl) triethoxysilane (APTES, 99%), ethanol (99.8%), glutaraldehyde solution (grade I, 50% in H_2O), sodium bicarbonate (99.7%), sodium cyanoborohydride (95%), hydrogen chloride (2M), glycine (98.5%), bovine serum albumin (BSA, 98%), fetal bovine serum (FBS) and Dulbecco's Phosphate Buffered Saline 1X (D-PBS) were purchased from Sigma-Aldrich and used as received. Dulbecco's modified Eagle medium (DMEM) was purchased from Lonza. NeutrAvidin Protein DyLight 650 (1 mg/mL) was purchased from Thermo Fisher Scientific. Anti-human VEGF capture antibody, recombinant human $VEGF_{165}$ protein (97%), biotinylated anti-human VEGF detection antibody , anti-human Angiopoietin-1 capture antibody , Anti-human Angiopoietin-2 capture antibody, biotinylated anti-human Angiopoietin-2 detection antibody, Human VEGF and Human Angiopoieitn-2 Quantikine ELISA Kit were purchased from R&D System. Water was purified by Millipore device.

3.4.2 Biological samples

All the biological samples were supplied by the Institute for Cancer Research and Treatment in Candiolo, Italy, by the group of Prof. Federico Bussolino.
Wild-type and biomarker-overexpressing Colo205 and MCF-7 cells were used. These latter were a kind gift of Prof. Roy Bicknell (University of Birmingham). MCF-7 cells are a human breast adenocarcinoma cell line extensively used in cancer research [Comşa et al. (2015)]. Cells were seeded in culture dishes at the density of $3.0 \cdot 10^6$ cells/cm^2 with DMEM containing 10% FBS. Serum-free medium was conditioned for 48h by confluent cultures. After collection, cell supernatants were cleaned by centrifugation (1500 rpm for 10 min at 4 °C) to remove particles. Samples were aliquoted and stored at -20 °C. Human plasma samples were from blood of cancer patients. Samples were collected in accordance with the protocol approved by the Institute's Ethical Commission and the Ethical Committee Piedmont Region, Torino, Italy. Plasma was prepared by centrifugation of the whole blood contained in the test tube with EDTA as anticoagulant; after centrifugation the corpuscolate fraction was discarded and the supernatant (i.e. plasma) was collected, aliquoted and stored at -80 °C. Plasma samples were analyzed with both the BSW biosensing platform and ELISA technique in order to validate the results. Commercially available kits from R&D Systems were used.

Chapter 4

Biosensing measurements

The goal of this thesis is to pre-clinically validate a compact and multifunctional point-of-care platform for real-time detection of cancer biomarkers in biological fluids with high sensitivity in a tandem configuration. As already mentioned, the two basic elements constituting the tandem approach are the label-free detection, based on a BSW resonance shift, and the spectral analysis of enhanced fluorescence emitted by biomolecules immobilized on the biochip surface.

The objective of the experiments is to measure very low concentration of angiogenic biomarkers coming from real world matrices like cell culture supernatant and human blood plasma from a pool of apparently healthy patients and patients with colonrectal cancer. This chapter is conceptually divided into three parts reporting the difficulties and the successes achieved during measurements:

- *First tests and modifications of the surface chemistry*
  The first batch of biochips was devoted to test the complete platform and the functionalized biochips with biomarker concentrations of the same order of magnitude of the real samples. During these assays a problem with the biomolecules immobilization was discovered and a complete batch of biochip have been used to develop a strategy to overcome it.

- *Results comparison between different matrices*
  Once surface chemistry issues were resolved, matrix effects were investigated for the detection of an important angiogenic factor, vascular endothelial growth factor (VEGF), in different matrices like Dulbecco's phosphate buffer saline (D-PBS), cell culture supernatant and human plasma samples.

- *Determination of Angiopoietin-2 in human plasma samples*
  Finally the fluorescence detection of the angiogenic factor Angiopoietin-2 (Ang2) in patients' plasma samples is presented. The biosensing system allows the detection of Angiopoietin-2 with similar analytical quality as laboratory methods, i.e. enzyme-linked immunosorbent assay (ELISA), but featuring short turnaround time, without any sample pretreatment and simple use.

4.1 First tests and modifications of the surface chemistry

The previous chapter described the protocol for the functionalization of the biochips and the immobilization of the biomolecules. The protocol was composed by four main steps:

1. APTES functionalization;
2. Glutaraldehyde crosslinker;
3. ProteinG (PtG) immobilization;
4. Antibody immobilization;
5. Bovine serum albumine (BSA) blocking (10mg/mL in D-PBS) at 4 °C overnight.

The steps 1-2 of the protocol were carried out over the whole surface of the biochips. The steps 3-4 were carried out after mounting on the biochips the five-channel flow cell. Primarily, the spotting tool was used to immobilize BSA (10 mg/mL) in two regions (channels) of the biochip surface and in three regions PtG (0.5 mg/mL). After 1 hour of incubation the biochip was detached from the tool and rinsed with D-PBS. The biochip was loaded again in the tool and the same three channels used for PtG were then filled with a solution containing the capture antibody, specific for the biomarker to be detected during the successive experiment. After incubating the biomolecules the spotting tool was removed, the biochip was washed in D-PBS and the microfluidic cell was clicked on top before mounting the complete biochip in the analytical instrument.

For the first set of experiments the following procedure was used:

- Baseline in D-PBS 1X.
- Injection and flush of 250μL of the analyte solution in D-PBS containing the biomarker.
- Injection and recirculation: 150μLof the same solution back and forward, 30 times.
- Wash: injection of 1000μL of D-PBS and then recirculation of 100μL 5 times.
- Injection and flush of 250μl of the detection antibody solution (2μg/mL) in D-PBS 1X.
- Injection and recirculation: 150μl of the same solution back and forward, 30 times.
- Wash: injection of 1000μL of D-PBS 1X and then recirculation of 100μL 5 times.
- Check for any fluorescence signal (fluorescence background measurement).
- Injection and flush of 250μl of Neutravidin solution (2μg/mL) in D-PBS 1X.
- Injection and recirculation: 150μl of the same solution back and forward, 30 times.
- Measure fluorescence.

Before starting each experiment, 1 mL of glycine-HCl (20 mM, pH 2.5) was injected and recirculated for 10 minutes to clean the surface. The measurement started in the label-free detection mode. In Fig. 4.1(b) it is shown the CCD camera image acquired in label-free mode for a functionalized biochip in D-PBS. Each pixel column corresponds to an angular component of the reflected beam and each row corresponds to a position along the illuminated region on the biochip surface. The BSW resonance appears as a dark vertical band. The angular position of the resonance puts into evidence the regions where the capture antibodies were immobilized, since the PDMS walls of the spotting tool leave residuals between adjacent channels that shift the resonance. However, such PDMS markers do not perturb in any way the measurement. The bio-conjugated regions are numbered in order to distinguish between each other.

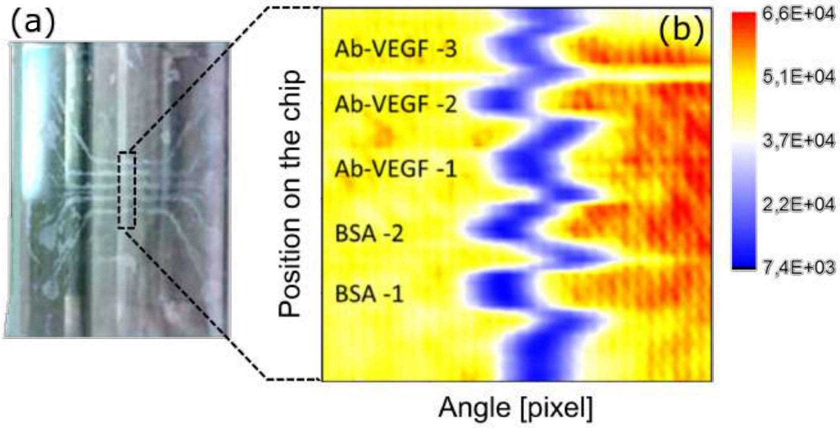

Fig. 4.1 (a) Photo of the 1DPC surface after the incubation with the spotting tool and before rinsing; (b) CCD reflectance map in label-free mode, the image was taken at the start of the experiment in D-PBS.

Fig. 4.2 shows the time dependency of the position of the minimum of the BSW resonance for the three spots where PtG+anti-VEGF antibody were incubated and the two spots with BSA. The first concentration of VEGF sent (t~9 min) was 31.25 pg/mL (i.e., the lowest standard suggested for the calibration curve related to the ELISA tests performed on biological samples as comparison) but any label-free binding signal was detected. Nevertheless, when injecting the detection antibody (t~42 min) and the neutravidin (t~95 min), a binding kinetic was observed for both.

The fluorescence detected by the CCD in the fluorescence mode is displayed in Fig. 4.3 and confirms the presence of the detection antibody and the neutravidin. The spots recorded by the CCD in the fluorescence mode of detection are identical to those defined in the label-free mode. Fig. 4.3(b) shows the integrated fluorescence intensity obtained for the regions considered before. The error bars represent the standard deviation of the integrated values.

Although the difference of weight between the VEGF molecule and its antibody is significant, it does not justify the difference observed in the sensorgram shown Fig. 4.2 between the magnitude of the signals observed upon injection of VEGF (t~9 min) and that of the detection antibody (t~42 min). Due to this discrepancy, other experiments were conducted in order to understand whether any non-specific binding of the detection antibody was present. First it was necessary to ensure that the capture antibody was present on the biochip. The biochips

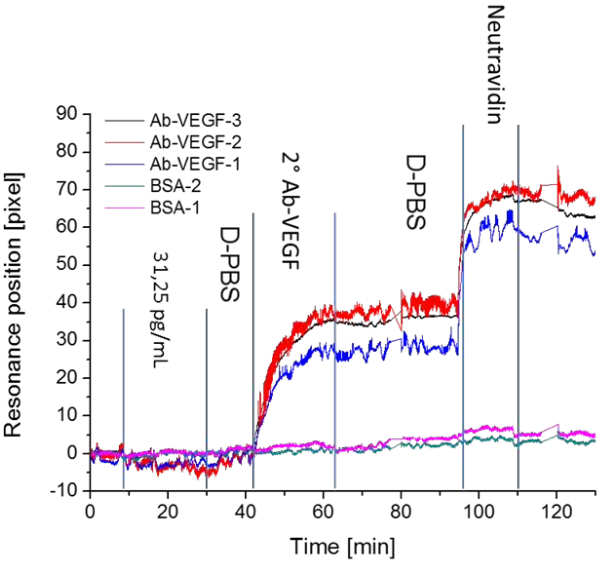

Fig. 4.2 Label-free sensorgram of different spots of the biochip surface upon the injection of 31.25 pg/mL VEGF solution in D-PBS. Detection antibody and the neutravidin were also injected. Although label-free signal of the VEGF was not evident, the binding of the detection antibody and of the neutravidin was observed.

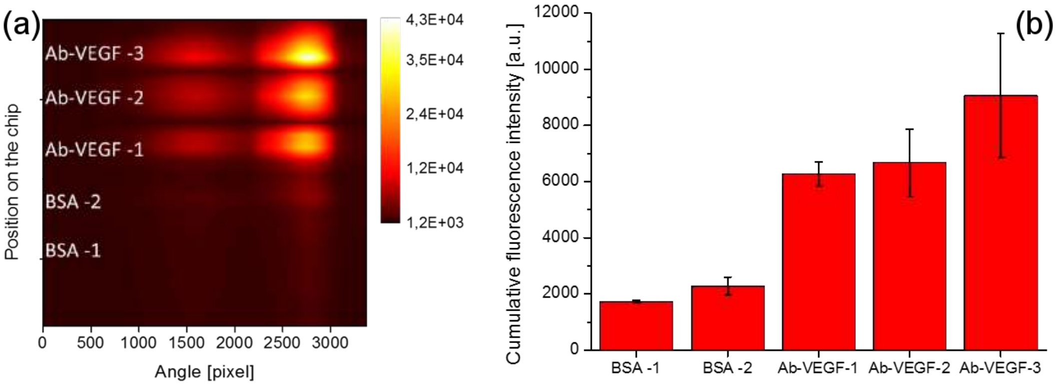

Fig. 4.3 (a) CCD camera image of the fluorescence emission of the neutravidin molecules that couples to the BSW mode; (b) integrated fluorescence intensity from the same spots considered in the label-free analysis.

were functionalized with APTES and GAH, then PtG and BSA were immobilized with the five-channel flow cell as described previously. The spotting tool was removed, biochips were whased with D-PBS, the fluidic cover was sealed and the biochip mounted on the platform. The capture antibody solution was injected directly in the microfluidic channel and the label-free signal was recorded. Two different concentrations of the capture antibody were injected, i.e., 20 μg/mL

(Fig. 4.4) and 40μg/mL (Fig. 4.6). After the washing step, the detection antibody and the neutravidin were injected, at the concentration of 2 μg/mL (Fig. 4.6 5) and 1 μg/mL (Fig. 4.6).

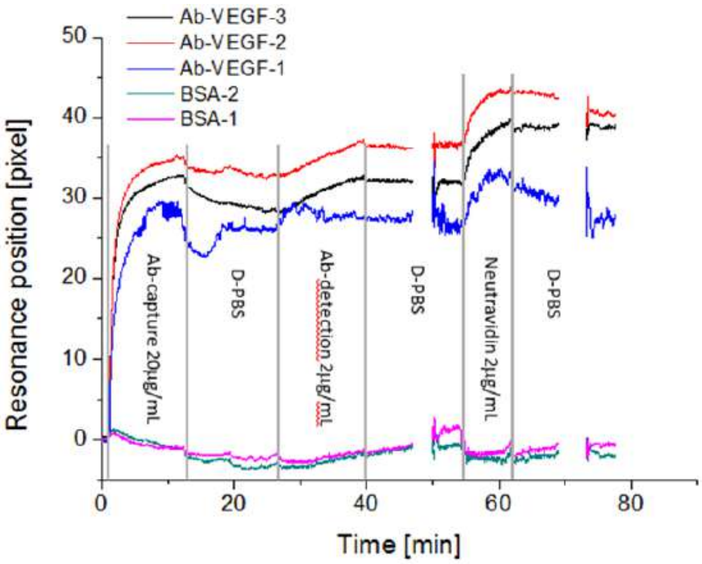

Fig. 4.4 Label-free sensorgram for a biochip that was functionalized with PtG and then incubated overnight in BSA. The first injection is the capture antibody that binds to the PtG. Then the detection antibody and the neutravidin are flown in the microchannel. Although any VEGF solution was injected a binding signal for both the detection antibody and the neutravidin is observed.

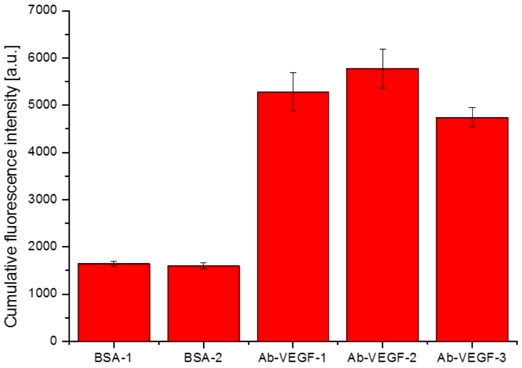

Fig. 4.5 Integrated fluorescence intensity detected by the CCD from the same spots considered in the label-free analysis. The presence of the fluorescence signal confirms that a non-specific binding was observed in label-free.

A clear binding of the capture antibody is observed in the PtG regions with respect to the blocked BSA reference regions. Despite the fact that any antigen was injected, a label-free signal for the detection antibody can be distinguished, only in the PtG regions, whereas no evident binding was detected in the BSA regions. This indicates the presence of not specific binding of the detection antibodies over the PtG regions. This is confirmed by the difference of the fluorescence intensities recorded in the regions bio-conjugated with either PtG or BSA.

From the comparison of Fig. 4.5 and Fig. 4.7, it is also clear that despites in the second experiment the concentration of the injected capture antibody was doubled, it was impossible to prevent the non-specific binding of the detection antibody, in fact the fluorescence intensities recorded are similar.

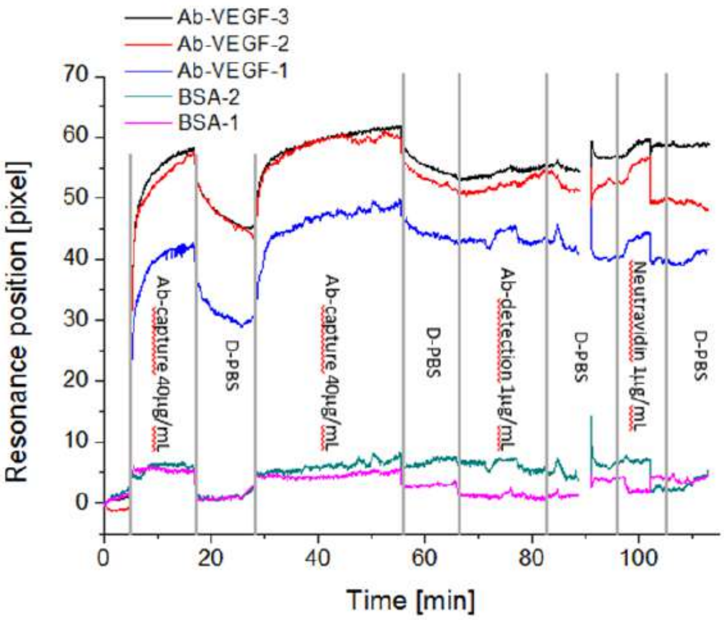

Fig. 4.6 Like in Fig. 4.4 biochip was functionalized with PtG and then incubated overnight in BSA. Two injections of the capture antibody were performed trying to saturate all the PtG binding sites. In this case, the label-free signal of the non-specific binding of the detection antibody and of the neutravidin is smaller.

The experiment was repeated with the injection of a 10 ng/mL VEGF solution in PBS (Fig. 4.8. No label-free binding can be identified upon the flown of the VEGF solutions. The capture antibody and the neutravidin were also injected, both with a concentration of 1ug/mL: the fluorescence intensity recorded by the CCD (Fig. 4.9) was of the same order of magnitude of the previous experiment (Fig. 4.7) but in that case any VEGF solution was added to the system.

The capture antibody did not succeed to saturate all the PtG binding sites and these lasts were free to bind the detection antibodies. Unfortunately this

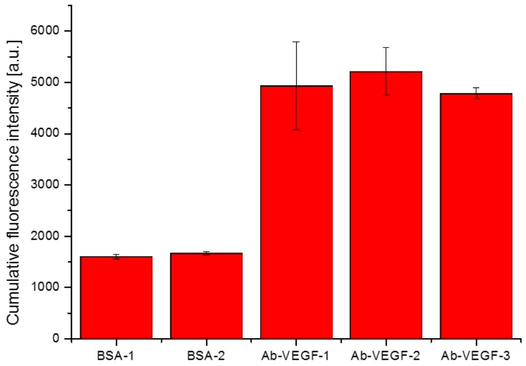

Fig. 4.7 Integrated fluorescence intensity detected by the CCD from the same spots considered in the label-free analysis. Fluorescence analysis reveals still the presence of a non-specific signal.

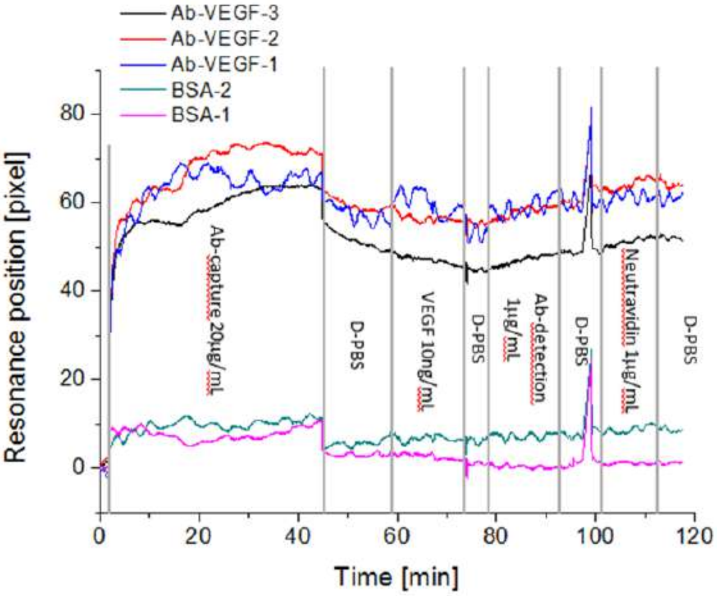

Fig. 4.8 In this label-free sensorgram after the injection of the capture antibody a solution of 10 ng/mL of VEGF in PBS was also injected. The biochip was functionalized with PtG and then incubated overnight in BSA. No evident binding on the VEGF was detected.

effect was predominant and masked the real signal that came from the effective presence of the biomarker on the surface.

A strategy was developed to overcome the problem described and the immobilization process was changed. The immobilization and use of the PtG layer was discontinued. The five channel functionalization flow cell was used to bioconjugate either specific antibodies for the target biomarker or other non-specific antibodies directly to GAH. In this way an on-chip negative reference region, very

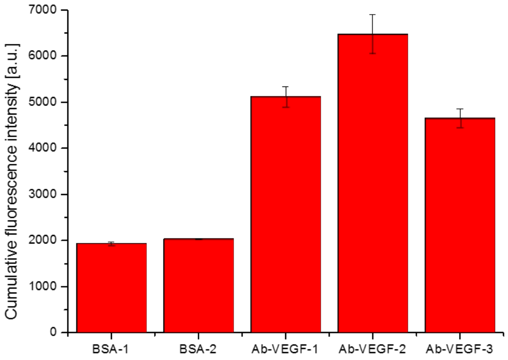

Fig. 4.9 Integrated fluorescence intensity detected by the CCD from the same spots considered in the label-free analysis. Intensities are similar to the ones reported in Fig. 4.7 when any VEGF solution was injected.

similar to the signal regions, was created. It was used to subtract any signal that arose from non-specific binding events. The functionalization and immobilization process changed to the following:

1. APTES functionalization;
2. Glutaraldehyde crosslinker;
3. Antibody immobilization;
4. Bovine serum albumine (BSA) blocking (10mg/mL in D-PBS) at 4 °C overnight.

This solution was adopted for the subsequent experiments. The results are reported in the next sections.

4.2 Comparison between different matrices

Blood plasma, together with serum, is one of the main sources of clinical analytes [Ehresman et al. (2007)]. Although it contains many disease biomarker, it is one of the most complex analytical matrix in which analytes are mixed with millions of other molecules [Treviño et al. (2009)]. This represents a serious obstacle for the development of clinical biosensors handling human plasma samples. Although many experiments were conducted with biomarkers spiked in simple matrices such as D-PBS, to obtain clinically relevant results it is essential to perform the biomarker detection in more complex matrices such as blood plasma or other biological fluids. In order to test the BSW biosensing platform for matrix effects, the attention was focused on different samples that contained the Vascular Endothelial Growth Factor (VEGF), an angiogenic inducer well known to play a key role in cancer progression and dissemination as well as in tumor angiogenesis [Ferrara (2010)]. Samples characterized by an increasing level of complexity were measured. More specifically, the lowest level of sample complexity was represented by solutions of D-PBS where a known amount of biomarker – in form of recombinant protein – was dissolved. Sample complexity increased with the use of cell culture supernatants, where low amounts of other molecules were released in addition to the biomarker. Finally, the highest level of sample complexity was represented by human plasma, i.e. complex heterogeneous systems. Cell supernatant samples and blood samples were tested for the presence of VEGF by ELISA and the results were compared with those obtained with the BSW biosensing platform.

More than 30 biochips for the detection of the VEGF in different matrices with label-free and fluorescence detection were tested. The calibration of the biosensing platform have been made using solutions of VEGF in D-PBS. In the case of matrices with a higher level of complexity, like supernatant and plasma samples, the label-free signal have been affected by the critical problem of protein fouling and are not reported. As can be seen from the experiments, fluorescence mode of detection was less penalized by this effect and even more sensitive. All experiments were carried out in duplicate.

The biochips were funtionalized with APTES chemistry as reported in previous section. In order to discriminate between specific and non-specific binding different antibodies were incubated in different regions of the functionalized 1DPC surface by means of the five-channel functionalization spotting tool. In following experiments, the five-channel functionalization flow cell was used to immobilize the anti-VEGF capture antibody as well as the anti-Angiopoietin 1 capture antibody used as negative control. Two channels were used to incubate 20 μg/mL of the anti-VEGF capture antibody, other two channels were filled with 20 μg/mL of the anti-Ang1 capture antibody and one was dedicated to BSA, 10 mg/mL. The volume used was 20 μL for each channel. The immobilization step lasted 1 hour and after the removal of the spotting tool, the biochips were rinsed with D-PBS and incubated overnight in a solution of 10 mg/mL of BSA in D-PBS at 4 °C, in order to block the surface.

Once the 1DPC surface is functionalized the microfluidic cover is clicked on top of the biochip before mounting the assembled biochip in the platform for the detection. The detection assay was reported in previous section. In the label-free mode, the biomarkers are directly recognized by the antibody-functionalized surface leading to the label-free signal. In the fluorescence mode, the biotinylated anti-VEGF detection antibody is injected in the flow cell and binds to the VEGF biomarker possibly immobilized onto the surface; the biotinylated antibody is in turn detected via a biotin-neutravidin recognition step, with an appropriate fluorophore that permits its detection in the fluorescence mode. The five measurement spots created with the spotting tool are numbered from 1 to 5 (Fig. 4.10). In all the experiments that are reported in this section, the Spot 3 and Spot 5 (signal spots), are bioconjugated to the anti-VEGF capture antibody, Spot 2 and Spot 4 to the anti-Ang1 capture antibody, whereas Spot 1 to BSA; Spots 1,2,4 are reference spots.

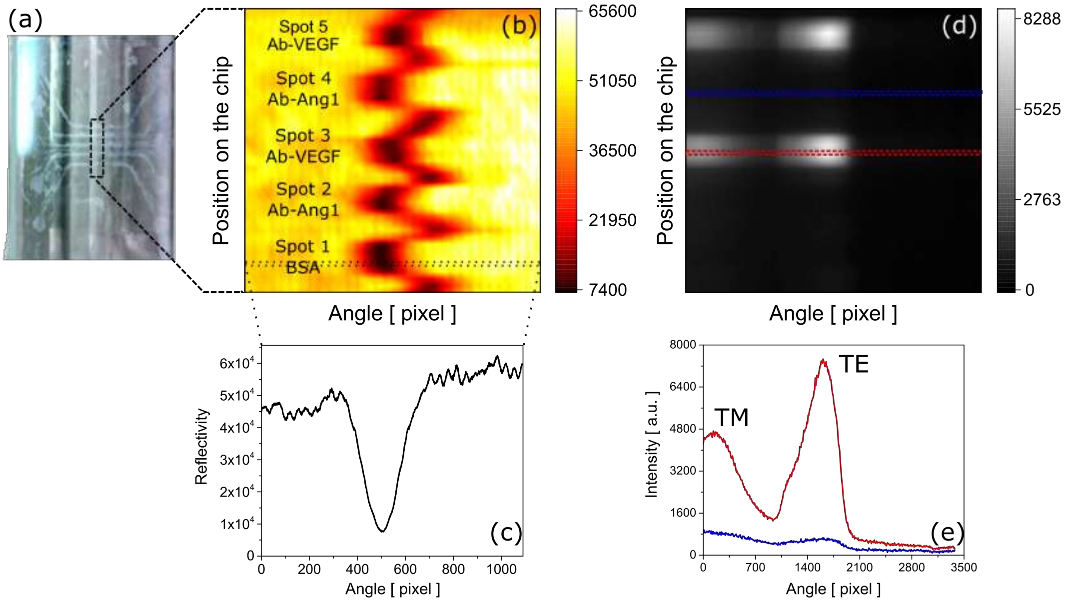

Fig. 4.10 (a) Photo of the 1DPC surface after the incubation with the spotting tool and before rinsing; (b) CCD reflectance map in label-free mode and (c) reflectance profile along the highlighted measurement line, the image was taken at the start of the experiment in D-PBS; (d) fluorescence emission recorded by the CCD camera the end of an assay where VEGF was detected; (e) angular emission profiles of the highlighted regions.

4.2.1 Label-free and fluorescence calibration curves

The label-free measurement recorded the position of the resonance dip to obtain the label-free signal. After a baseline in D-PBS, 300 μL of the analyte solution was injected and recirculated for 10 minutes. The injection and recirculation flow rate used in all the measurements reported was 30 μl/min. The biochip was then rinsed with plenty of D-PBS and the label-free detection was completed. The label-free sensor response was defined as the difference in the resonance dip position before the sample injection and after rinsing in D-PBS.

Biochips were prepared to detect increasing concentrations of VEGF in D-PBS in the range 50 to 500 ng/mL. Fig. 4.11(a,b,c) depict the binding of VEGF monitored in the label-free mode for three different biochips.

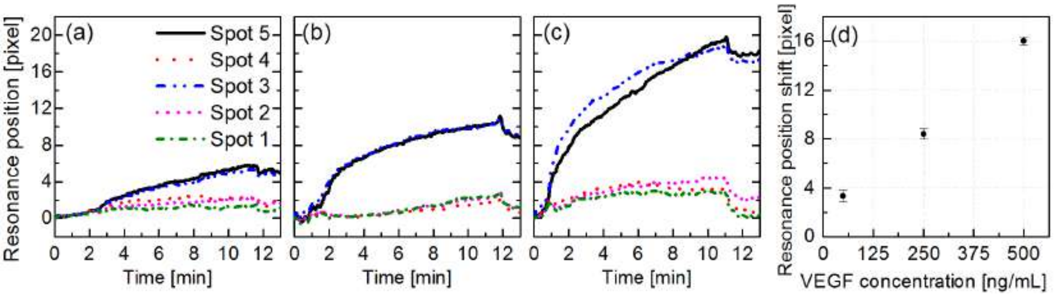

Fig. 4.11 Label-free sensorgrams for the detection of VEGF in D-PBS at concentrations of (a) 50, (b) 125 and (c) 500 ng/mL. Spots 3 and 5 have been functionalized with VEGF specific antibody while Spots 2, 4 and 1 were reference spots. (d) Resonance position shift plotted against biomarker concentration shows a good linearity.

The sensorgrams show the angular shift of the resonance for three different biochips. The residual shifts after the D-PBS washing were averaged in the signal and reference Spots. The label-free sensor response was then calculated as the difference between such averaged values. The results reported in Fig. 4.11(d) are the mean values of duplicate measurements. The label-free response is linear in the range of VEGF concentrations used in the assays and the sensitivity of the system was evaluated as S_{LF}^{VEGF} = 0.0286 pixel/[ng/mL]. The standard deviation of the noise, calculated on a 5 minutes baseline, was σ_{LF}^{VEGF} = 0.157 pixel. According to the IUPAC definition Butler and Laqua (1996), the estimated Limit of detection (LoD) for label-free operation can be calculated as $\mathrm{LoD}_{LF}^{VEGF} = 3\sigma_{LF}^{VEGF} / S_{LF}^{VEGF}$ = 16.5 ng/mL. The estimated LoD is an easy tool to compare the performance of different sensors. Despite this LoD is in line with optical label-free platforms that makes use of surface waves, it is still larger than reported plasma VEGF concentrations in healthy humans and cancer patients, ranging from a few tens to a few hundreds of pg/ml [Jelkmann (2001),Iinuma (2010),Ławicki et al. (2016)]. However, the platform can efficiently take advantage of the fluorescence mode of detection to decrease its LoD and open the way to the detection of lower amount of biomarkers in complex samples. For this reason it was decided to concentrate the efforts on the fluorescence detection.

To perform fluorescence detection, in a first phase 300 μL of bioninylated anti-VEGF-biotin in D-PBS (1 μg/mL) were injected and recirculated for 10 minutes. After rinsing with D-PBS, any fluorescence background signal was recorded. The switch between the label-free and fluorescence detection modes was automatically done by the control software when the the cylindrical *zoom* system was inserted in the optical path(see Chapter 2). While label-free source was switched off, fluorescence laser source was started and CCD settings were properly changed. Then 300 μL of a NeutrAvidin Protein DyLight 650 solution in D-PBS (1 μg/mL) were injected and recirculated for 10 minutes and finally a wash with D-PBS was performed before measuring the fluorescence signal. Fig. 4.10(d) displays the fluorescence detected by the CCD at the end of an assay in which a certain amount of VEGF was injected. In order to distinguish the Spots, it was possible to refer to the label-free map, in fact the number and the position of the spots recorded by the CCD in the fluorescence mode of detection are identical to those defined in the label-free mode.

A reliable and robust analysis of the fluorescence signal was set up using the complemental label-free signal. For each Spot the angularly dispersed fluorescence emission was acquired in 50 adjacent CCD camera rows (see the region between dashed lines in Fig. 4.10(d)). The label-free map was used as a mask to integrate the intensity of all the lines of a single Spot. First the background fluorescence was subtracted, then the angular intensity distribution recorded in each CCD row (Fig. 4.10(e)) was integrated along the angle. Hence, the integral values were averaged over the 50 rows and to each Spot it was assigned an intensity and its standard deviation.

The operation in the fluorescence detection mode was calibrated setting the minimum concentration measured in label-free as the largest. Thus, the spiked concentrations of VEGF in D-PBS were in the range 2.5-50 ng/mL. Fig. 4.12 reports the integrated fluorescence intensities of six different experiments, carried out with different biochips, that constitute one of the duplicate measurement of the fluorescence calibration. The error bars represent the standard deviation of the integrated values after the error propagation.

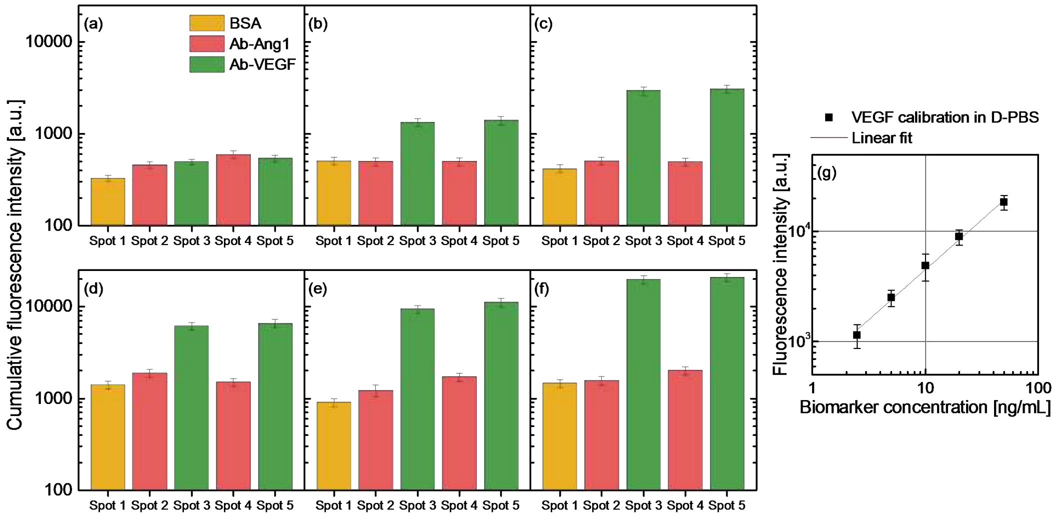

Fig. 4.12 Fluorescence intensity from VEGF solutions at different concentrations in D-PBS. (a) D PBS; (b) 2.5, (c) 5, (d) 10, (e) 20, (f) 50 ng/mL. (g) Calibration curve obtained by subtracting the averaged reference Spots intensity to the averaged signal Spots, each point is the mean value of duplicate measurements.

Fig 4.12a shows the case in which no VEGF was injected in the biochip (only the buffer). It appears that the detection antibody is non specifically absorbed onto the sensor surface and Neutravidin can bind to it resulting in a low non-specific fluorescence signal. The signal obtained is uniform over the whole surface. Fig. 4.12(b-f) refer to the case in which solutions containing VEGF were injected, with increasing concentration. Increasing fluorescence intensities are apparent in the signal Spots, with a good contrast with respect to the reference ones. For each VEGF concentration, the final fluorescence intensity is the difference between the averaged intensities of the Spots 3,5 and the reference. Their variances are summed in order to obtain the final standard deviations according to the error propagation theory. The resulting calibration curve is displayed in Fig. 4.12(g) where each point is the mean value of duplicate measurements. This calibration has been used to evaluate the unknown VEGF concentration in cell culture supernatant and spiked plasma samples. The fluorescence intensities obtained can be fitted with a linear function resulting in a sensitivity of S_F^{VEGF} = 460 [a.u.]/[ng/mL]. Making use of the standard deviation of the the blank it is possible to evaluate the limit of detection for the fluorescence mode of detection $LoD_F^{VEGF} = 3\sigma_F^{VEGF} / S_F^{VEGF}$ = = 0.98 ng/mL. Such value is one order of magnitude lower than the label-free limit and it is closer to the relevant VEGF concentration in human plasma samples.

4.2.2 Measurement of supernatant samples

Cell culture supernatants were the first step to test the BSW platform with more complex matrices. Cell supernatants collected from wild-type and $VEGF_{165}$-overexpressing Colo205 and MCF-7 cells were used. The concentrations of VEGF in cell supernatants were first assessed via ELISA. Wild-type Colo205 and MCF-7 cells expressed a VEGF basal level smaller than 1 ng/mL, while $VEGF_{165}$-overexpressing cells released an increased amount in the supernatant, i.e. 16.9 ng/mL. The measured concentrations are reported in Table 4.1.

Table 4.1 Results of ELISA tests for the assessment of biomarkers concentration in cell culture supernatants. Values are the mean ±SD of 3 experiments.

Cell type	**VEGF amount [ng/mL]**
MCF-7WT	0.770±0.005
MCF-7 $VEGF_{165}$	15.539±0.195
Colo205 WT	0.647±0.232
Colo205 $VEGF_{165}$	16.944±0.111

The VEGF concentration was measured in undiluted and diluted cell supernatants in D-PBS (Fig. 4.13). In particular, MCF-7 $VEGF_{165}$ sample was diluted by a ratio of 1:4 while Colo205 $VEGF_{165}$ sample by a ratio of 1:2. From the differential fluorescence intensities evaluated from Fig. 4.13(a-b) and making use of the fluorescence calibration curve shown in Fig. 4.12(g), it was possible to retrieve the following estimation of the VEGF concentration: 14 ng/mL and 4 ng/mL for the undiluted and 1:4 diluted MCF-7 $VEGF_{165}$ samples, respectively and 21.5 ng/mL and 8.5 ng/mL for the undiluted and 1:2 diluted Colo205 $VEGF_{165}$ sample. In Fig. 4.13(c) are plotted the fluorescence calibration curve together with data points corresponding to the intensities for the cell culture supernatant samples. These values show a good agreement between the BSW platform and results obtained via ELISA. Furthermore, the intensities obtained from the diluted samples are consistent with the undiluted ones. The reported results demonstrate that the biosensing platform can successfully perform biomarker detection in cells culture supernatants.

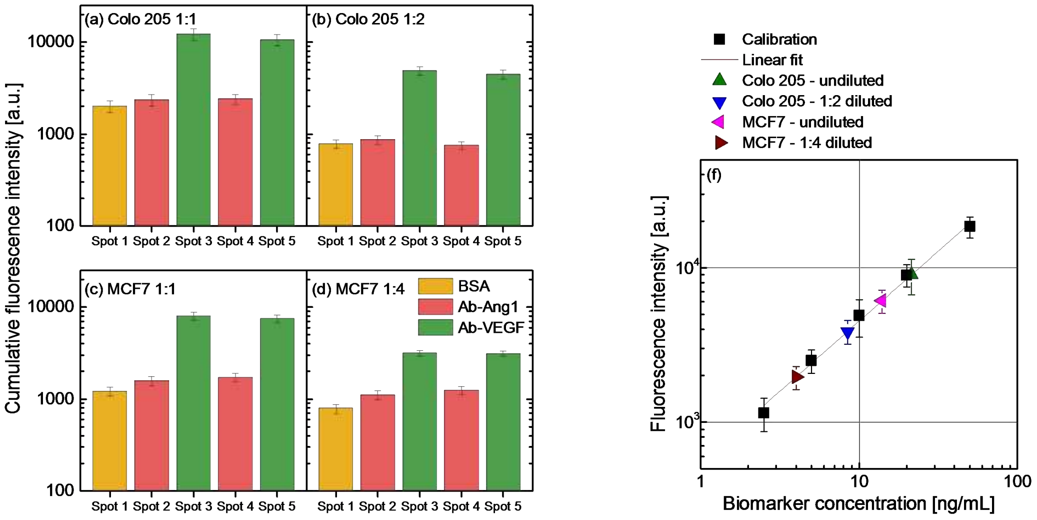

Fig. 4.13 Fluorescence intensities from cell culture supernatant samples: (a) undiluted Colo205 VEGF_{165} sample containing VEGF at 17 ng/mL; (b) 1:2 diluted Colo205 VEGF_{165} sample; (c) undiluted MCF-7 VEGF_{165} sample containing VEGF at 15.5 ng/mL; (d) 1:4 diluted MCF-7 VEGF_{165} sample. (f) Calibration curve (Fig. 4.12) and cell culture supernatant results.

4.2.3 Measurement of spiked blood samples

Human plasma samples were collected from a pool of apparently healthy patients. The total amount of sample used for one measurement is 300 μl. The concentrations of VEGF in the human plasma samples were assessed also via ELISA and revealed a concentration of VEGF lower than 0.3 ng/mL.

Due to the extremely low concentration of VEGF a certain amount of the recombinant VEGF protein was added in two plasma samples. The amount added was enough to obtain two samples at concentration 3.75 and 15 ng/mL. The results are shown in Fig. 4.14. The fluorescence signals in the Spots 3,5 could be distinguished from those in the reference Spots and the fluorescence intensities returned, through the calibration curve, VEGF concentrations of 3.5 and 14 ng/mL, for the two samples. Such values are in good agreement with the spiked concentrations. It is worth to mention that protein fouling, the unspecific adsorption on the sensor surface due to complex biological matrices, was not a problem for the fluorescence operation mode, both in supernatants samples and in plasma samples from different donors. The results presented in Fig. 4.13 and Fig. 4.14 show that the BSW platform, together with the strategy adopted to calculate the

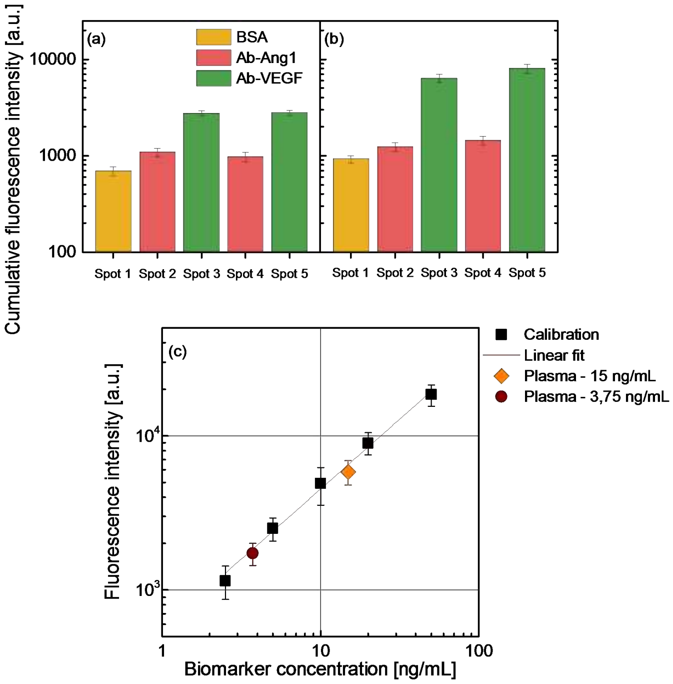

Fig. 4.14 (a) Fluorescence measurements of plasma sample with a spiked VEGF concentration of 3.75 ng/mL and (b) plasma sample with 15 ng/mL spiked concentration of VEGF. (c) Calibration curve (Fig. 4.12(g)) and spiked plasma samples results.

fluorescence intensity, allow to measure different biomarker concentrations in different complex matrices.

4.3 Determination of Angiopoietin-2 in human plasma samples

Angiogenesis, the formation of new blood vessels from pre-existing ones, is one of the most intensively studied areas of cancer research in recent years. Although in adulthood angiogenesis is generally required to repair tissue and remodel tissues involved in menstruations, cancers can use angiogenesis to allow their growth and metastasis [Maisonpierre et al. (1997)]. Indeed, after reaching a diffusion-limited size, many tumors rely on an angiogenic switch, rendering tumor angiogenesis one of the hallmarks of cancer. In basic research, traditional (largely qualitative) biochemical, biomolecular and microscopy-based techniques had provided fundamental information with regard to the main mechanisms involved in tumor angiogenesis. The release of angiogenic factors by tumor cells establishes a dynamic tumor microenvironment where intricate intracellular paths lead to the phenotypic changes required to sustain tumor growth. Angiopoietin ligands belong to a novel class of angiogenic factors that, together with Tie receptors, play a critical role in blood and lymphatic vessel development, inflammation and tumor vascularization [Eklund and Saharinen (2013)]. Among angiopoietin molecules, Angiopoietin-2 (Ang2) has been widely investigated due to its function in the inhibition of the tumor vasculature and in other pathological conditions associated with endothelial dysfunction [Eklund and Saharinen (2013),Loughna and Sato (2001)]. Quantitative detection of angiogenic biomarkers such Ang2 can be a powerful tool to diagnose cancers in early stages and to follow its progression during therapy [Pepe et al. (2001)]. Moreover, Ang2 plasma level has been found to be correlated with cerebral cavernous malformation [Zhao et al. (2016)] and disease severity in human cancers [Park (2007)]. It may also assist in the diagnosis of difficult lesions [Teixeira et al. (2016)]. Monitor Ang2, as well as other angiogenic factors, is therefore desirable for future development of targeted anti-angiogenesis therapy in cancer and/or in other diseases.

Here it is presented the enhanced fluorescence detection of Ang2 biomarker directly from human plasma. This was the first biosensor assay that used BSW for the detection of Ang2 from patients' plasma samples at clinically relevant concentrations.

Biochips were functionalized and measured according to the procedures described in the previous sections. Also in these experiments a sandwich immunoassay format with antibodies against Ang2 immobilized on the 1DPC surface was chosen. The five channel functionalization flow cell was used to immobilize the specific anti-Ang2 capture antibody as well as BSA molecules and a non-specific capture antibody, precisely the antibody specific for VEGF. Two channels were used to incubate 20 μg/mL of the anti-Ang2 capture antibody, other two channels were filled with 20 μg/mL of the anti-VEGF and one was dedicated to BSA, 10 mg/mL. The volume used was 20 μL for each channel. The sandwich immunoassay adopted is sketched in Fig. 4.15 as a reminder.

Analyzed liquid samples were flowed over the functionalized biochip (Fig. 4.15(a)) and Ang2 molecules bond to the surface (Fig. 4.15(b)). In order to detect a fluorescence signal a biotinylated detection antibody solution (1 μg/mL in D-PBS) was injected in the microfluidic channel. At this point the fluorescence background

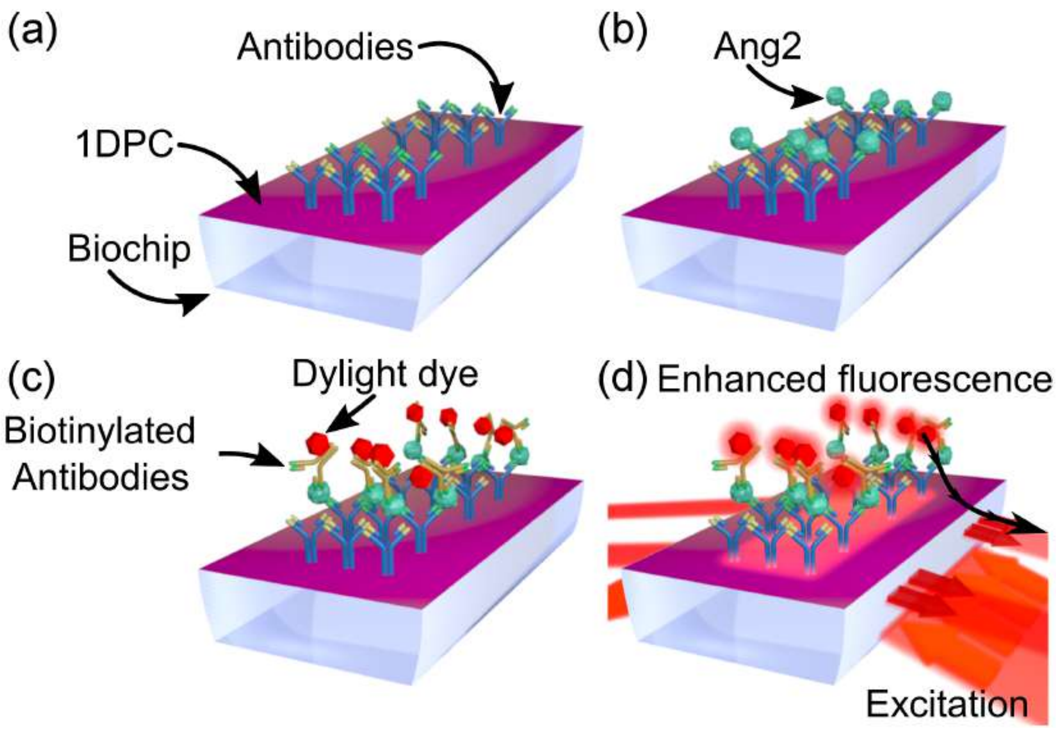

Fig. 4.15 Sandwich assay for the detection of Ang2 biomarker. Refer to text for details.

was recorded. The detection antibody was in turn labelled with an appropriate fluorophore (NeutrAvidin Protein DyLight 650, 1 μg/mL in D-PBS, Fig. 4.15(c)). Fluorescence detection (Fig. 4.15(d)) was performed after a final wash of the microfluidic channel. The volume of all solutions used, from the analyte solution that contained the target biomarker to the one in which the labelling dye was present, was 300 μL and all the solutions were recirculated for 10 minutes. Between each step the microfluidic channel was rinsed with abundant D-PBS increasing the flow rate to 50 μL/min.

Fig. 4.16(a) displays the arrangement of the bio-conjugated regions together with the fluorescence intensity of detected by the CCD at the end of an experiment in which a certain amount of Ang2 was injected (Fig. 4.10(b)). A clear fluorescence signal arose from regions that were bio-conjugated to anti-Ang2, while poor signal strength was observed from the reference regions.

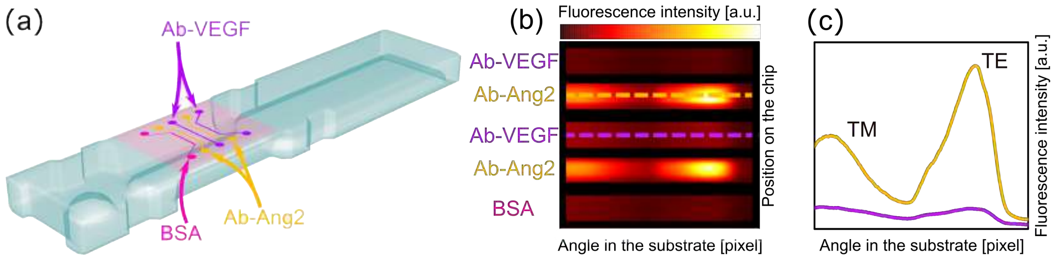

Fig. 4.16 (a) Sketch of a functionalized biochip after the incubation with the spotting tool; (b) fluorescence emission recorded by the CCD camera the end of an assay where Ang2 was detected; (c) angular emission profiles of the highlighted regions.

4.3.1 Fluorescence characterization and immunoassay limit of detection

Ang2 levels in patients with cancer are generally higher than 1 ng/mL [Caine et al. (2003),Engin et al. (2012a),Engin et al. (2012b)]. In order to use the BSW biosensing system to quantify Ang2 levels in patients' plasma it needs to be calibrated. To this purpose, duplicate standards of Ang2 in the range 2.5 to 50 ng/mL were prepared in D-PBS by serial dilution of a stock solution of 1 mg/mL of Ang2 in D-PBS. Calibration curves were obtained employing concentrations of 2.5, 5, 10, 20 and 50 ng/mL. Pure D-PBS was used as negative sample. Fig. 4.17(a) shows the fluorescence intensities recorded by the CCD for the calibration curve concentrations. In case only D-PBS was injected during the measurement, the platform detected a very low uniform signal from the whole surface. However, when a solution which contains Ang2 was injected, the produced signal by the anti-Ang2 regions could be distinguished with a good contrast.

Fig. 4.17(b) reports the integrated fluorescence signal of analogues regions. The bar plot shows increasing signal in response to increasing Ang2 concentrations. Standard deviations of the mean values were calculated as the sum of the variances associated to the signal emitted from each region according to the error propagation theory. It is worth to mention that such standard deviations spread with increasing concentration of Ang2 but relative values are constant.

On chip reference regions have been introduced purposely to take into account any effect that may alter the detected signal, i.e. non-specific absorption of any molecule. The overall response of the system was assessed as the difference between the averaged intensities of the regions bio-conjugated with anti-Ang2 and

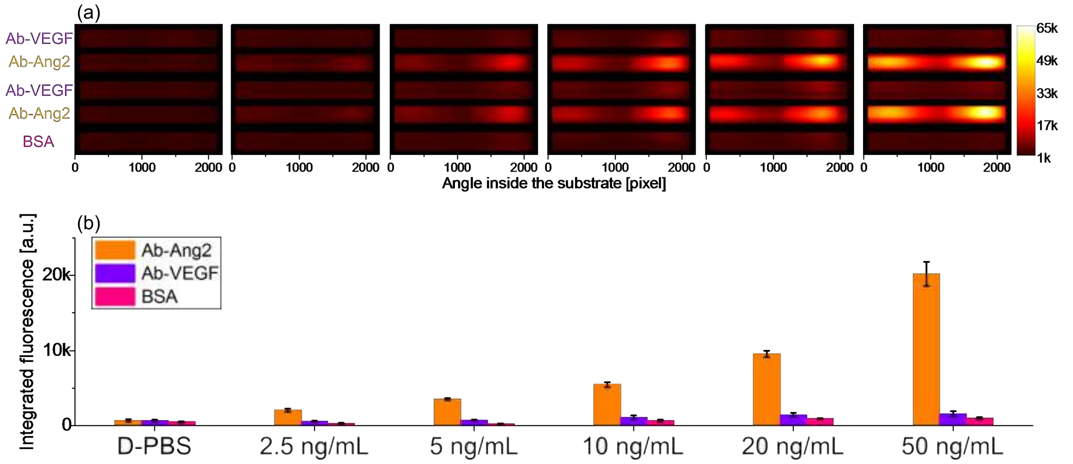

Fig. 4.17 Fluorescence intensities from Ang2 solutions at different concentrations in D-PBS. (a) Fluorescence intensities recorded by the CCD at the end of the assay. Each concentration correspond to a single assay conducted on a single biochip. (b) Integrated and averaged intensities for related regions of the functionalized biochips, error bars represent the standard deviation associated to the integrated and averaged values.

the reference regions.

The averaged responses of the two standards measured for each concentration are plotted versus the Ang2 concentration in Fig. 4.18 and fitted to a four-parameter Boltzmann equation:

$$y = \frac{A_1 - A_2}{1 + e^{(x-x_0)/A_3}} + A_2.$$

where y is the measured fluorescence intensity, x is the Ang2 concentration, A_1 and A_2 are the asymptotic minimum and maximum respectively. the slope in x=x_0 is S_F^{Ang2}=(A_2- A_1)/4A_3. The function was chosen to take into account that the enhanced fluorescence signal produced by the 50 ng/mL solution almost saturated the CCD detector. All the measurements have been conducted with the same exposure time but in case of need this setting can be reduced and the biosensing system can explore higher ranges of concentration.

The slope S_F^{Ang2} in the linear region the sensitivity of the BSW platform for this bioassay. The LoD can be evaluated making use of the standard deviation of the blank through the formula $LoD_F^{Ang2} = 3\sigma/S_F^{Ang2}$ ~1.5 ng/mL. This calculated LoD is compatible with the concentration ranges of Ang2 in plasma from patients with metastatic colorectal cancer [Caine et al. (2003),Engin et al. (2012a),Engin

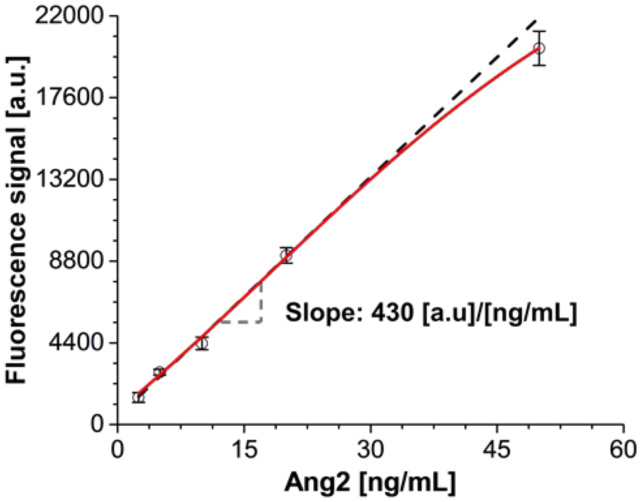

Fig. 4.18 Calibration curve of Ang2 in D-PBS. Each point represents the mean value of two replicate measurements.

et al. (2012b)]. The obtained calibration curve has been used to evaluate the Ang2 concentration in patient plasma samples.

4.3.2 Detection of Ang2 in human plasma samples

Collection, processing, storage and use of human blood samples strictly adhered to the protocol approved by the Institute's Ethical Commission and the Ethical Committee Piedmont Region, Torino (Italy). Patient's identifiers are kept to a minimum, i.e., the normal personal identifiers were replaced by an artificially-created identifier that here are reported as "Plasma sample" 1/2/3. For each patient, after obtaining informed consent, blood sampling was done in order to obtain plasma samples before a therapy cycle, during the therapy, and after the therapy. After having informed the patient, during a routine blood sampling for diagnostic purpose an additional blood volume (~12 mL) was collected. The additional blood volume was collected in different test tubes to allow plasma preparation. Plasma were prepared according to the procedure described in previous sections. Considering the same biological sample, some aliquots of plasma were assayed for the quantification of Ang2 by ELISA, while others were devoted to the measurement via the BSW system. Three different samples were measured. Two plasma samples, i.e. plasma sample 1 and 2, were collected from the same patient but in different moment of the tumor progression. ELISA determination revealed that the Ang2 concentration was around 6 ng/mL in all the three samples. Samples' aliquots were then measured with the developed BSW system and the results are reported in Table 4.2. These data reveal good agreement between both methods with percentage deviation from ELISA results less than 10%. Duplicate measurements of each sample were considered.

Table 4.2 Detected Ang2 in plasma samples from metastatic colorectal cancer patients by BSW system in comparison to ELISA. For the BSW system, each calculated value represent the mean of duplicate measurements.

	Detected Ang2 concentrations [ng/mL]	
	BSW platform (σ)	ELISA
Plasma sample 1	6.2 (0.4)	6.7
Plasma sample 2	5.8 (0.4)	5.7
Plasma sample 3	5.3 (0.2)	5.8

The bioassay accuracy can be assessed by evaluating the results variability for the same plasma sample. The concentrations obtained are the mean value of duplicate measurements done in different days every time with a pristine sample. The coefficients of variation for plasma sample measurements are reported in Table 4.3. The table present also the variability of the calibration procedure. As already mentioned, duplicate standard curves were prepared and each concentration, i.e. 2.5, 5, 10, 20, 50 ng/mL, was tested on a single biochip. Mean values of the coefficient of variations are below 6% for both plasma measurements and standards. Moreover, all the individual values are below 10%. These coefficients are acceptable variability values for analytical methods.

Table 4.3 Assay variations in plasma samples measurements and in the calibration procedure.

	Sample 1		Sample 2		Sample 3	Mean
Coefficient of variation of measured plasma samples	6.68		7.23		3.18	5.70
	Calibration curve points [ng/mL]					
	2.5	5	10	20	50	
Coefficient of variation of standards	5.9	5.53	7.62	5.14	5.34	5.78

Chapter 5

More compact readout scheme: gratings and BSW

Among the optical readout schemes, fluorescence has become the dominant detection/sensing technology in medical diagnostics and biotechnology [Taitt et al. (2016),Lakowicz (2006)]. The microarray approach provides a simultaneous analysis of thousands of parameters within a single experiment, resulting in rapid response time analysis. In the attempt to provide a more compact and miniaturized chip for an enhanced fluorescence biosensing, in this chapter a nanopatterned 1DPC structure is proposed. This section was published in Ricciardi et al. (2015).

5.1 Nanopatterned 1DPC

The nanopatterned 1DPC is integrated on a PDMS lab on a chip for a miniaturized fluorescence assay. The optofluidic chip is made of a photonic substrate constituted by amorphous materials deposited on glass and a PDMS fluidic membrane for solution/analyte handling (sketch in Fig. 5.1).

The photonic structure is based on a 1DPC that is surface-patterned as an array of linear subwavelength corrugations. The use of such a photonic substrate allows an enhancement and a beaming of the emitted radiation towards the observer, in such a way that the fluorescence collection is largely improved even with low-cost optics. The overall system can be optically interrogated by means of an extended excitation laser beam. The resulting fluorescence can be collected through a collection optics arranged in a simple wide-field configuration, with no

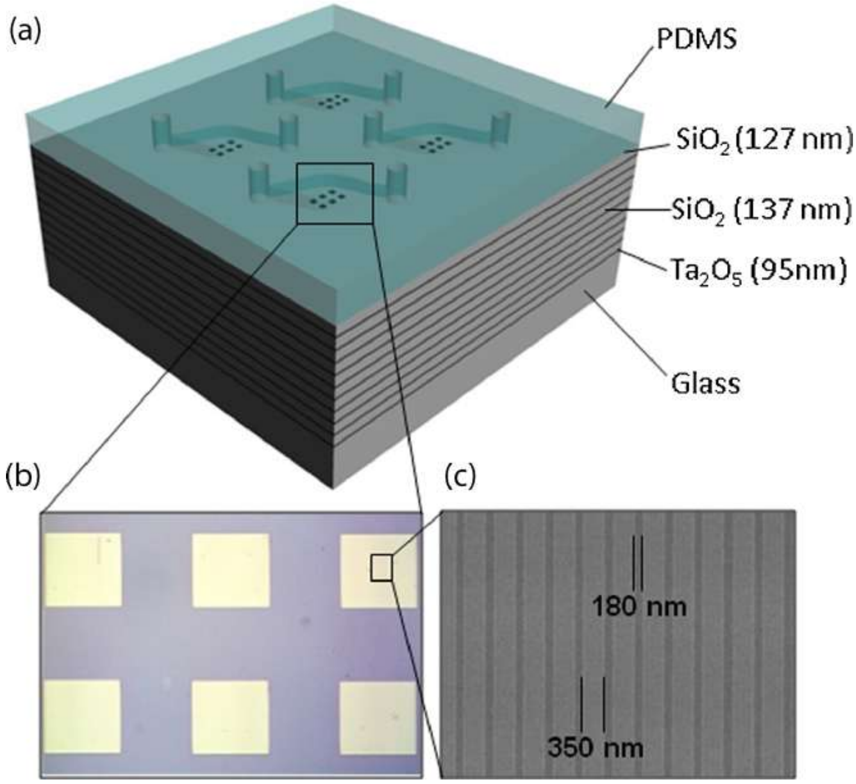

Fig. 5.1 Schematic (a) sketch of the optofluidic chip. A 1DPC is patterned with 4 groups of linear subwavelength gratings and bond to a PDMS microfluidic membrane whose 4 independent cells (provided with independent inlet and drain channels) are respectively aligned to each of the grating groups; (b) optical image of 1 grating group constituted by 6 gratings; (c) SEM image of a detailed portion of a linear grating.

need of any scanning mechanism. Thanks to the high transparency and optical quality of the PDMS cover, the optical excitation/detection can be implemented from either the PDMS or the glass substrate side [Choi and Cunningham (2006)]. The 1DPC is constituted by 20 alternating layers of Ta_2O_5 and SiO_2, deposited on a thin glass substrate by PIAD. The Ta_2O_5 and SiO_2 layers are 95 and 137 nm thick respectively, while the top SiO_2 layer is only 127 nm thick. On top of the stack a pattern of linear gratings with a period of $\Lambda = 530$ nm is fabricated by electron beam lithography, followed by a sputter deposition of SiO_2 (K. J. Lesker PVD 75 DC Magnetron Sputtering). Gratings are arranged into four groups, each group including six grating pads, 250 μm × 250 μm in size. Grating groups are respectively separated by 4 mm, in such a way that each group can observed with a single micro-fluidic cell, with independent inlet and outlet. The resulting grating height is about 100 nm. In order to provide a practical implementation of the

BSW-assisted fluorescence detection, the photonic structure is integrated onto a PDMS microfluidics and a biosensing protocol as follows is performed. The immunological assay consists of the specific recognition of Actin and Anti-Actin antibody molecules. Antibody species are immobilized on the solid support, upon proper chemical modification. Fluorescently labelled Actin molecules(Actin-Alexa Fluor 568) are employed as target molecules. The specific binding of Antibodies on the 1DPC surface is promoted by a functionalization procedure based on APTES (ref Chapter 3). After the surface functionalization, the photonic structure can be bonded to the PDMS microfluidics. Antibody solutions (50 μg/ml) are incubated all over the surface. As a result, the biomolecules are covalently grafted [Fiorilli et al. (2008)] both on the linear gratings and outside them, on the flat 1DPC surface. After incubation, samples are deeply rinsed in PBS-Tween 20 (0.05%) and in deionised water, to remove non-specific signal derived from molecules not covalently grafted on the surface; then samples are dried under nitrogen flux.After antibodies immobilization, Actin-Alexa Fluor 568 solutions at different concentrations are incubated corresponding to the four different grating groups (covering areas inside and outside the gratings). Then, a rinsing step in PBS-Tween 20 (0.05%) and in deionised water is performed. Finally, a nitrogen stream is used for drying.The detection is performed by means of a simplified fluorescence microscope, as illustrated in Fig. 5.2.

Briefly, fluorescence is excited with a doubled frequency Nd:YAG laser beam (wavelength $\lambda = 532$ nm) that is firstly focused from a single-mode fibre and then collimated onto the sample through a NA = 0.1 objective. The laser spot can homogeneously illuminate a single grating pad. Illumination is incident from the glass substrate (bottom side) and polarized parallel to the grating groves. This arrangement allows for the resonant excitation of BSW by means of the laser, providing an additional mechanism for fluorescence enhancement. On the air-side, the fluorescence emitted in the free-space and the transmitted laser light can prop-agate through the transparent low-roughness PDMS membrane and collected by a NA = 0.2 objective. After laser filtering, a fluorescent image of the photonic crystal surface is obtained. Thanks to the BSW-assisted beaming effect described above, the corrugated areas show a brighter fluorescence intensity that can be directly compared to the flat 1DPC regions imaged within the collection objective field of view. It should be noted, however, that lower NA optics can be used in alternative, since the BSW-assisted fluorescence beaming shows a

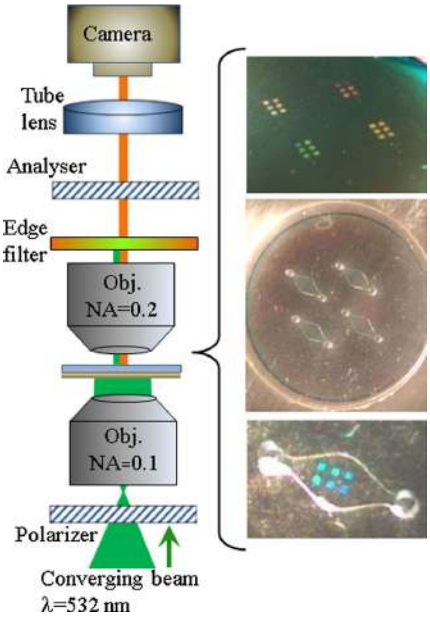

Fig. 5.2 Sketch of the optical setup for microarray fluorescence imaging. Also shown, exemplary pictures of the optofluidic chip hosting 4 groups of linear gratings and the PDMS microfluidics.

divergence well below an angular spread of 10 deg. The analyzer in the collection path is not used here.

5.2 Computational model

The one dimensional photonic crystal (1DPC) has been designed in such a way that TE-polarized BSW are allowed to propagate at their truncation surface. In this case, BSW are sustained for wavelengths shorter than 620 nm. In previous chapters, the angular emission distribution have been demonstrated to change significantly for fluorophores located in close proximity to the 1DPC surface. As already stated, a light source oriented with its dipole momentum parallel to the 1DPC flat surface (as sketched in Fig. 5.3(a)) can couple a significant portion of the emitted power into the BSW sustained by the 1DPC itself. This BSW-coupled fluorescence propagates as a surface wave on the 1DPC surface, as illustrated by the Finite Element Method (FEM) calculations shown in Fig. 5.3(b). During the surface-propagation, the BSW-coupled fluorescence leaks into the glass substrate, where it radiates as a free-space wave along a specific direction determined by the BSW wavevector. The readout scheme used in the previous chapters exploited a prism configuration to detect the BSW-coupled fluorescence. In alternative, if the

1DPC is patterned with a linear corrugation having a suitable period (Fig. 5.3(c)) and the emitter is still located close to the surface, the BSW-coupled fluorescence propagating parallel to the grating direction is directly diffracted and shot out in the free space [Angelini et al. (2014a)]. This mechanism is illustrated by the FEM calculations presented in Fig. 5.3(d and e), wherein a high-intensity beam of light emitted normally to the 1DPC surface is observed. The advantage of using a suitable diffraction grating on top of the 1DPC can be better appreciated when the angular distribution of the integral power emitted by the source on the photonic structure is considered (Fig. 5.3(f)).

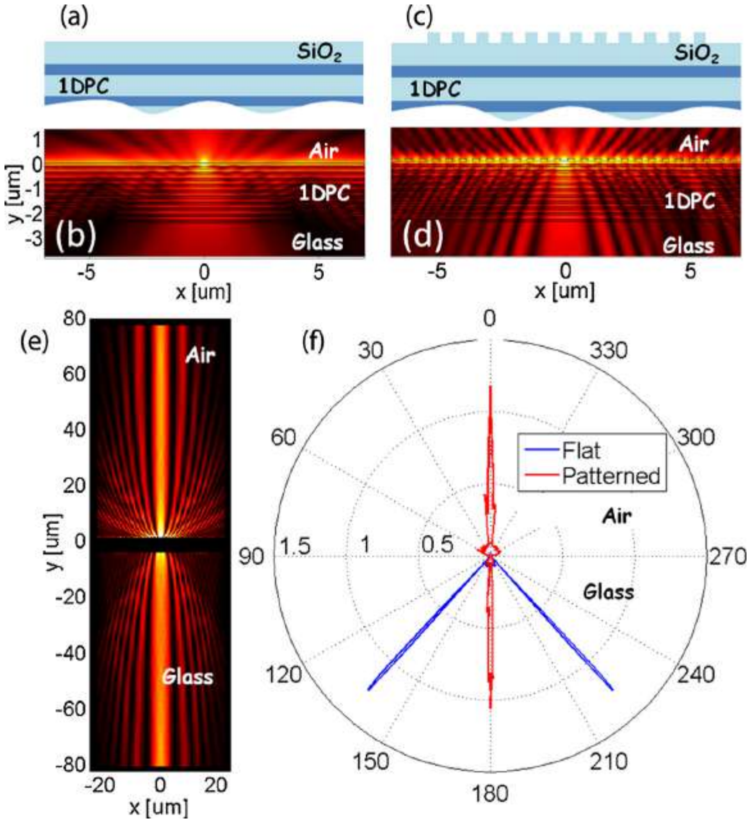

Fig. 5.3 Cross sectional sketch of flat (a) and patterned (c) multilayer; calculated near-field intensity distribution of light radiated by an emitter close to the surface of a flat (b) and patterned (d) multilayer; (e) expanded view of the intensity distribution of BSW-coupled diffracted fluorescence; (f) angular pattern of emitted light in the case of flat and corrugated 1DPC, highlighting the BSW-assisted beaming.

The linear grating out-couples the BSW-coupled fluorescence that would be otherwise leaking into the glass substrate (blue line) and barely detected without using a prism or an immersion optics. As a result, a spectacular beaming effect (red line) is produced, shooting the emitted fluorescence normally to the 1DPC surface with a very low angular divergence. Due to the linear geometry of the grating, this beaming effect occurs substantially on a plane containing the grating vector.In this way, a very low numerical aperture (NA) collection optics can indeed be used to efficiently collect a large amount of emitted fluorescence, therefore improving the performance of a low-cost fluorescence assay. The use of transparent, dielectric materials allows an easy design of photonic structures exhibiting (diffracted) BSW tuned at the desired emission wavelengths of operation [Angelini et al. (2014b)]. In the calculations presented in Fig. 5.3, the emitter radiates at a wavelength λ = 580 nm, thus demonstrating the capability of the proposed photonic structure to operate in the visible spectral range.

5.3 Fluorescence detection

When the fluorescence-labelled biomolecules are grafted on the photonic surface of the optofluidic chip, it is possible to produce a fluorescence image of each single grating by adjusting the magnification of the detection unit previously shown. In alternative, an imaging setup may be provided, allowing a wider field-of-view containing multiple gratings that can be collectively illuminated.In the present case, the laser homogeneously illuminates a single grating pad. The signal enhancement on the grating can be appreciated from Fig. 5.4(a), wherein exemplary fluorescence images of the photonic crystal surface are considered. The illumination spot (yellow dashed circle) is slightly offset with respect to the grating, in such a way that the fluorescence intensity discontinuity at the grating edge can be clearly observed. Then, a cross-sectional intensity profile across the illuminated area can be taken corresponding to the grating. This intensity distribution is directly compared and superposed to the fluorescence profile of the illumination area without grating (Fig. 5.4(b)). The illumination power being the same,the on-grating fluorescence shows an intensity enhanced approximately by a factor of 20. A titration curve can be built, by using different concentrations of Actin-Alexa Fluor solutions as target (0.042 μg/ml,0.084 μg/ml, 0.168 μg/ml, 0.420 μg/ml, 0.840 μg/ml, 1.680 μg/ml,4.2μg/ml, 8.4 μg/ml, 16.8 μg/ml, 42 μg/ml, 84 μg/ml, 168 μg/ml) in D-PBS prepared by serial dilution. Till to four different solutions of Actin-Alexa Fluor are simultaneously incubated on the four different gratings groups, each one provided with a dedicated microfluidic chamber. Fluorescence intensities are collected from the gratings and from the flat regions beside the gratings and plotted as shown in Fig. 5.4(c).For each Actin concentration, the quantification of the fluorescence intensity has been performed by calculating an average intensity over the illuminated areas either on gratings or on flat regions. The error bars take into account the intensity variation within each spot and over the 6 gratings incubated at identical concentration. Collected data are well fitted by sigmoidal profiles, as expected. At low concentrations, the fluorescence intensity is dominated by the background, thus preventing small changes in the amount of Actin molecules grafted on the surface to be resolved. The background is estimated by collecting the fluorescence from the photonic crystal surface with no Actin-Alexa Fluor molecules incubated on it. However, as the photonic enhancement mechanism occurs also for the background fluorescence, two different background levels have to be considered separately for grating and flat regions. More particularly, the background level on the grating is higher (see Fig. 5.4(c)).

At increasing concentrations, the fluorescence collected on the gratings is significantly enhanced as compared to the flat areas. This signal enhancement leads to an overall decrease of the limit of detection (LoD) for Actin concentration by a factor of about 40, as illustrated in the figure. For the LoD determination, the mean background level (with only APTES on the surface) increased by 3σ as a threshold was considered, where σ represents the standard deviation of the background fluorescence. As a result, in this assays, Actin down to 0.168 μg/ml concentration can be clearly detected on the gratings, whist on flat areas it is not possible to discriminate from the background Actin concentrations lower than 8.4 μg/ml.

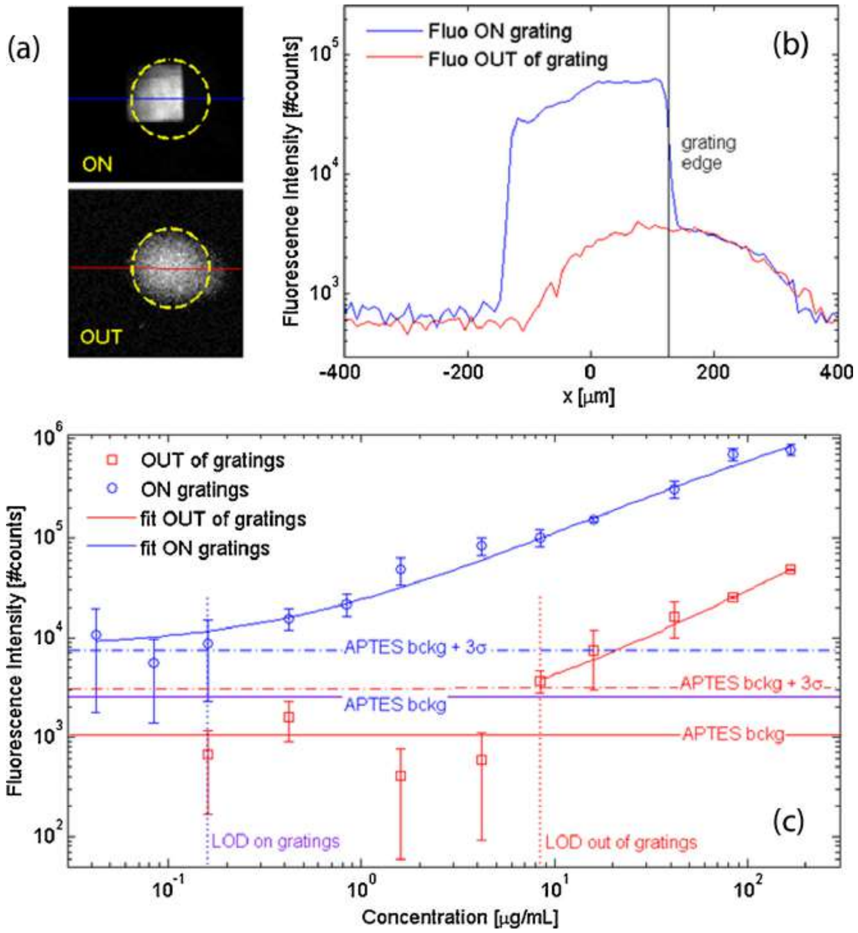

Fig. 5.4 (a) Fluorescence image of the photonic crystal surface (grating and flat area), illuminated by a collimated laser beam. The illumination beam is indicated by the dashed yellow circle and is slightly offset with respect to the grating position; (b) cross sectional intensity profiles of fluorescence across the grating (blue solid line) and across the flat area (red solid line), illuminated by the same laser beam intensity. An increase by approximately a factor of 20 is observed in the collected fluorescence corresponding to the grating, as compared to the outside; (c) titration curve of fluorescence collected for different labelled Actin-Alexa concentrations, grafted to Anti-Actin receptors. The increase of the fluorescence intensity shifts down the minimum observable Actin-Alexa concentration by a factor of 40 approximately.

Chapter 6

Conclusions

In this thesis manuscript, I have shown many of the aspects related to BSW biosensing on one dimensional photonic crystals, from the design and optimization of the 1DPC till the measurements of real human plasma samples and the development of a more compact readout scheme for the fluorescence enhancement.

As seen in Chapter 1, modelling an angular resonance as a simple quadratic function provides a numerical estimation of the noise of resonance position determination. In the limit of wide resonance widths the results compare to previous findings. Noise of minimum position determination has been converted into a limit of detection as an assessment criterion of the sensor device which takes into account the angular range that has to be detected by the optical system. Compared to the well established figure of merit, which relates sensitivity, resonance depth and resonance width for narrow angular range detecting systems, the additional involvement of the angular range introduces considerations of free measurement range and tolerances. The limiting case of very narrow resonances has been modelled analytically by discretization errors that can be related to mechanical stability issues of the system. Furthermore, a variety of stacks with regard to the number of periods and the layer thicknesses exhibit high sensitivity values that yield a linear relation between high and low index layer thicknesses, respectively. Then, the number of periods and layer thickness needs to be fixed for adjusting resonance depth D and angular range A in order to obtain a minimum limit of detection LoD.

In Chapter 2 fabrication of 1DPC was investigated. a-SiNx:H and a-SiOxCy:H thin films have been deposited by means of PECVD. The refractive index dispersion of selected binary and ternary alloys has been extracted in order to design periodic multilayers that have been optimized for the coupling of BSW. Although the designed silicon-based multilayers could be exploited for sensing experiments, only the 1DPC coated with the PIAD method were used in the subsequent measurement mainly due to the high number of substrates that can be coated in a single deposition run. Morover, the analysis of the angular resolved reflectance of PIAD multilayers which feature BSW resonances allowed the determination of low intrinsic losses down to $10^{-6} \sim 10^{-5}$. The losses measured for the BSW-stacks are seemingly reliable. The findings about n and k values of the deposited PIAD materials were used to design the final BSW multilayer that have been used to perform the bioassays. The optical system exploited for the measurements was also disclosed. The BSW platform takes advantage of a tandem configuration label-free/fluorescence and is furnished with a plastic disposable and low cost sensor unit.

Chapter 3 reports the surface functionalization technique that have been used for the measurements. The 1DPC surface was made bio-compatible through APTES chemistry and GAH crosslinker. Specific antibodies for the targeted biomarkers were bio-conjugated to the sensitive area of the sensor by means of a microfluidic spotting tool.

Finally in Chapter 4 the biosensing experiments are shown. Using a novel biosensing BSW platform it was demonstrated the detection of the VEGF cancer biomarker in matrices of increasing complexity, such as cell culture supernatants and human plasma samples. The label-free technique has a great LoD_{LF}^{VEGF} of 16.5 ng/mL, can provide useful information about the kinetics of the binding reactions and the lowest concentration detected was 25 ng/mL. The fluorescence detection mode could detect VEGF molecules down to 2.5 ng/mL in human plasma samples with a calculated LoD_{F}^{VEGF} of 0.98 ng/mL, close to the plasma VEGF concentration values previously reported for cancer patients (i.e., in the order of one hundred or a few hundreds of pg/ml).

The proposed biosensing system demonstrated also its usefulness for the detection of relevant clinical levels of the angiogenic factor Ang2 in patient plasma samples. The platform LoD has been found compatible with clinically relevant concentrations inside patients plasma samples. The system was capable to determinate Ang2 concentration in plasma samples using low volumes, 300μl, with short turnaround times ,30 minutes, and without any sample pre-treatment or dilution. This was the first BSW based biosensor assay for the determination of Ang2 in plasma samples at relevant concentrations. The robustness was assessed with the good reproducibility proven by low coefficients of variation. The fluorescence outcome was comparable between more than 15 measurements in different days. The Ang2 plasma concentrations determined with the BSW system were validated by ELISA measurements and a good agreement between both results were found.

An optofluidic chip made of a nanopatterned 1DPC integrated on a elastomeric microfluidics has been proposed for fluorescence-based sensing in Chapter 5. Thanks to the radiation beaming provided by the photonic structure, a high-efficiency fluorescence collection can be obtained even with low NA optics. An overall improvement in detecting antigene molecules has been demonstrated with a simple home-made fluorescence imaging setup. The approach can be advantageously exploited in compact, low-cost optical systems for the fluorescence read-out of miniaturized optofluidic chips in point-of-care devices. For a reproducible and robust spotting of labelled analytes, a flow-through PDMS membrane aligned to the grating areas can be employed.

The outcomes of this thesis affirm that the BSW biosensing platforms can be a valuable tool for fast diagnostics of different type of biomarkers and paves the way for the development of multiplexing BSW biosensor for the detection and monitoring of multiple clinical analytes.

Publications and conferences

List of publications

1. Rizzo, R. et al., Detection of the VEGF tumor biomarker in different biological matrices with a Bloch surface wave label-free and fluorescence platform. **To be submitted** to Sens. Actuators, B.

2. Rizzo, R. et al., Surface enhanced fluorescence biosensor for the detection of clinically relevant levels of Angiopoietin-2 tumor biomarker directly from plasma of cancer patients. **To be submitted** to Sci. Rep.

3. Ricciardi, S., Rizzo, R. et al. , 2015. Optofluidic chip for surface wave-based fluorescence sensing. Sensors Actuators, B Chem. 215, 225–230. doi:10.1016/j.snb.2015.03.063.

4. Sinibaldi, A., Rizzo, R. et al. , 2015. Phase-sentitive bloch surface wave biosensors, in: 2015 XVIII AISEM Annual Conference. IEEE, pp. 1–4. doi:10.1109/AISEM.2015.7066790.

5. Sinibaldi, A., Rizzo, R. et al. , 2015. Angularly resolved ellipsometric optical biosensing by means of Bloch surface waves. Anal. Bioanal. Chem. 3965–3974. doi:10.1007/s00216-015-8591-8.

6. Sinibaldi, A., Rizzo, R. et al. , 2015. Label-Free Detection of Tumor Angiogenesis Biomarker Angiopoietin 2 Using Bloch Surface Waves on One Dimensional Photonic Crystals. J. Light. Technol. 33, 3385–3393. doi:10.1109/JLT.2015.2448795.

7. Anopchenko, A., Rizzo, R. et al. , 2016. Effect of thickness disorder on the performance of photonic crystal surface wave sensors. Opt. Express 24, 7728. doi:10.1364/OE.24.007728.

8. Pirani, F., Rizzo, R. et al. , 2016. Light-Driven Reversible Shaping of Individual Azopolymeric Micro-Pillars. Sci. Rep. 6, 31702. doi:10.1038/srep31702.
9. Mandracci, P., Rizzo, R. et al. , 2016. Optical and structural properties of amorphous silicon-nitrides and silicon-oxycarbides: Application of multilayer structures for the coupling of Bloch Surface Waves. J. Non. Cryst. Solids 453, 113–117. doi:10.1016/j.jnoncrysol.2016.10.002.

Conferences

1. Rizzo, R., et al., Detection of Angiopoietin 2 biomarker in human plasma using a biosensing platform based on Bloch surface wave enhanced fluorescence, 2016, 18th edition of the Italian National Congress on Photonics Technology.
2. Rizzo, R., et al., Measurement of Angiopoietin 2 tumor biomarker in plasma from colorectal cancer patients by means of a platform based on Bloch surface wave, 2016, European Optical Society Annual Meeting (EOSAM).

References

Angelini, A., Barakat, E., Munzert, P., Boarino, L., De Leo, N., Enrico, E., Giorgis, F., Herzig, H. P., Pirri, C. F., and Descrovi, E. (2014a). Focusing and Extraction of Light mediated by Bloch Surface Waves. *Scientific Reports*, 4:5428.

Angelini, A., Enrico, E., De Leo, N., Munzert, P., Boarino, L., Michelotti, F., Giorgis, F., and Descrovi, E. (2013). Fluorescence diffraction assisted by Bloch surface waves on a one-dimensional photonic crystal. *New Journal of Physics*, 15(7):073002.

Angelini, A., Munzert, P., Enrico, E., De Leo, N., Scaltrito, L., Boarino, L., Giorgis, F., and Descrovi, E. (2014b). Surface-Wave-Assisted Beaming of Light Radiation from Localized Sources. *ACS Photonics*, 1(7):612–617.

Anopchenko, A., Occhicone, A., Rizzo, R., Sinibaldi, A., Figliozzi, G., Danz, N., Munzert, P., and Michelotti, F. (2016). Effect of thickness disorder on the performance of photonic crystal surface wave sensors. *Optics Express*, 24(7):7728.

Badugu, R., Nowaczyk, K., Descrovi, E., and Lakowicz, J. R. (2013). Radiative decay engineering 6: Fluorescence on one-dimensional photonic crystals. *Analytical Biochemistry*, 442(1):83–96.

Butler, L. and Laqua, K. (1996). Nomenclature, symbols, units and their usage in spectrochemical analysis—IX. Instrumentation for the spectral dispersion and isolation of optical radiation. *Spectrochimica Acta Part B: Atomic Spectroscopy*, 51(7):645–664.

Caine, G. J., Blann, A. D., Stonelake, P. S., Ryan, P., and Lip, G. Y. H. (2003). Plasma angiopoietin-1, angiopoietin-2 and Tie-2 in breast and prostate cancer: a comparison with VEGF and Flt-1. *European Journal of Clinical Investigation*, 33(10):883–890.

Chinowsky, T. M., Soelberg, S. D., Baker, P., Swanson, N. R., Kauffman, P., Mactutis, A., Grow, M. S., Atmar, R., Yee, S. S., and Furlong, C. E. (2007). Portable 24-analyte surface plasmon resonance instruments for rapid, versatile biodetection. *Biosensors and Bioelectronics*, 22(9-10):2268–2275.

Choi, C. J. and Cunningham, B. T. (2006). Single-step fabrication and characterization of photonic crystal biosensors with polymer microfluidic channels. *Lab on a chip*, 6(10):1373–80.

Comşa, e., Cîmpean, A. M., and Raica, M. (2015). The Story of MCF-7 Breast Cancer Cell Line: 40 years of Experience in Research. *Anticancer research*, 35(6):3147–54.

Cooper, M. a. (2002). Optical biosensors in drug discovery. *Nature Reviews Drug Discovery*, 1(7):515–528.

Danz, N., Kick, A., Sonntag, F., Schmieder, S., Höfer, B., Klotzbach, U., and Mertig, M. (2011). Surface plasmon resonance platform technology for multi-parameter analyses on polymer chips. *Engineering in Life Sciences*, 11(6):566–572.

Descrovi, E., Barakat, E., Angelini, A., Munzert, P., De Leo, N., Boarino, L., Giorgis, F., and Herzig, H. P. (2013). Leakage radiation interference microscopy. *Optics letters*, 38(17):3374–6.

Descrovi, E., Sfez, T., Quaglio, M., Brunazzo, D., Dominici, L., Michelotti, F., Herzig, H. P., Martin, O. J. F., and Giorgis, F. (2010). Guided bloch surface waves on ultrathin polymeric ridges. *Nano Letters*, 10(6):2087–2091.

Dey, B., Thukral, S., Krishnan, S., Chakrobarty, M., Gupta, S., Manghani, C., and Rani, V. (2012). DNA–protein interactions: methods for detection and analysis. *Molecular and Cellular Biochemistry*, 365(1-2):279–299.

Ehresman, D. J., Froehlich, J. W., Olsen, G. W., Chang, S.-C., and Butenhoff, J. L. (2007). Comparison of human whole blood, plasma, and serum matrices for the determination of perfluorooctanesulfonate (PFOS), perfluorooctanoate (PFOA), and other fluorochemicals. *Environmental Research*, 103(2):176–184.

Eklund, L. and Saharinen, P. (2013). Angiopoietin signaling in the vasculature. *Experimental Cell Research*, 319(9):1271–1280.

Engin, H., Üstünda˘, Y., Ishak, ., Tekin, Ö., Gökmen, A., Ertop, E., Uygun, S., Ilikhan, ., Üstündağ, Y., Tekin, s. Ö., Gökmen, A., Ertop, e., and İlikhan, S. U. (2012a). Plasma concentrations of angiopoietin-1, angiopoietin-2 and Tie-2 in colon cancer. *European Cytokine Network*, 23(232):68–71.

Engin, H., Üstünda˘ G, Y., Ishak, ., Tekin, Ö., and Gökmen, A. (2012b). Plasma concentrations of Ang-1, Ang-2 and Tie-2 in gastric cancer. *Eur. Cytokine Netw. Eur. Cytokine Netw*, 23(231):21–4.

Fan, X., White, I. M., Shopova, S. I., Zhu, H., Suter, J. D., and Sun, Y. (2008). Sensitive optical biosensors for unlabeled targets: A review. *Analytica Chimica Acta*, 620(1-2):8–26.

Ferlay, J., Soerjomataram, I., Dikshit, R., Eser, S., Mathers, C., Rebelo, M., Parkin, D. M., Forman, D., and Bray, F. (2015). Cancer incidence and mortality worldwide: Sources, methods and major patterns in GLOBOCAN 2012. *International Journal of Cancer*, 136(5):E359–E386.

Ferrara, N. (2010). Vascular endothelial growth factor and age-related macular degeneration: from basic science to therapy. *Nature Medicine*, 16(10):1107–1111.

Fiorilli, S., Rivolo, P., Descrovi, E., Ricciardi, C., Pasquardini, L., Lunelli, L., Vanzetti, L., Pederzolli, C., Onida, B., and Garrone, E. (2008). Vapor-phase self-assembled monolayers of aminosilane on plasma-activated silicon substrates. *Journal of Colloid and Interface Science*, 321(1):235–241.

Fort, E. and Grésillon, S. (2008). Surface enhanced fluorescence. *Journal of Physics D: Applied Physics*, 41(1):013001.

Giorgis, F., Pirri, C., and Tresso, E. (1997). Structural properties of a-Si1-xNx:H films grown by plasma enhanced chemical vapour deposition by SiH4+NH3+H2 gas mixtures. *Thin Solid Films*, 307(1-2):298–305.

Giorgis, F., Pirri, C. F., Vinegoni, C., and Pavesi, L. (1999). Luminescence processes in amorphous hydrogenated silicon-nitride nanometric multilayers. *Physical Review B*, 60(16):11572–11576.

Guo, X. (2012). Surface plasmon resonance based biosensor technique: A review. *Journal of Biophotonics*, 5(7):483–501.

Huber, W., Barner, R., Fattinger, C., Hübscher, J., Koller, H., Müller, F., Schalatter, D., and Lukosz, W. (1992). Direct optical immunosensing (sensitivity and selectivity). *Sensors and Actuators B: Chemical*, 6(1-3):122–126.

Iinuma (2010). Association of plasma VEGF-A, soluble VEGFR-1 and VEGFR-2 levels and clinical response and survival in advanced colorectal cancer patients receiving bevacizumab with modified FOLFOX6. *Oncology Letters*, 1(2):253–259.

Jang, L.-S. and Liu, H.-J. (2009). Fabrication of protein chips based on 3-aminopropyltriethoxysilane as a monolayer. *Biomedical Microdevices*, 11(2):331–338.

Jelkmann, W. (2001). Pitfalls in the measurement of circulating vascular endothelial growth factor. *Clinical chemistry*, 47(4):617–23.

Jiang, J., Huang, H., Wang, Q., Zhu, W., Hao, J., and Liu, W. (2014). Comparative study on structure and properties of titanium/silicon mono- and co-doped amorphous carbon films deposited by mid-frequency magnetron sputtering. *Surface and Interface Analysis*, 46(3):139–144.

Karlsson, R., Michaelsson, A., and Mattsson, L. (1991). Kinetic analysis of monoclonal antibody-antigen interactions with a new biosensor based analytical system. *Journal of Immunological Methods*, 145(1-2):229–240.

Kim, H. J., Shao, Q., and Kim, Y.-H. (2003). Characterization of low-dielectric-constant SiOC thin films deposited by PECVD for interlayer dielectrics of multilevel interconnection. *Surface and Coatings Technology*, 171(1-3):39–45.

Konopsky, V., Karakouz, T., Alieva, E., Vicario, C., Sekatskii, S., and Dietler, G. (2013). Photonic Crystal Biosensor Based on Optical Surface Waves. *Sensors*, 13(3):2566–2578.

Lakowicz, J. R. (2006). *Principles of fluorescence spectroscopy.*

Ławicki, S., Zajkowska, M., Głażewska, E. K., Będkowska, G. E., and Szmitkowski, M. (2016). Plasma levels and diagnostic utility of VEGF, MMP-9, and TIMP-1 in the diagnosis of patients with breast cancer. *OncoTargets and therapy*, 9:911–9.

Levi, P. (1987). *Storie naturali.* Einaudi.

Ligler, F. S. and Taitt, C. A. R. (2008). *Optical biosensors : today and tomorrow.* Elsevier.

Lin, Z., Guo, Y., Song, C., Song, J., Wang, X., Zhang, Y., Huang, R., and Huang, X. (2015). Influence of the oxygen content in obtaining tunable and strong photoluminescence from low-temperature grown silicon oxycarbide films. *Journal of Alloys and Compounds*, 633:153–156.

Liscidini, M. and Sipe, J. E. (2009). Analysis of Bloch-surface-wave assisted diffraction-based biosensors. *Journal of the Optical Society of America B*, 26(2):279.

Liu, J.-T., Chen, L.-Y., Shih, M.-C., Chang, Y., and Chen, W.-Y. (2008). The investigation of recognition interaction between phenylboronate monolayer and glycated hemoglobin using surface plasmon resonance. *Analytical Biochemistry*, 375(1):90–96.

Loughna, S. and Sato, T. N. (2001). Angiopoietin and Tie signaling pathways in vascular development. *Matrix Biology*, 20(5-6):319–325.

Luo, G.-L., Lee, C.-C., Cheng, C.-L., Tsai, M.-H., and Fang, W. (2013). CMOS-MEMS Fabry-Perot optical interference device with tunable resonant cavity. In *2013 Transducers & Eurosensors XXVII: The 17th International Conference on Solid-State Sensors, Actuators and Microsystems (TRANSDUCERS & EUROSENSORS XXVII)*, pages 2600–2603. IEEE.

Maisonpierre, P. C., Suri, C., Jones, P. F., Bartunkova, S., Wiegand, S. J., Radziejewski, C., Compton, D., McClain, J., Aldrich, T. H., Papadopoulos, N., Daly, T. J., Davis, S., Sato, T. N., and Yancopoulos, G. D. (1997). Angiopoietin-2, a Natural Antagonist for Tie2 That Disrupts in vivo Angiogenesis. *Science*, 277(5322):55–60.

Mandracci, P., Mussano, F., Ricciardi, C., Ceruti, P., Pirri, F., and Carossa, S. (2008). Low temperature growth of thin film coatings for the surface modification of dental prostheses. *Surface and Coatings Technology*, 202(11):2477–2481.

Mandracci, P. and Ricciardi, C. (2007). Silicon–carbon–oxynitrides grown by plasma-enhanced chemical vapor deposition technique. *Thin Solid Films*, 515(19):7639–7642.

Mathias, P. C., Ganesh, N., Chan, L. L., and Cunningham, B. T. (2007). Combined enhanced fluorescence and label-free biomolecular detection with a photonic crystal surface. *Applied Optics*, 46(12):2351.

Mehlen, P. and Puisieux, A. (2006). Metastasis: a question of life or death. *Nature Reviews Cancer*, 6(6):449–458.

Mittal, K. L. and International Symposium on Silanes and Other Coupling Agents. (1992). *Silanes and other coupling agents*. VSP.

Miyazaki, H. (2008). Structure and Optical Properties of Silicon Oxycarbide Films Deposited by Reactive RF Magnetron Sputtering Using a SiC Target. *Japanese Journal of Applied Physics*, 47(11):8287–8290.

Munzert, P., Schulz, U., and Kaiser, N. (2003). Transparent thermoplastic polymers in plasma-assisted coating processes. *Surface and Coatings Technology*, 174-175:1048–1052.

Naimushin, A. N., Soelberg, S. D., Nguyen, D. K., Dunlap, L., Bartholomew, D., Elkind, J., Melendez, J., and Furlong, C. E. (2002). Detection of Staphylococcus aureus enterotoxin B at femtomolar levels with a miniature integrated two-channel surface plasmon resonance (SPR) sensor. *Biosensors & bioelectronics*, 17(6-7):573–84.

Novotny, L. and Hecht, B. (2012). *Principles of Nano-Optics*. Cambridge University Press, 2nd editio edition.

Paeder, V., Musi, V., Hvozdara, L., Herminjard, S., and Herzig, H. (2011). Detection of protein aggregation with a Bloch surface wave based sensor. *Sensors and Actuators B: Chemical*, 157(1):260–264.

Palik, E. D. (1998). *Handbook of optical constants of solids*. Academic Press.

Park, J. H. (2007). Serum Angiopoietin-2 as a Clinical Marker for Lung Cancer. *CHEST Journal*, 132(1):200.

Pepe, M. S., Etzioni, R., Feng, Z., Potter, J. D., Thompson, M. L., Thornquist, M., Winget, M., and Yasui, Y. (2001). Phases of biomarker development for early detection of cancer. *Journal of the National Cancer Institute*, 93(14):1054–61.

Piliarik, M. and Homola, J. (2009). Surface plasmon resonance (SPR) sensors: approaching their limits? *Optics express*, 17(19):16505–17.

Piliarik, M., Vaisocherova, H., and Homola, J. (2007). Towards parallelized surface plasmon resonance sensor platform for sensitive detection of oligonucleotides. *Sensors and Actuators B: Chemical*, 121(1):187–193.

Piliarik, M., Vala, M., Tichý, I., and Homola, J. (2009). Compact and low-cost biosensor based on novel approach to spectroscopy of surface plasmons. *Biosensors and Bioelectronics*, 24(12):3430–3435.

Pokhriyal, A., Lu, M., Chaudhery, V., Huang, C.-S., Schulz, S., and Cunningham, B. T. (2010). Photonic crystal enhanced fluorescence using a quartz substrate to reduce limits of detection. *Optics Express*, 18(24):24793.

Pomorski, T. A., Bittel, B. C., Lenahan, P. M., Mays, E., Ege, C., Bielefeld, J., Michalak, D., and King, S. W. (2014). Defect structure and electronic properties of SiOC:H films used for back end of line dielectrics. *Journal of Applied Physics*, 115(23):234508.

Professor Dr. Heinz Raether (1988). *Surface Plasmons on Smooth and Rough Surfaces and on Gratings*, volume 111 of *Springer Tracts in Modern Physics*. Springer Berlin Heidelberg.

Ray, K., Badugu, R., and Lakowicz, J. R. (2015). Bloch surface wave-coupled emission from quantum dots by ensemble and single molecule spectroscopy. *RSC Adv.*, 5(67):54403–54411.

Rayleigh, L. (1888). XXVI. On the remarkable phenomenon of crystalline reflexion described by Prof. Stokes. *Philosophical Magazine Series 5*, 26(160):256–265.

Remy-Martin, F., El Osta, M., Lucchi, G., Zeggari, R., Leblois, T., Bellon, S., Ducoroy, P., and Boireau, W. (2012). Surface plasmon resonance imaging in arrays coupled with mass spectrometry (SUPRA-MS): proof of concept of on-chip characterization of a potential breast cancer marker in human plasma. *Analytical and bioanalytical chemistry*, 404(2):423–32.

Ricciardi, S., Frascella, F., Angelini, A., Lamberti, A., Munzert, P., Boarino, L., Rizzo, R., Tommasi, A., and Descrovi, E. (2015). Optofluidic chip for surface wave-based fluorescence sensing. *Sensors and Actuators, B: Chemical*, 215:225–230.

Rivolo, P., Michelotti, F., Frascella, F., Digregorio, G., Mandracci, P., Dominici, L., Giorgis, F., and Descrovi, E. (2012). Real time secondary antibody detection by means of silicon-based multilayers sustaining Bloch surface waves. *Sensors and Actuators B: Chemical*, 161(1):1046–1052.

Rizzo, R., Danz, N., Michelotti, F., Maillart, E., Anopchenko, A., and Wächter, C. (2014a). Optimization of angularly resolved Bloch surface wave biosensors. *Optics Express*, 22(19):23202.

Rizzo, R., Danz, N., Michelotti, F., Munzert, P., and Sinibaldi, A. (2014b). Limit of detection comparison for surface wave biosensors. In Berghmans, F., Mignani, A. G., and De Moor, P., editors, *Proc. SPIE 9141, Optical Sensing and Detection III*, volume 9141, page 91410P.

Robertson, J. (1991). Electronic structure of silicon nitride. *Philosophical Magazine Part B*, 63(1):47–77.

Shi, J., Xu, F., Zhou, P., Yang, J., Yang, Z., Chen, D., Yin, Y., Chen, D., and Ma, Z. (2013). Refined nano-textured surface coupled with SiNx layer on the improved photovoltaic properties of multi-crystalline silicon solar cells. *Solid-State Electronics*, 85:23–27.

Shinn, M. and Robertson, W. (2005). Surface plasmon-like sensor based on surface electromagnetic waves in a photonic band-gap material. *Sensors and Actuators B: Chemical*, 105(2):360–364.

Sikarwar, B., Singh, V. V., Sharma, P. K., Kumar, A., Thavaselvam, D., Boopathi, M., Singh, B., and Jaiswal, Y. K. (2017). DNA-probe-target interaction based detection of Brucella melitensis by using surface plasmon resonance. *Biosensors and Bioelectronics*, 87:964–969.

Sinibaldi, A., Anopchenko, A., Rizzo, R., Danz, N., Munzert, P., Rivolo, P., Frascella, F., Ricciardi, S., and Michelotti, F. (2015). Angularly resolved ellipsometric optical biosensing by means of Bloch surface waves. *Analytical and Bioanalytical Chemistry*, pages 3965–3974.

Sinibaldi, A., Danz, N., Descrovi, E., Munzert, P., Schulz, U., Sonntag, F., Dominici, L., and Michelotti, F. (2012). Direct comparison of the performance of Bloch surface wave and surface plasmon polariton sensors. *Sensors and Actuators B: Chemical*, 174:292–298.

Sinibaldi, A., Fieramosca, A., Rizzo, R., Anopchenko, A., Danz, N., Munzert, P., Magistris, C., Barolo, C., and Michelotti, F. (2014). Combining label-free and fluorescence operation of Bloch surface wave optical sensors. *Opt. Lett.*, 39(10):2947–2950.

Sinibaldi, A., Rizzo, R., Figliozzi, G., Descrovi, E., Danz, N., Munzert, P., Anopchenko, A., and Michelotti, F. (2013). A full ellipsometric approach to optical sensing with Bloch surface waves on photonic crystals. *Optics Express*, 21(20):23331–23344.

Stewart, B. and Wild, C. (2014). World Cancer Report 2014.

Taitt, C. R., Anderson, G. P., and Ligler, F. S. (2016). Evanescent wave fluorescence biosensors: Advances of the last decade. *Biosensors and Bioelectronics*, 76:103–112.

Tan, W., Sabet, L., Li, Y., Yu, T., Klokkevold, P. R., Wong, D. T., and Ho, C.-M. (2008). Optical protein sensor for detecting cancer markers in saliva. *Biosensors and Bioelectronics*, 24(2):266–271.

Teixeira, A. C., Brasil, I. R., Torres, A. F., and Tavora, F. (2016). The Evaluation of Angiogenesis Markers in Hepatocellular Carcinoma and Precursor Lesions in Liver Explants From a Single Institution. *Applied Immunohistochemistry & Molecular Morphology*, page 1.

Tighe, P. J., Ryder, R. R., Todd, I., and Fairclough, L. C. (2015). ELISA in the multiplex era: Potentials and pitfalls.

Treviño, J., Calle, A., Rodríguez-Frade, J., Mellado, M., and Lechuga, L. (2009). Determination of human growth hormone in human serum samples by surface plasmon resonance immunoassay. *Talanta*, 78(3):1011–1016.

Ulber, R., Frerichs, J.-G., and Beutel, S. (2003). Optical sensor systems for bioprocess monitoring. *Analytical and bioanalytical chemistry*, 376(3):342–8.

Wan, Y., McIntosh, K. R., and Thomson, A. F. (2013). Characterisation and optimisation of PECVD SiNx as an antireflection coating and passivation layer for silicon solar cells. *AIP Advances*, 3(3):032113.

Wu, C., Li, Y., Baklanov, M. R., and Croes, K. (2014). Electrical Reliability Challenges of Advanced Low-k Dielectrics. *ECS Journal of Solid State Science and Technology*, 4(1):N3065–N3070.

Yablonovitch, E. (1987). Inhibited Spontaneous Emission in Solid-State Physics and Electronics. *Physical Review Letters*, 58(20):2059–2062.

Zhao, H., Mleynek, T. M., and Li, D. Y. (2016). Dysregulated exocytosis of angiopoietin-2 drives cerebral cavernous malformation. *Nature Medicine*, 22(9):971–973.

Zhao, Y., Zhao, X., and Gu, Z. (2010). Photonic Crystals in Bioassays. *Advanced Functional Materials*, 20(18):2970–2988.

Ziegel, E., Press, W., Flannery, B., Teukolsky, S., and Vetterling, W. (1987). Numerical Recipes: The Art of Scientific Computing. *Technometrics*, 29(4):501.